VERBAND DER DEUTSCHEN FEDERNINDUSTRIE

1st Compendium of Modern Spring Technologies 2021

Miniaturized Fatigue Testing Devices to characterize Fatigue Damage Evolution

FE Simulation of Power Springs



A new test bench for rotating bending fatigue test of tempered steel wires

Maintaining the functionality of springs via a high-performance zinc flake system

Development of fatigue strength diagrams for helical compression springs

A Novel Algorithm for the Determination of Stress States in Loaded Disc Springs

Examinations on composite strips for springs under torsional load

Design and Analysis of Composite Structures for Automotive Applications

Stress Intensity Factors at Surface Cracks in Compression and Tension Springs

The Application of a Stainless Martensitic Precipitation Hardening Steel to an Elastic Spring

September 2021

Published by:
VERBAND DER DEUTSCHEN FEDERNINDUSTRIE e.V.
Goldene Pforte 1
58093 Hagen
tel.: +049 2331 9588 57
fax: +049 2331 9587 57
web: www.federnverband.de

Editors:
Andres Weinrich
Wolfgang Hermann

cover design by:
Dr. Andres Weinrich

© All rights reserved
August 2021

Table of Contents

Table of Contents i

Preface ii

A Novel Algorithm for the Determination of Stress States in Loaded Disc Springs 3
Max. B. GEILEN, Marcus KLEIN and Matthias OECHSNER

Development of fatigue strength diagrams for helical compression springs made of spring steel wire 9
Martin PETRICH, René REICH and Ulf KLETZIN

FE Simulation of Power Springs 19
Thomas Rausch and Georg.Hannig

Stress Intensity Factors at Surface Cracks in Compression and Tension Springs 25
Yuji NAKASONE

A new test bench for rotating bending fatigue test of tempered steel wires 33
Federico BALLO, Michele CARBONI, Gianpiero MASTINU and Giorgio PREVIATI

Miniaturised Fatigue Testing Devices to characterise Fatigue Damage Evolution 37
Anna WILDEIS, Matthias THIMM, Robert BRANDT, Hans-Jürgen CHRIST and Claus-Peter FRITZEN

Design and Analysis of Composite Structures for Automotive Applications. Chassis and Drivetrain 45
Vladimir KOBELEV and Jörg NEUBRAND

Examinations on composite strips for springs under torsional load 53
Martin PETRICH, Stefan TITZE, Tom-Luis WEIMANN and Ulf KLETZIN

The Application of a Stainless Martensitic Precipitation Hardening Steel to an Elastic Spring 61
Robert BRANDT, Martin LINDNER and Andreas ELVENKEMPER

Maintaining the functionality of springs via a high-performance zinc flake system. 68
Klaus GRADTKE

©VDFI

Preface

Technical springs are usually invisible parts of our everyday life. They make our life easier and safer. Technical springs can be used in simple toys or in very sophisticated medical technology but also irreplaceable in both traditional and modern measurement technology. You will also find springs in all kind of vehicles and even in building technology. Springs are and remain a very effective energy storage element with a high degree of efficiency. The environmental conditions where springs are used can be very different from very low to very high temperatures, from vacuum to acidic atmosphere.

The essential foundations of technical springs are extensively researched and understood. However, the demands on the spring increase continuously.

The improvements in research knowledge are meaningless if they cannot be implemented under industrial conditions. Therefore, a close cooperation between research and industry is a matter of special importance.

This diversity and the increasing demands on quality, dimensional accuracy and higher durability requires an improvement of this “simple” machine part, whose main property is to store mechanical energy, must be allowed for the demands of the future. This is the essence of the first ICST in Japan in 2015. In 2018, the International Committee of the ICST decided to hold the second ICST in Germany in 2020.

Due to the COVID-19 pandemic we had first to postpone the 2nd ICST to 2020 and later we have to cancel the online conference on 2021. Before the conference has been canceled several full papers had been submitted. This great support and interest of the authors on the ICST has prompted us to publish the contributions. In order to rewarded the work and effort of the authors.Therefore, the VDFI decided to compile the submitted papers into this document.

Responsible for the peer-review of the presented paperds was the The local committee of Germany is responsible for the peer-review process of the abstracts and papers

Committee:

- Dr. Andres Weinrich, VDFI e.V. (local committee and conference chair)
- Prof. Dr. Robert Brandt, University of Siegen
- Dr. Michael Hellmann, C.D. Wälzholz GmbH & Co. KG
- Dr. Marcus Klein, State Materials Testing Institute Darmstadt/ Chair and Institute for Materials Technology,
- Prof. Dr. Ulf Kletzin, Technische Universität Ilmenau
- Prof. Dr. Vladimir Kobelev, University of Siegen / Muhr und Bender KG
- Dr. Rüdiger Lux, Westfälische Drahtindustrie GmbH
- Prof. Dr. Eckehard Müller, University of Applied Sciences Bochum
- Dr. Peter Thoma, SCHERDEL GmbH

We hope the pandemic situation calm down in a timely manner and the next ICST is able to take place, with German support but in an other Country of the international committee.

Wolfgang Hermann & Dr. Andres Weinrich
Hagen, Germany August 2021

A Novel Algorithm for the Determination of Stress States in Loaded Disc Springs

Max. B. GEILEN, Marcus KLEIN, Matthias OECHSNER
Centre for Engineering Materials (MPA-IfW) TU Darmstadt
TEL: +49 6151 16-25867, E-Mail: geilen@mpa-ifw.tu-darmstadt.de

In this paper, a novel algorithm for the determination of stress states in loaded disc springs is presented. The algorithm takes a 3D-scan of a disc spring, measured residual stresses, material parameters and spring loads as inputs. It outputs a distribution of Walker parameters over the surface area of the input disc spring. As the algorithm allows a fully automated determination of the stress state, it can be used by disc spring manufacturers to significantly reduce the working time spent on this task by specialised engineers. Compared to spreadsheet applications using analytical formulas and finite elements models using idealized geometry, this approach offers a superior description of the stress states in disc springs.

Keywords: disc springs, fatigue, FEA, automation, real geometry, Abaqus Scripting

1. INTRODUCTION

1.1 MOTIVATION

The fatigue behaviour of disc springs can be described by models ranging widely in complexity. Simple models like the one described in [1),2)] can be implemented using spreadsheet applications, e.g. Microsoft Excel. As models become more sophisticated, the expense of building and evaluating the model rises. With the latest step in creating more complex models, the introduction of scanned geometries, superposed residual stresses and the Walker damage parameter, a need for a novel algorithm for the determination of stress states in loaded disc springs has arisen.

1.2 SCOPE

An introduction to the Walker damage parameter is given in chapter 2. In chapter 3, an algorithm used to describe Walker damage at the surface of a 3D-scanned disc spring is presented. Its implementation is described in chapter 4. The algorithm described in this paper is an application of the Spring_stack Python module, which also has a wider range of applications. For more information on the simulation without 3D-scanned geometry or with multiple springs in one assembly, see [3),4)].

2 THE WALKER PARAMETER

The Walker damage parameter [5)] helps to compare the fatigue behavior of materials under different mean stresses. Compared with other approaches to the characterization of mean stress effects in steels [6),7),8)], the Walker parameter shows a superior lifetime prediction [9)]. In this paper, the stress-based approach is described. For the strain-based approach, see [10)].

The Walker damage parameter P_{Walker} is computed from the maximum stress σ_{max}, the stress amplitude σ_{amp} and the Walker exponent γ:

$$P_{Walker} = \sigma_{max}^{1-\gamma}\sigma_{amp}^{\gamma} \quad (1)$$

The Walker exponent is a material parameter which can be identified by fitting SN-curves with different mean stresses or R-ratios. A high Walker exponent implies a low sensitivity to mean stress effects, while a low Walker parameter implies a high sensitivity. If the Walker exponent is fixed to 0.5, the stress Walker approach is equivalent to the stress Smith Watson Topper[8)] approach.

The Walker equation requires σ_{max} and σ_{amp} to be scalar values. At the surface of the disc spring, the stress state is two-dimensional, therefore an equivalent stress must be computed. Here, the von Mises equivalent stress is used.

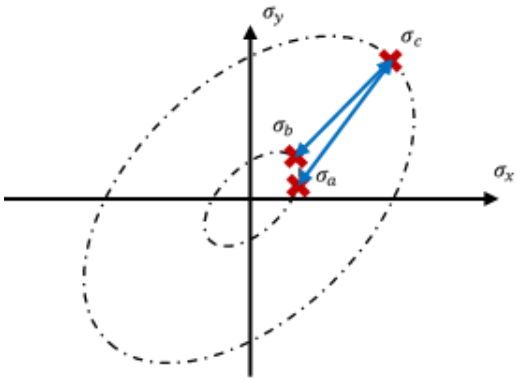

Fig. 1: Planar stress with von Mises equivalent (zero shear)

©VDFI

For proportional loads in quadrant 1, the computation of the maximum stress σ_{max} and the stress amplitude σ_{amp} from the minimum and maximum principal stresses $\sigma_{I,max}$, $\sigma_{II,max}$, $\sigma_{I,min}$ and $\sigma_{II,min}$ is obvious.

$$\sigma_{max} = \sqrt{\frac{\sigma_{I,max}^2 + (\sigma_{I,max} - \sigma_{II,max})^2 + \sigma_{II,max}^2}{2}} \quad (2)$$

$$\sigma_{min} = \sqrt{\frac{\sigma_{I,min}^2 + (\sigma_{I,min} - \sigma_{II,min})^2 + \sigma_{II,min}^2}{2}} \quad (3)$$

$$\sigma_{amp} = 0.5 \cdot (\sigma_{max} - \sigma_{min}) \quad (4)$$

The stress state in disc springs however is non-proportional, especially in shot peened specimens. An example why the formulas given for the proportional case may give inconsistent results for the non-proportional case is depicted in Fig. 1. Given the stress states σ_a, σ_b and σ_c in quadrant 1, the stress amplitude between σ_a and σ_c is equal to the stress amplitude between σ_b and σ_c if the von Mises equivalent stress in σ_a is equal to the von Mises equivalent stress in σ_b. The same applies for mean stresses. In reality, the damage inflicted by cycling between σ_b and σ_c is smaller than the damage inflicted by cycling between σ_a and σ_c.

To avoid the described misrepresentation of damage inflicted, the Modified Manson-McKnight Method[11] is used. Instead of computing two scalar stress states σ_{max} and σ_{min} and deducing a scalar amplitude and a scalar mean stress, a two-dimensional stress amplitude and a two-dimensional mean stress are deduced from a two-dimensional maximum and minimum stress state:

$$\sigma_{I,amp} = 0{,}5 \cdot (\sigma_{I,max} - \sigma_{I,min}) \quad (5)$$

$$\sigma_{II,amp} = 0{,}5 \cdot (\sigma_{II,max} - \sigma_{II,min}) \quad (6)$$

$$\sigma_{I,mean} = 0{,}5 \cdot (\sigma_{I,max} + \sigma_{I,min}) \quad (7)$$

$$\sigma_{II,mean} = 0{,}5 \cdot (\sigma_{II,max} + \sigma_{II,min}) \quad (8)$$

These pairs of stress components are converted into von Mises equivalent stresses:

$$\sigma_{amp} = \sqrt{\frac{\sigma_{I,amp}^2 + (\sigma_{I,amp} - \sigma_{II,amp})^2 + \sigma_{II,amp}^2}{2}} \quad (9)$$

$$\sigma_{mean} = \frac{\sigma_{I,mean} - \sigma_{III,mean}}{\sigma_{I,mean} + \sigma_{III,mean}}. \quad (10)$$

$$\sqrt{\frac{\sigma_{I,mean}^2 + (\sigma_{I,mean} - \sigma_{II,mean})^2 + \sigma_{II,mean}^2}{2}}$$

The maximum stress σ_{max} is defined with a lower bound to avoid complex numbers as Walker parameters.

$$\sigma_{max} = \max(\sigma_{mean} + \sigma_{amp}, 0) \quad (11)$$

3. THE ALGORITHM

3.1 GENERAL CONCEPT

The algorithm starts with an STL-file of a disc spring placed randomly in space. After aligning the disc spring approximately symmetric around the y-axis, it imports the geometry information into a finite element application. In our implementation of the algorithm, the finite element application Abaqus is used. Through the Abaqus Scripting interface, it builds a model around the geometry data, using additional inputs like loads and friction coefficients provided by the user. It generates an output database file using the Abaqus Standard Solver. Utilizing Abaqus Viewer functionalities via the Scripting interface, a field of residual stresses is generated from input data. Aggregated minimum and maximum stress fields are computed by superpositioning the computed load stress field and the residual stress field. A Walker damage field is computed from the minimum and maximum stress fields. The Walker damage at the surface of the disc spring is computed and exported as tabular data.

3.2 ARCHITECTURE

The software architecture used is called a pipeline in programming terms and resembles a production line: An instance of the class Spring_stack is passed along a series of different processing stations. The processing stations gradually transform the instance from input data to a solved finite element model with postprocessed output fields and from there to easily readable tabular data and a graphical representation thereof. In programming terms, these processing stations are called methods. The flow of data is depicted in Fig. 2.

4. IMPLEMENTATION

4.1 ALIGNING THE DISC SPRING

In order to build a model around a part, the alignment of the part in space must be known. For example, to apply axial loads, the axial direction of the loaded part must be known. Because it makes the rest of the algorithm much easier, the input disc spring is preprocessed so it always has the same orientation. By convention, this position is in the point of origin, closely

axially symmetric to the y-axis.

In the alignment process, the mesh $\boldsymbol{\mathcal{M}_{start}}$ is processed as a set of vertices $\boldsymbol{V_{start}} = \{\boldsymbol{v_1}, \dots, \boldsymbol{v_v}\}$ and a set of triangles $\boldsymbol{e} = \{\boldsymbol{e_1}, \dots, \boldsymbol{e_e}\}$ connecting these vertices. The vertices $\boldsymbol{v_{i,start}} = (x_{i,start}, y_{i,start}, z_{i,start})$ are defined in a cartesian coordinate system (x, y, z). The point set is aligned by a translation $\boldsymbol{t}(t_x, t_y, t_z, \boldsymbol{V})$ along and a rotation $\boldsymbol{A}(\theta_x, \theta_y, \theta_z)$ around the principal axes.

$$\boldsymbol{V_{aligned}}(\boldsymbol{A}, \boldsymbol{t}, \boldsymbol{V_{start}}) = \boldsymbol{A}(\theta_x, \theta_y, \theta_z)\boldsymbol{t}(t_x, t_y, t_z, \boldsymbol{V_{start}}) \quad (12)$$

The edges are defined as connectors between vertices, therefore a geometric transformation of any mesh $\boldsymbol{\mathcal{M}}$ is fully described by a geometric transformation of its vertices $\boldsymbol{V}$. The resulting mesh $\boldsymbol{\mathcal{M}_{aligned}}$ is defined by the vertices $\boldsymbol{V_{aligned}}$ and the edges $\boldsymbol{e}$.

A feasible combination of translation $\boldsymbol{t}$ and rotation $\boldsymbol{A}$ is found by solving an optimization problem.

$$\min_{\boldsymbol{\theta_{x,y,z}}, \boldsymbol{t_{x,y,z}}} f\left(\boldsymbol{V_{aligned}}(\boldsymbol{A}, \boldsymbol{t}, \boldsymbol{V_{start}})\right) \quad (13)$$

To compute the objective function f, the transformed point cloud $\boldsymbol{V_{aligned}}$ is projected into the xy-plane, producing $\boldsymbol{V_{xy}} = \{\boldsymbol{v_{xy,1}}, \dots, \boldsymbol{v_{xy,v}}\}$ by rotation around the y-axis. $\boldsymbol{V_{xy}}$ is computed using the coordinates of $\boldsymbol{V_{aligned}}$:

$$\boldsymbol{v_{xy,i}} = \begin{pmatrix} \sqrt{\boldsymbol{x_{i,aligned}^2} + \boldsymbol{y_{i,aligned}^2}} \\ \boldsymbol{z_{i,aligned}} \end{pmatrix} \quad (14)$$

The objective function f is defined as the area A of the convex hull of $\boldsymbol{V_{xy}}$.

$$f = A\left(Conv(\boldsymbol{V_{xy}})\right)$$

The convex hull is computed using the Quickhull Algorithm [12), 13)].

The objective function f is invariant to rotations around the y-axis. Therefore, $\boldsymbol{\theta_y}$ is fixed to zero.

To further simplify the optimization problem, it is assumed that the centroid of the aligned mesh $c\left(\boldsymbol{\mathcal{M}_{aligned}}\right)$ lies in the point of origin.

Although this assumption is applicable only for perfectly symmetric spring geometries, we assume that for springs possessing minor deviations regarding their Based on this assumption, $\boldsymbol{t}$ is defined as translating the volumetric centroid c of the Mesh $\boldsymbol{\mathcal{M}_{start}}$ into the point of origin.symmetry, the assumption holds true, too.

$$c(\boldsymbol{\mathcal{M}_{translated}}) = (0,0,0) \quad (15)$$

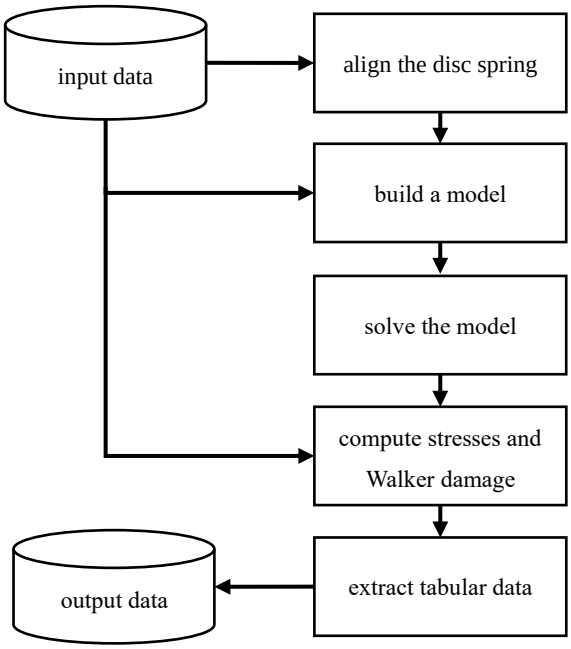

Fig. 2: Simplified flowchart of algorithm

The computational cost for finding $\boldsymbol{t}$ is low because the volumetric centroid of any closed mesh $\boldsymbol{\mathcal{M}}$ can be computed cheaply.

In the following rotation $\boldsymbol{A}$, the mesh $\boldsymbol{\mathcal{M}_{translated}}$ is only rotated around the principal axes. As the volumetric centroid lies on all three of the principal axes, it is invariant under said rotation $\boldsymbol{A}$.

$$c\left(\boldsymbol{\mathcal{M}_{aligned}}\right) = c(\boldsymbol{\mathcal{M}_{translated}}) = (0,0,0) \quad (16)$$

By fixing the translation, the dimensionality of the optimization problem is reduced from six to two.

$$\min_{\boldsymbol{\theta_{x,z}}} f\left(\boldsymbol{V_{aligned}}(\boldsymbol{A}, \boldsymbol{t}, \boldsymbol{V_{start}})\right) \quad (17)$$

The parameters θ_x and θ_z are calculated using the L-BFGS-B method [13) bis 15)].

The resulting mesh $\boldsymbol{\mathcal{M}_{aligned}}$ may be aligned upside down. This being the case, it can simply be rotated by 180 degrees around the x-axis. To further ease the following steps, it is translated along the y-axis so its lowest point is in the xz-plane.

$$min\left(y_{i,postprocessed}\right) = 0 \quad (18)$$

The postprocessed, aligned mesh $\boldsymbol{\mathcal{M}_{postprocessed}}$ is exported as an Abaqus input file (.inp).

4.2 Building the Finite Element Model

The creation of the model is structured as a pipeline inside the pipeline depicted in Fig. 2. The sub-pipeline is depicted in Fig. 3. The allotment of tasks to processing stations (methods) along the pipeline is based on the allotment of functionalities to modules in the Abaqus/CAE environment. Each of the processing stations is customized according to input data. The following paragraphs describe the individual processing stations.

For the simulation of a single disc spring, four components are required: the disc spring itself, a guide pin and two flat plates. The geometry of the disc spring is read from the input file generated from the 3D-scan data. The guide pin is defined as an idealized cylinder with the same height as the disc spring, the plates are defined as idealized planes.

The plate and the guide pin part instances are defined as analytic rigid surfaces and therefore don't need to be meshed. The part instance representing the disc spring is a surface mesh and is meshed by the free mesher implemented in Abaqus. Mesh size cannot be controlled actively but only by changing the mesh size of the imported surface mesh. The surface mesh size is adjusted by exporting very fine meshes from the 3D-scanning software GOM Scan and increasing mesh size using the quadric edge collapse decimation algorithm 16).

In the approach described in this paper, the finite element analysis uses a purely elastic material law. Residual stresses are incorporated through the superposition of measured stresses. To introduce inertia and improve convergence, a density is defined for the disc spring.

Because the spring was aligned beforehand, the assembly is straightforward. Instances of all four parts are created in the assembly module. The lower plate, the disc spring and the guide pin are already in place. The upper plate is positioned in its place by a translation along the y-axis.

The lower plate and the guide pin are fixed in space, loads are applied to the upper plate. To improve convergence, a small gravitational load is defined. No other loads are applied directly to the disc.

Forces are transmitted via contacts. Node to surface contacts are defined between the disc spring and each of the other part instances.

The Abaqus Scripting Interface includes an option to customize output requests. This option is used in the algorithm to request stress and coordinate outputs. However, coordinates cannot be requested at integration points by means of the Scripting Interface. Coordinate data in the integration points is necessary to compute residual stresses in the integration points.

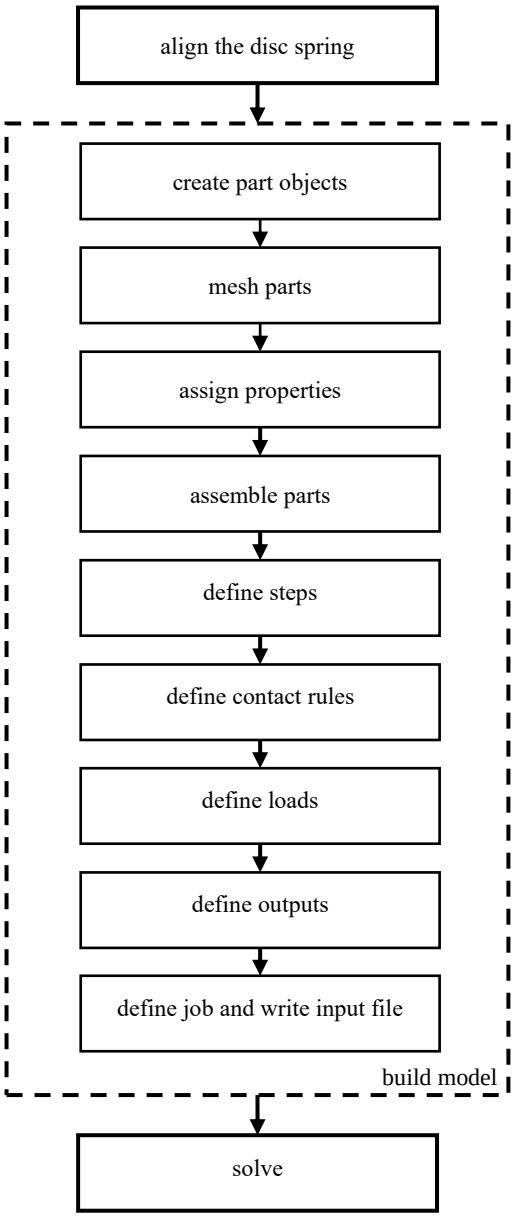

Fig. 3: Flowchart of sub-pipeline "build model"

A job instance is created to generate an input file. The input file is manipulated to create an output request for coordinate information in the integration points and a second job instance pointing to the new input file is created. The second job is converted into a system of partial differential equations and solved using Abaqus/Standard.

4.3 Computing Stresses and Walker Damage

After solving the system of partial differential equations for the displacements of the nodes in the model, Abaqus Standard computes stresses and coordinates in the integration points at different points in step-time which refer to the minimum and the maximum load. In this section, the computation of Walker damage parameters at the surface of the disc spring between edge II and edge III is described. Here, we may assume a plane stress state with a dominationg tension component:

$$\sigma_{load,II,min} = 0 \vee \sigma_{load,III,min} = 0 \quad (19)$$

$$\sigma_{load,II,max} = 0 \vee \sigma_{load,III,max} = 0 \quad (19)$$

For integration points close to the surface, this is approximately true. The assumption becomes more realistic with a finer mesh and is true with an infinitesimal mesh size. The minimial and maximal stress components $\sigma'_{load,II,min}$ and $\sigma'_{load,II,max}$ are redefined:

$$\sigma'_{load,II,min} := \sigma_{load,II,min} + \sigma_{load,III,min} \quad (20)$$

$$\sigma'_{load,II,max} := \sigma_{load,II,max} + \sigma_{load,III,max} \quad (21)$$

In the surface of disc springs, $\sigma_{I,load}$ points in the tangential direction and $\sigma'_{load,II}$ points in the radial direction. Residual stresses are measured in the tangential direction $(\sigma_{residual,tan})$ and in radial thedirection $(\sigma_{residual,rad})$. The input stresses for the computation of the Walker parameters are defined as:

$$\sigma_{I,max} = \sigma_{load,I,max} + \sigma_{residual,tan} \quad (22)$$

$$\sigma_{II,max} = \sigma'_{load,II,max} + \sigma_{residual,rad} \quad (23)$$

$$\sigma_{I,min} = \sigma_{I,load,min} + \sigma_{residual,tan} \quad (24)$$

$$\sigma_{II,min} = \sigma'_{load,II,min} + \sigma_{residual,rad} \quad (25)$$

Walker parameters are computed following equations 1 to 11. For each surface triangle, a surface area A_i and a Walker damage parameter $P_{Walker,i}$ is computed. The surface Walker damage parameter is computed by averaging the Walker parameters of the six neighboring nodes. These data pairs are saved as the set S.

4.4 Extracting Tabular Data

The set S is too rich on information to be captured holistically without extraction and/ or condensation. This is done by transforming the information into tabular data. Therefore, it is condensed into human readable tabular data. Each element of the set is defined as a dirac delta function:

$$f_i(P_{Walker}) = A_i \cdot \delta(P_{Walker} - P_{Walker,i}) \quad (27)$$

The accumulated surface area A_{acc} assigned to a given Walker damage parameter is computed as:

$$A_{acc}(P_{Walker}) = \int_{P_{Walker}}^{\infty} \sum_i f_i(P_{Walker})\, \mathrm{d}P_{Walker} \quad (26)$$

It describes the size of the surface area of the disc spring with a Walker damage equal to or bigger than the given P_{Walker}. A graphical representation of the accumulated surface area is created, Fig. 4 [17].

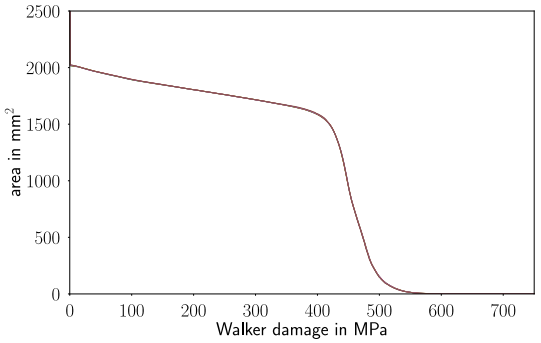

Fig. 4: Area as a function of the Walker damage

5. SUMMARY

A novel algorithm as implemented in the Spring_stack module was presented in this paper. After geometry acqusistion by 3D-scanning, the digital representation of a disc spring is aligned in space. A finite element model is built around the aligned geometry and further user-inputs like load cases. The model is solved and the result is used to compute Walker damage parameters in the integration points of the model. In a postprocessing step the accumulated surface area as a function of the Walker parameter is computed.

ACKNOWLEDGEMENTS

This article was created as part of the research project AVIF A 309 ‘Bewertung des Einflusses realer Bauteil-geometrien auf die Beanspruchbarkeit von Tellerfedern anhand numerischer Simulation’ (assesment of the influence of real geometries on the load capacity of disc springs by numerical simulation). This project is funded by Stiftung Stahlanwendungsforschung, which is part of Stifterverband für die Deutsche Wissenschaft e.V. (Donors’ Association for the Promotion of Science and Humanities in Germany). The Association’s mission is the promotion of research into the manufacturing and utilization of steel in Germany. The research proposal

was audited by a panel of experts from the Research Association of the Working Group of the Iron- and Metal-processing Industries (AVIF), which is composed of specialists from the steelworking industry and academia. The project is accompanied by a working group from the VDFI (Association of the German Spring Industry).

REFERENCES

1) DIN EN 16983:2017. Disc springs - Quality specifications - Dimensions.
2) DIN EN 16984:2017. Disc springs - Calculation.
3) Geilen, M. B., Klein, M. and Oechsner, M.: Building Models with 3D-Scanned Geometry using Abaqus Scripting - A Case Study on Disc Springs. 3DEXPERIENCE Conference - Design, Modeling & Simulation. Darmstadt 2019.
4) Geilen, M. B., Klein, M. and Oechsner, M.: Spring_stack - ein Modul zur numerischen Simulation von Tellerfedern und Tellerfedersäulen. Ilmenauer Federntag. Ilmenau 2019, pp. 77–86.
5) Walker, K.: The effect of stress ratio during crack propagation and fatigue for 2024-T3 and 7075-T6 aluminum. In: Effects of environment and complex load history on fatigue life. ASTM International 1970, pp. 1–14.
6) Goodman, J.: Mechanics applied to engineering. Longmans, Green 1919.
7) Morrow, J.: Fatigue design handbook. Advances in engineering 4 (1968), pp. 21–29.
8) Smith, K. N., Watson, P. and Topper, T. H.: A stress-strain function for the fatigue of metals. Journal of materials 5 (1970), pp. 767–778.
9) Dowling, N. E., Calhoun, C. A. and Arcari, A.: Mean sress effects in stress-life fatigue and the Walker equation. Fatigue & Fracture of Engineering Materials & Structures 32 (2009) 3, pp. 163–179.
10) Dowling, N. E.: Mechanical behavior of materials: engineering methods for deformation, fracture, and fatigue. Pearson 2012.
11) Gyekenyesi, J. Z., Murthy, P. L. N. and Mital, S. K.: NASALIFE-Component fatigue and creep life prediction program, 2014.
12) Barber, C. B., Dobkin, D. P. and Huhdanpaa, H.: The quickhull algorithm for convex hulls. ACM Transactions on Mathematical Software (TOMS) 22 (1996) 4, pp. 469–483.
13) Virtanen, P., Gommers, R., Oliphant, T. E., Haberland, M., Reddy, T., Cournapeau, D., Burovski, E., Peterson, P., Weckesser, W. and Bright, J.: SciPy 1.0--Fundamental Algorithms for Scientific Computing in Python. arXiv preprint arXiv:1907.10121 (2019), pp. 1–22.
14) Byrd, R. H., Lu, P., Nocedal, J. and Zhu, C.: A limited memory algorithm for bound constrained optimization. SIAM Journal on Scientific Computing 16 (1995) 5, pp. 1190–1208.
15) Zhu, C., Byrd, R. H., Lu, P. and Nocedal, J.: L-BFGS-B: Fortran subroutines for large-scale bound-constrained optimization. ACM Transactions on Mathematical Software (TOMS) 23 (1997) 4, pp. 550–560.
16) Cignoni, P., Callieri, M., Corsini, M., Dellepiane, M., Ganovelli, F. and Ranzuglia, G.: Meshlab: an open-source mesh processing tool. Eurographics Italian chapter conference. 2008, pp. 129–136.
17) Hunter, J. D.: Matplotlib: A 2D graphics environment. Computing in science & engineering 9 (2007) 3, pp. 90–95.

Development of fatigue strength diagrams for helical compression springs made of spring steel wire

Martin PETRICH, René REICH and Ulf KLETZIN
Technische Universität Ilmenau, Wire and Springs Research Group, Machine Elements Group
Max-Planck-Ring 12, 98693 Ilmenau, Germany
TEL: +49-(0)-3677-69-1865 FAX: 49-(0)-3677-69-1259 e-mail: martin.petrich@tu-ilmenau.de

For the design and calculation of helical compression springs, the European Standard DIN EN 13906-1 includes analytical relationships and Goodman diagrams. The creation of these Goodman diagrams dates back more than 50 years, which is why they do not provide enough information, compared to the today´s knowledge regarding fatigue behavior. As for users of the standard, this leads to uncertainties, which have to be compensated by cost-intensive fatigue tests. In order to overcome those inadequacies, the deduction of new fatigue strength diagrams has been the subject of an extensive research program. To reduce the costs to reach this goal, only a relatively small amount of springs has been tested by fatigue experiments to create the lines of the fatigue diagrams. The test results are then being combined with calculations by a mathematical algorithm based on the draft of the guideline "Rechnerischer Festigkeitsnachweis für Federn und Federelemente", developed in a former research project. In addition, a mathematical transfer method of the permissable stresses of the reference springs in the diagrams to other helical compression springs is being presented. This paper shows approaches to design competitive springs in shorter time and with less test effort.

Keywords: compression springs, fatigue calculation method, fatigue diagrams

1. MOTIVATION

1.1. INITIAL SITUATION

In general, when designing components, attention is paid to size, mass and reliability. An important design criterion is the service life to be achieved. For cyclically stressed components, fatigue strength diagrams such as the Haigh- or Smith-diagram have been established.

In contrast, the relationships and Goodman diagrams contained in the standard DIN EN 13906-1[1)] form the essential basis for the design and calculation of cylindrical helical compression springs. These are not only used nationally, but are spread throughout Europe as well as internationally and are used in particular in SMEs in the spring industry and by spring users.

Ten of the Goodman diagrams in DIN EN 13906-1 show torsional fatigue strength values of cold-formed springs (Fig. 1). The permissible fatigue stress τ_{kH} is plotted there as a function of the stress τ_{kU}, for a given number of cycles N of the helical compression springs.

These fatigue strengths shown in DIN EN 13906-1 possess meaningful reserves. In the past decades, the wire materials have significantly improved (metallurgy, purity, drawing process, heat treatments, tensile strength, tolerances, uniformity).

Furthermore, it is now known that geometry, surface, process sequences and process parameters (heat treatment, pre-setting, shot peening, ...) during spring manufacture and the operating conditions have a significant influence on the fatigue resistance of the springs [2) 3) 4) 5) 6)]

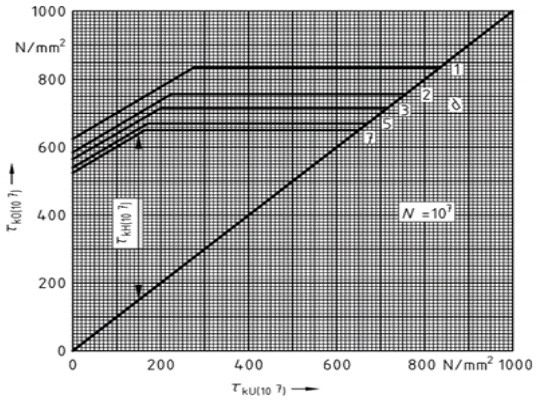

Fig. 1: Example of a Goodman diagram from DIN EN 13906-1 for shot-peened springs (VD wire).

According to the standard, these factors are currently not taken into account in the spring design process. For the users of the standard this results in great uncertainty, which must currently be compensated by experience from cost-intensive fatigue tests. In addition to being uneconomical, these uncertainties involve high legal

risks for spring manufacturers and users who have to use high-performance springs for competitive products, but which then do not comply with the applicable standard.

Last but not least, the most important deficiencies are the lack of specifications of the underlying tested springs and of lack of details for security factors or failure probabilities.

1.2. SPRING DESIGN METHODS AROUND THE GLOBE

Standards and guidelines for spring design are used internationally. Historically, research on wires and springs and the associated guideline work have played a pioneering role, particularly in Germany. To date, the guideline work is being promoted and coordinated by the Verband der Deutschen Federnindustrie e.V. (VDFI) in cooperation with its member companies and research partners, such as the Wire and Springs Research Group at the Ilmenau University of Technology.

In recent years, a large number of German wire, ribbon and spring standards have been converted into European standards. Thanks to its status as a European Standard, DIN EN 13906 has achieved enormous distribution and establishment in Europe. In addition, the level of acceptance of the knowledge and fatigue values from this standard is high internationally, for example in [7] .

The Japanese standard JIS B 2704-1[8] contains a Goodman diagram where only a small amout of factors are taken into account. In the American area there are tables for standard springs (wire diameter, coil diameter, spring length, spring rate, etc.) without reference to life estimates (e.g. [9] [10]).

The spring manual SAE HS 795 Part 2 (1990) [11] contains only two fatigue diagrams for non-presetted and presetted springs. The tensile strength of the material and the spring geometry as well as shot peening are included in the calculations, but other influencing factors are not taken into account. Due to the fact that this manual has not been updated for more than 25 years and that not all of the main influencing factors are taken into account, no high-performance springs, that users are increasingly demanding, can be designed.

In the last years, a new method for analytical calculation of the cyclic degree of utilisation was developed in a publicly funded research project in Germany [12] by the authors and others involved. The basis for this new method is the FKM guideline "Analytical Strength Assessment" [13] , which contains fatigue calculations for any machine elements. This procedure was used and modified, considering the specific peculiarities that exist for spring steel wire and springs made from it. In conclusion, a new guideline "Rechnerischer Festigkeitsnachweis für Federn und Federelemente" (Analytical strength assessment for springs and spring elements) [14] was composed and published 2020. In further development and application of the new method, another research was carried out [15], which results are being presented here.

1.3. APPROACH AND OBJECTIVE

In order to overcome the problems described previously, new fatigue diagrams for reference springs should be generated, that correspond to the state of the art in spring technology and methods should be developed to deal with all influences.

The aim of the research project is, to develop a basis for renewing the Goodman diagrams of the DIN EN 13906-1 standard with a comparatively small experimental scope of fatigue tests on cold-formed helical compression springs (reference springs).

To further increase the design quality, new or refined methods for determining the fatigue strength are used, taking into account the following parameters that influence the fatigue strength:

- Internal stresses from different manufacturing processes or manufacturing steps such as shot peening and presetting.
- Wire tensile strength Rm including heat treatment.
- Influences of differently rough surfaces.
- Effects of different spring geometries (spring index w, number of coils n) and wire diameters d.
- Change in the fatigue strength of the spring with a different number of load cycles N^* that deviates from the fatigue strength diagram (specified number of cycles N, e.g., $N=10^7$).

2. FATIGUE TESTS

2.1. WIRE MATERIALS, SPRING DESIGN AND EXPERIMENTAL PROCEDURE

The materials in this research program were well distributed across the three spring steel relevant material groups: oil hardened, patent drawn and stainless steel according to the standards DIN EN 10270- 1-3. First, the materials FDSiCr, VDSiCr, VDSiCrV, DH, 1.4310 and 1.4568 were determined. Then, based on the standard DIN EN 13906-1, the wire diameters were divided into small, medium and large ones (d = 1, 3, 6-10 mm). Before the spring production started, all wires were analysed by destructive tensile and torsion tests. Due to

the knowledge of the elastic-plastic material behaviour, each spring design could be optimized.

Different companies, that were involved in the research project, manufactured a total of 42 different spring versions. Following spring characteristics and manufacturing details were specified by the research group and the project committee:

- direction of coiling: right
- quality grade 1
- closed and ground end coils
- manufacturing process for non-shot peened springs: winding, heat treatment, grinding, presetting
- manufacturing process for shot peened springs: winding, heat treatment, grinding, shot peening, (optional: heat treatment) and presetting
- pressetting three times to a specified force

The fatigue testes were mostly run on three machines (resonance vibration machine, eccentric beam testing machine and servo hydraulic testing machine) at the laboratories at TU Ilmenau, but also at IABG and Mubea in Germany.

Before the fatigue tests started, three samples of each spring variant were geometrically measured and the charactieristic curves were recorded. Additionally, the initial spring length of each probe was documented before the tests.

On the basis of the spring curve, the stress levels were determined (see Fig. 2) for the Wöhler-tests with constant mean stress and variable stress range τ_{kh}. Overall, each stress level was tested with minimum of 8 springs (normally 10 samples) and for springs with d = 3 mm mostly 16 probes per run.

The stress ratio R can be calculated by equation (1).

$$R = \frac{\tau_{ku}}{\tau_{ko}} = \frac{\tau_{km} - \tau_{ka}}{\tau_{km} + \tau_{ka}} \qquad (1)$$

Essentially, the cycle counts from fatigue occasions were noted on the test report as well as specifics of them, e.g. end coil failures, double breaks or incipient cracks. Furthermore, the location of fracture and, for intact springs, the spring lengths were noted. The maximum life cycle count was determined to $N = 10^7$.

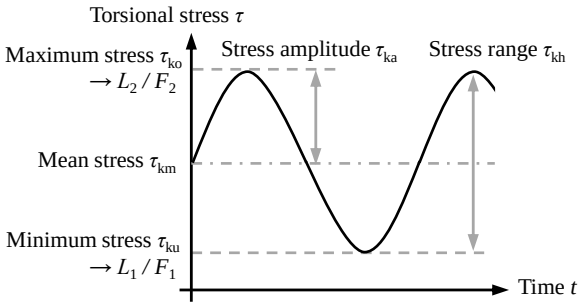

Fig. 2: Load cycle with constant mean stress

In conclusion, a detailed test report was generated for each spring variant, including all necessary information for subsequent studies.

2.2. INTERPRETATION OF THE FATIGUE TEST RESULTS

There are a lot of different statistical methods for the interpretation of results from Wöhler-tests to determine the parameters of the Wöhler-line. In this project, the common Arcsin-√P-transformation [16], the Maximum Likelihood method [17] [18]and a modified Probit-evaluation were tested on example data.

While the test results show standard fatigue behaviour, the different methods lead to equivalent parameters for the Wöhler-line at 50% survival probability. Certainly, non-standard cracks can't be considered by the Arcsin-√P- and Probit-method, so that the quantity of specimen decreases, leading to a reduction of the interpretation quality.

According to [18], the Maximum-Likelihood-method provides best results overall, because censored data (e.g. end coil fracture) can be included by a statistical assumption.

For this reason, the Maximum-Likelihood-method was used for the interpretation of all test results, which is a universal tool for a wide variety of problems. The main goal is, to find parameters with which a mathematical model / function describes an existing data record with the highest probability. This so-called Likelihood function can be composed of sub-functions that describe the problem sufficiently (support functions). As an optimization problem, the parameters should fit the function in the best possible way on the data record. Then the Likelihood function is maximized without it´s value playing a role. The chosen Likelihood funktion based on [17] and [19] considers a bilinear Wöhler-line in the double logartihmic scale and a break point at approx. $N = 10^6$ as shown in Fig. 3.

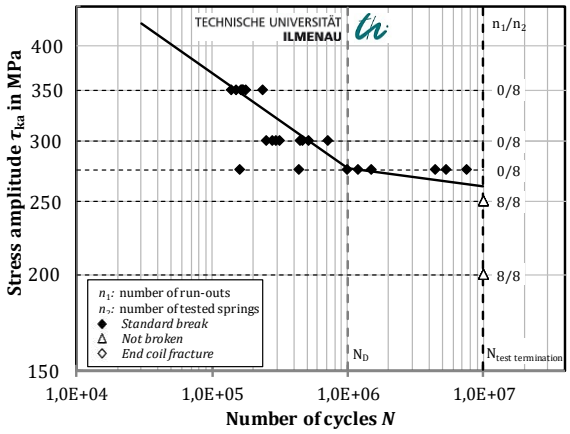

Fig. 3: Example for a bilinear Wöhler-line in a double logarithmic Wöhler-diagram for 50% survival probability

The relationship between the number of cycles N and the stresses τ is established using the slope exponents $k_{1,2\tau}$ (equation (2)). This makes it possible to convert from the break point N_D / τ_D to any number of load cycles or the amplitude of the point N_i / τ_i.

$$\frac{N_D}{N_i} = \left(\frac{\tau_i}{\tau_D}\right)^{k_{1\tau}} \quad \text{for } N_i \leq N_D \qquad (2)$$

$$\frac{N_D}{N_i} = \left(\frac{\tau_i}{\tau_D}\right)^{k_{2\tau}} \quad \text{for } N_i > N_D$$

Various sources recommend the use of the normal distribution or Gaussian distribution, whose density function is described by equation (3). It is assumed that the scatter in the y direction στ is constant over N.

$$f(x) = \frac{1}{\sigma\sqrt{2\pi}} e^{-\frac{1}{2}\left(\frac{x-\mu}{\sigma}\right)^2} \qquad (3)$$

μ - mean σ – standard deviation

The Likelihood function is the product of the probabilites for breaks before and after N_D and run-outs. In the logarithmic scale, the product changes to a sum of supports, which has to be maximised (equation (4)).

$$\text{Max}(sup_{N_i \leq N_D} + sup_{N_i > N_D} + sup_{run-out}) \qquad (4)$$

The Maximum-Likelihood function was implemented in Microsoft Excel and can be used with the Solver, to fit the Wöhler-lines to the test data.

3. DEVELOPMENT OF FATIGUE DIAGRAMS

The main goal of the research project was, to renew the existing fatigue strength diagrams for compression springs and to enable the users to consider all necessary influences in an easy and applicable, but resilient way.

On the one hand, diagrams are very easy to use and provide good information in a short time. But, not all details and variants can be described, because an infinite number of diagrams could be developed. On the other hand, the following described calculation method appears difficult and not very descriptive.

A compromising way is, to draw reference diagrams for common standard springs and to add an easy applicable method for the design of non-standard springs or springs with very high fatigue requirements. This idea is being described on the next pages.

3.1 CALCULATION OF FATIGUE STRENGTH

As described before, the fatigue diagrams should be developed methodically, supported by fatigue tests. The calculation procedure in the new FKM guideline [14] is being started with the tensile strength of the material, as this value is always available (Fig. 4).

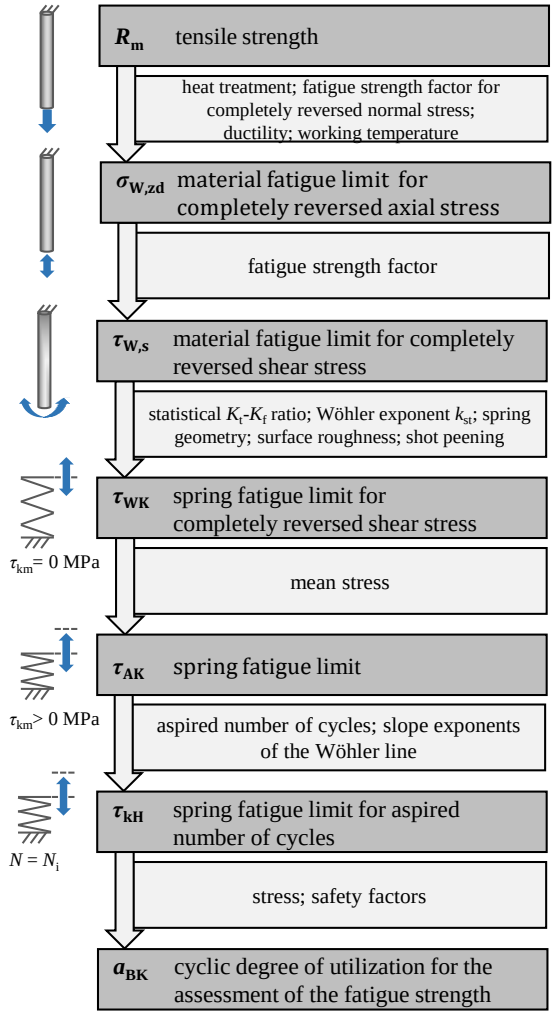

Fig. 4: Calculation of the fatigue strength [14]

If there are characteristic values from cyclical tests (e.g. from circular bending tests or cyclical torsion tests), the calculation of the permissible stresses can also begin in one of the corresponding intermediate steps. With the help of approximate solutions, difficult mathematical

relationships are identified (e.g. integrals to determine the highly stressed surface), simplified and thus a complete integration into Excel is possible.

In order to be able to carry out the calculations, the material, the wire diameter d, the spring index w, the number of active coils n_f, and the tensile strength R_m of the non-heat-treated wire are needed. The heat treatment temperature is also required. The deformability of the material (K*), the surface roughness in the form of the roughness factor K_R and an increase in vibration resistance due to shot peening are to be assessed. In addition, the number of cycles N and the survival probability $P_ü$ are required. The permissible stress amplitude τ_{BK} for a medium stress τ_{km} can be calculated, including all factors described before.

On this basis, a Wöhler-line for a specific spring can be computed. When the break point at $N_D = 10^6$ is being calculated, each point from the τ-N-curve can be reached by the equations in (2) due to the slope exponents $k_{1,2\tau}$.

Numerous correlations in the aforementioned guideline work with arithmetical factors. Due to the inclusion of fatigue strength values from previous research projects as well as the implementation of additional cyclical tests on wires and springs to close gaps in the database, the developed guideline offers a very current and at the same time broadly based reference for the calculation of fatigue strengths.

When determining the calculation factors and material constants contained therein, a total database of 418 statistically evaluated fatigue strengths was taken into account, of which 229 results come from helical compression springs. Additionally, the fatigue tests described in chapter 2 were taken into account for further evaluation of the calculated values.

3.2 SAFETY CONCEPT

The calculations described previously (see Fig. 4) are being build up on a survival probability of $P_ü = 50\%$. This determination simplifies the efforts for analysis in the mathematical way but also the interpretation of test results, especially from former projects that were not carried out by the research group at TU Ilmenau.

However, the probability value can not be used practically, since many springs would then be overloaded. In addition, the data from tests have an unavoidable scatter. Therefore, an essential topic of the research is to secure the calculations by a safety concept. Because the diagrams of the standard DIN EN 13906-1 do not contain any information on safety, this means a big step forward in spring design, but it also creates the need for training in the application of this new knowledge. Besides the reports from [12] and the new guideline [14], a detailed examination on the effects of the safety factors was published by the authors in [21].

The safety factor j_{ges} contains two parts (equation (5)). One factor j_{Cn} depends on the trust level of the database C(x) to handle the scatter. The second factor j_S enables the survival probability $P_ü$ to be increased on to a practical value.

$$j_{ges} = j_{Cn} \cdot j_s \tag{5}$$

The values of the safety factors were derived on the basis of the experimental data and the calculated fatigue strength, considering the Gaussian normal distribution.

Table 1: Examples for safety factors j_{Cn} and j_S (j_S is valid for not shot-peened springs made from oil hardened wire).

C(x)	j_{Cn}	$P_ü = 99,9\%$		j_S	
90%	1,10	Shot peening	Oil hardened	Patent drawn	1.4310
95%	1,15	No	1,31	1,37	1,50
99%	1,23	Yes	1,25	1,25	1,31

Through this concept, can easily take their own production scatter into account on the one hand and on the other hand the statistical demands from the application site can be considered.

3.3. DRAFT OF NEW FATIGUE DIAGRAMS FOR SPRINGS

Since springs are used, the Goodman diagram is common for the spring design. For other machine parts, further diagram forms like the Haigh diagram have been established. In general, these two diagrams contain the same information and can easily be transformed into each other (Table 2). In order to create a future-oriented interface at this point, all diagrams were developed in both forms.

Table 2: Equations for transformation between Goodman and Haigh diagram

Goodman		Haigh
τ_{KU}	⇒	$\tau_{km} = \frac{\tau_{kO} + \tau_{kU}}{2}$
τ_{K0}	⇒	$\tau_{kA} = \frac{\tau_{kO} - \tau_{kU}}{2}$
$\tau_{KU} = \tau_{km} - \tau_{kA}$	⇐	τ_{km}
$\tau_{kO} = \tau_{km} + \tau_{kA}$	⇐	τ_{kA}

The fatigue strength diagram according to Goodman is well known from DIN EN 13906-1. In this diagram (Fig. 5) permissible maximum stress τ_{kO} (1.) and minimum stress τ_{kU} (2.) are shown for a number of cycles N. The working range of the spring is delimited by a diagonal (2.) and a characteristic curve (1.), which consists of an ascending (3.-4.) and a horizontal straight line (4.-5.). A working point of a spring is shown as an example (6.), which can be operated with a minimum stress with the associated permissible maximum stress.

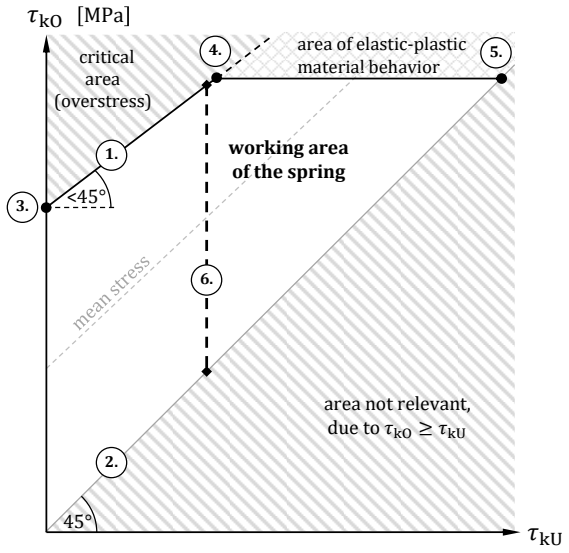

Fig. 5: Schematic structure of the Goodman diagram

Fig. 6 shows the schematic structure of the Haigh diagram. Therein, the permissible stress amplitude τ_{kA} (1.) is plotted against the mean stress τ_{km} (2.) for a number of cycles N. Since the stress amplitude of compression springs cannot be greater than the mean stress, generally only the area below the diagonal (stress ratio $R = 0$) is relevant. The break (4.) is caused by the decreasing amplitude in the Goodman diagram, which follows from the limited upper stress (horizontal 4.-5.). A working point of a spring is shown as an example (6.).

The Haigh diagram is particularly interesting when residual stresses (e.g. by shot peening), are to be taken into account using the principle of the mean stress shift.

In the following sections, some representative drafts of new fatigue diagrams will be presented as examples out of 24 new diagrams. As a reference, strength lines from the current standard are shown as black dashed lines. The calculated lines are based on medium tensile strength values from the wire standards 20), medium values for the different factors (see Fig. 4) and $N = 10^7$.

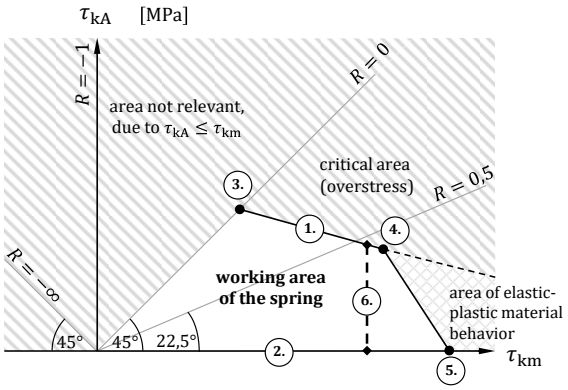

Fig. 6: Schematic structure of the Haigh diagram

The reference springs are being considered with $w = 6$ and $n = 6{,}5$ and not shot peened. For the safety factors, the trust level of the database was set to $C(x) = 95\%$ and the survival probability to $P_ü = 99{,}9\%$ ($P_ü = 1 - P_A$), which actually appears as a compromising way between necessary but not superfluous security for most spring applications (no safety relevant springs!).

The additional strengthening effect caused by shot peening is unregarded at this point. In general, two ways of consideration have been acquired. The first way is similar to the principle of mean stress shift in [13], assuming that the residual stress induced by the shot peening can be handled as an overlay to the mean stress. This residual compressive stresses on the wire surface are opposed to the load stresses.

The second method was developed in [12] to provide an easy applicable alternative. Therefore, an offset $\Delta\tau_{ES}$ is being added to the permissable stress amplitude.

3.4. SPRINGS MADE FROM OIL HARDENED WIRE

The first example for VDSiCr is shown in Fig. 7. It is visible, that the shown lines provide more permissable stress than the curves from the standard, especially for higher stresses. For tensile strength $R_m > 2000$ MPa no further increase in fatigue strength is expected in [14]. This is particularly interesting for small wire diameters with high tensile strength. Nevertheless, an increase is known in practice, but it is not as high as for smaller strengths. Practically, the blue line is slightly higher than shown here.

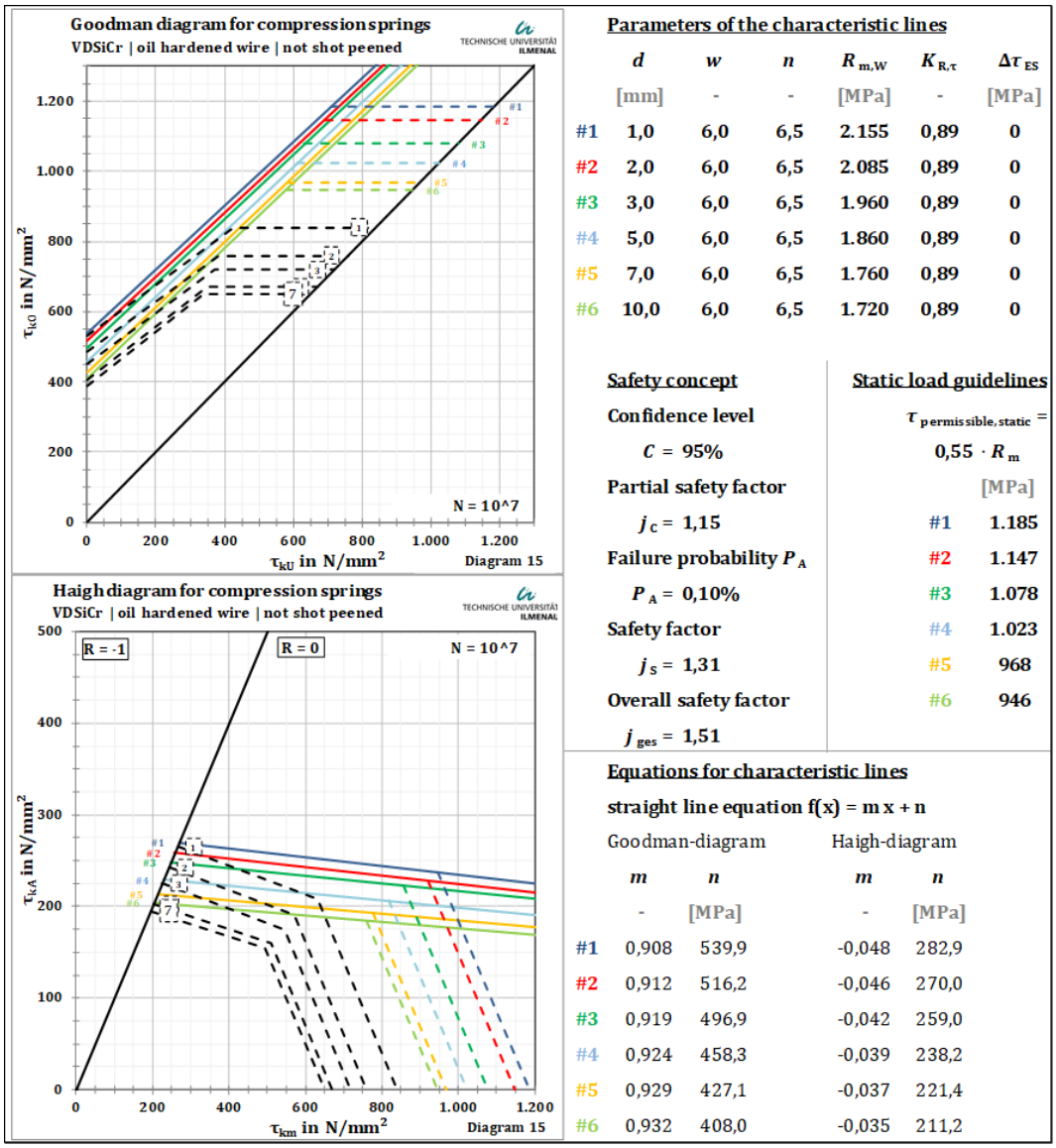

Parameters of the characteristic lines

	d	w	n	$R_{m,W}$	$K_{R,\tau}$	$\Delta\tau_{ES}$
	[mm]	-	-	[MPa]	-	[MPa]
#1	1,0	6,0	6,5	2.155	0,89	0
#2	2,0	6,0	6,5	2.085	0,89	0
#3	3,0	6,0	6,5	1.960	0,89	0
#4	5,0	6,0	6,5	1.860	0,89	0
#5	7,0	6,0	6,5	1.760	0,89	0
#6	10,0	6,0	6,5	1.720	0,89	0

Safety concept

Confidence level

C = 95%

Partial safety factor

j_C = 1,15

Failure probability P_A

P_A = 0,10%

Safety factor

j_S = 1,31

Overall safety factor

j_{ges} = 1,51

Static load guidelines

$\tau_{permissible,static}$ = $0{,}55 \cdot R_m$

	[MPa]
#1	1.185
#2	1.147
#3	1.078
#4	1.023
#5	968
#6	946

Equations for characteristic lines

straight line equation f(x) = m x + n

	Goodman-diagram		Haigh-diagram	
	m	n	m	n
	-	[MPa]	-	[MPa]
#1	0,908	539,9	-0,048	282,9
#2	0,912	516,2	-0,046	270,0
#3	0,919	496,9	-0,042	259,0
#4	0,924	458,3	-0,039	238,2
#5	0,929	427,1	-0,037	221,4
#6	0,932	408,0	-0,035	211,2

Fig. 7: Fatigue diagrams for springs made of VDSiCr wire

3.5 SPRINGS MADE FROM PATENT DRAWN WIRE

The next draft is presented for DH wire in Fig.8. For the DH material, a more or less comparable fatigue strength is visible. Due to the slightly changed tilt, the reserves in strength are available for higher stress levels, like seen at the diagrams for the VDSiCr wire.

3.6 SPRINGS MADE FROM STAINLESS STEEL WIRE

The stainless steel is presented by 1.4310 in Fig. 6. A decreased fatigue limit for all wire diameters can be clearly determined. This result was being confirmed by spring designers for the 1.4310 material. It can be stated, that the lines in the standard do not provide any reserves for the chosen safety factors. This important finding needs to be emphasized at this point.

3.7 UPPER STRESS LIMIT DUE TO STATIC STRENGTH

Experience and reports from previous research projects and from industrial practice have shown that the horizontal limits of the fatigue strength outlined in DIN EN 13906-1 are conservative with regard to the capacity of modern wire materials. There are also several unresolved questions:

- It is not clear in what context the height / tension of the horizontal is with e.g., the tensile strength, or which wire characteristic they represent.
- There is no direct indication of whether corrected or

uncorrected permissible stresses are plotted as horizontal lines in the diagrams. Since the corrected is to be assumed, the spring index must be considered. Consequently, the height of the horizontal in the diagrams cannot be related to $\tau_{zul} = 0.56 \cdot R_m$, for example.

- All characteristics are plotted without information on the failure probability. The scatter band, which is to be laid around the rising straight line, would be cut off obliquely by the horizontal boundary. The result is that the failure probability in the break of the curve has little or no influence on the permissible stress.

The research group therefore suggests that the future fatigue diagrams should follow a new approach to fill the gap like shown below, which considers the yield point and residual stresses from presetting.

$$\tau_{permiss,\,static} = \tau_{tF} + \tau_{residual,presetting} \quad (6)$$

$$\tau_{\mathrm{permiss,\,static}} = x \cdot R_m/\sqrt{3} + 0{,}06 \cdot R_m \quad (7)$$

$$\tau_{\mathrm{permiss,\,static}} = \left(x/\sqrt{3} + 0{,}06\right) \cdot R_m = y \cdot R_m \quad (8)$$

$\tau_{permiss,\,static}$ permissible upper stress limit

τ_{tF} yield strength

$\tau_{(residual,presetting)}$ residual stresses from presetting

R_m tensile strength after heat treatment (R_m > 2000 MPa R_m = 2000 MPa)

x,y factors determined on the basis of test results

The boundary value is drawn in the form of a dashed line for orientation. Considering the static limit was not a focus of the investigations in the project, but a proposition had to be given. The calculation factors *x* and *y* were determined on the basis of test results, to ensure that the formula is easy to use with the tensile strength.

Table 3: Factors to calculate the upper stress limit

Material	$x = \bar{x}$	$y = \bar{x}/\sqrt{3} + 0{,}06$
Oil hardened	0,85	0,55
Patent drawn	0,78	0,51
1.4310	0,60	0,41
1.4568	0,66	0,44

3.8 METHOD OF FATIGUE TRANSFER

The project idea is largely based on transferring the fatigue strength of a reference spring τ_{kH1} to a similar spring τ_{kH2} using factors based on the calculation procedure shown in Fig. 4. An approach for a transferring method shows equation (9).

Various factors (*K*) are defined for the transmission. Influences of geometry (*GF*), surface roughness (*OF*), tensile strength (*ZF*), shot peening (*KS*) and mean stress (*MS*) can be taken into account.

$$\tau_{kH2} = 2 \cdot \left(K_{GF} \cdot K_{OF} \cdot K_{ZF} \cdot \frac{\tau_{kH1}}{2} \cdot j_{ges} + K_{KS} + K_{MS}\right) \quad (9)$$

using Goodman-diagram

$$\tau_{kA2} = K_{GF} \cdot K_{OF} \cdot K_{ZF} \cdot \tau_{kA1} \cdot j_{ges} + K_{KS} + K_{MS} \quad (10)$$

using Haigh-diagram

$$K_{GF} = \frac{n_2}{n_1} \qquad K_{OF} = \frac{K_{R\tau,2}}{K_{R\tau,1}} \qquad K_{ZF} = \frac{R_{m,2}}{R_{m,1}}$$

$$K_{KS} = \sigma_{ES,2} \cdot M_{\tau,2} - \sigma_{ES,1} \cdot M_{\tau,1}$$

$$K_{MS} = \tau_{km,1} \cdot M_{\tau,1} - \tau_{km,2} \cdot M_{\tau,2}$$

n statistical Kt - Kf ratio

K_R roughness factor

R_m tensile strength after heat treatment (R_m > 2000 MPa → R_m = 2000 MPa)

σ_{ES} residual stress

τ_{km} mean stress

M_τ mean stress sensitivity

Furthermore, a transfer to other values for N_i can be related through equation (2). It has to be noted, that the possibly changed demands on safety have to be regarded.

In addition to the current application of the diagrams according to the standard, the permissible stresses according to the diagrams, which have been checked for a special sample spring geometry, can also be used for other spring indexes, number of coils, material parameters, surface roughnesses, residual stresses, and more. This makes it possible for the first time to methodically consider these influences in the spring design.

4. CONCLUSION AND OUTLOOK

As described in the explanations, an update of the fatigue strength diagrams for springs is essential. Many details must be observed, which can only be partially explained at this point. Some details are still in the discussion stage, which is why the diagrams here may only be seen as drafts and not for spring design.

The comparison of the newly calculated characteristic curves with the characteristic curves of the current standard shows some strength reserves, but also a partial reduction in the permissible strengths. Generally, the comparison is questionable, due to a lot of unknown parameters in the old curves of the standard.

However, the greatest advantage of the new design is the knowledge of all details of the characteristic curves as well as a statistical assessment, which, due to the inevitable variability and scatter, will have to become a focus of spring design in the future.

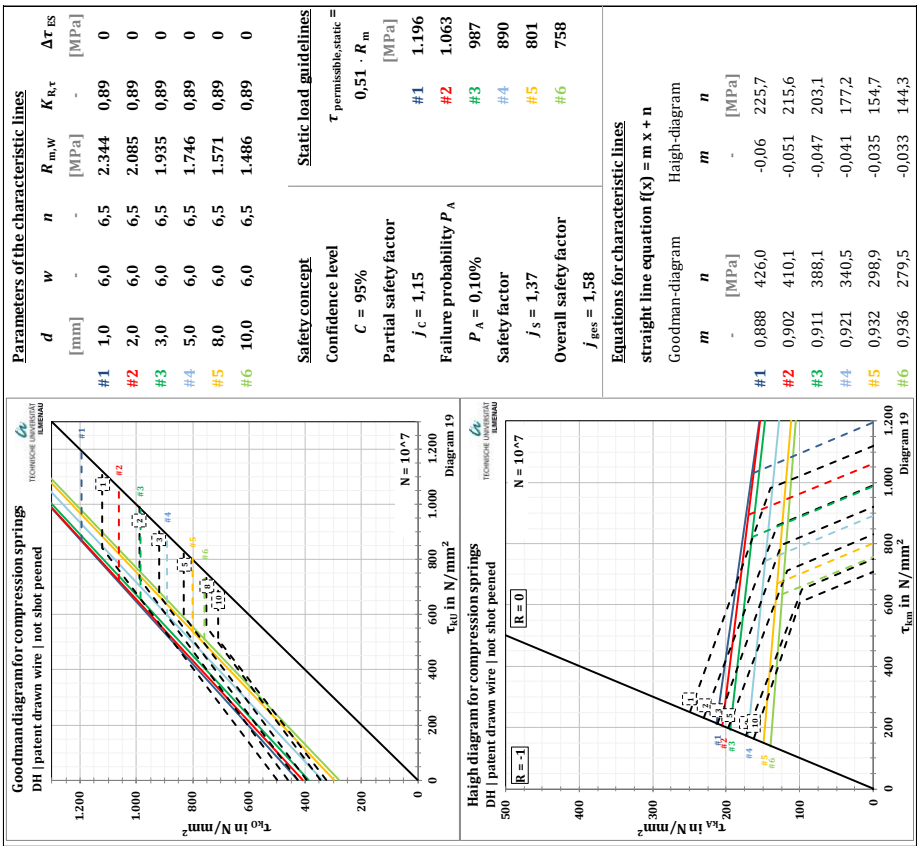

Fig. 5: Fatigue diagrams for springs made of DH wire

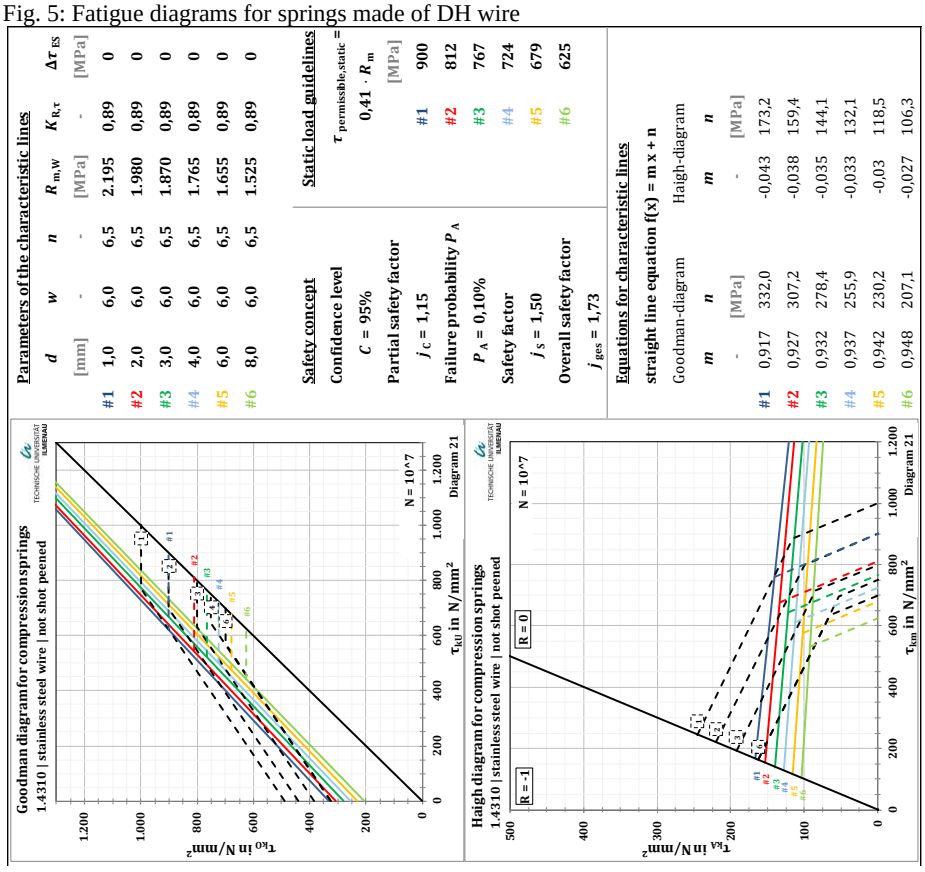

Fig. 6: Fatigue diagrams for springs made of 1.4310 wire

The approach to design competitive springs in shorter time and with less test effort can be reached and the reliability of the design can now be evaluated. This contribution is intended to support spring designers and to reduce uncertainty with regard to future developments. Furthermore, the goal remains to pursue, on the one hand, to transfer this knowledge into the standard DIN EN 13906-1 and, on the other, to bring it closer to the users.

5. ACKNOWLEDGEMENTS

This IGF Project (IGF 19693) of the FSV is supported via AiF within the programme for promoting the Industrial Collective Research (IGF) of the German Ministry of Economic Affairs and Energy (BMWi), based on a resolution of the German Parliament.

The research was thankfully supported by the Forschungsgesellschaft Stahlverformung e.V. (FSV) and Verband der Deutschen Federnindustrie e.V. (VDFI) as well as the numerous members of the project committee.

REFERENCES

1) DIN EN 13906-1; Zylindrische Schraubenfedern aus runden Drähten und Stäben. 2013-11
2) Reich, R.; Kletzin, U.: Lebensdauervorhersage für Schrauben-druckfedern. Final report of IGF 15747, TU Ilmenau 2010
3) Reich, R.; Kletzin, U.: Betriebsfeste Auslegung von Schraubendruckfedern unter Verwendung dynamischer Materialkennwerte aus Umlaufbiegeprüfungen. Final report IGF16999, TU Ilmenau 2013
4) Geinitz, V.; Kletzin, U.; Beyer, P.: Wärmebehandlung kalt geformter Federn. Final report of IGF 17627. TU Ilmenau 2015
5) Reich, R.: Möglichkeiten und Grenzen bei der Auslegung von Schraubendruckfedern auf Basis von Umlaufbiegeprüfungen. Dissertation; TU Ilmenau 2016
6) Reich, R.; Kletzin, U.: Vorhersage des Vorsetzbetrages von Schraubendruckfedern. Ilmenauer Federntag, TU Ilmenau 2017
7) Indian Standard 7906-1: Helical Compression Springs: Design and Calculation for Springs made from Circular Section Wire and Bar; BIS 1997
8) Japanese Industrial Standard JIS B 2704-1: Coil Springs: Basic Calculation methods on helical compression and extension springs
9) Aerospace Standard AS 24585C: Spring, Helical, Compression: For loads below 20 lbf; SAE International 2007
10) ASTM A125-96 (2013), Standard Specification for Steel Springs, Helical, Heat-Treated, ASTM International 2013
11) Society of Automotive Engineers SAE HS795 Spring Design Manual Part 2: Design and Application of Helical and Spiral Springs. SAE International 1990
12) Reich, R.; Kletzin, U.; Oechsner, M.; Spies, A.; Klein, M.: Rechnerischer Festigkeitsnachweis für Federn und Federelemente – Abschlussbericht zum Forschungsvorhaben IGF 18495, Ilmenau, 2017
13) FKM guideline: Rechnerischer Festigkeitsnachweis für Maschinenbauteile. 6th Volume, VDMA-Verlag 2012
14) FKM guideline: Rechnerischer Festigkeitsnachweis für Federn und Federelemente. VDMA-Verlag, ob e published in 2020
16) Dengel, D.: Die arcsin-√P-Transformation ‑ ein einfaches Ver-fahren zur grafischen und rechnerischen Auswertung geplanter Wöhler-versuche. Zeitschrift für Werkstofftechnik. 6th Volume, Journal 8; 1975
17) Spindel, J.E.; Haibach, E.: The method of maximum likelihood applied to the statistical analysis of fatigue data. International Journal of Fatigue, p. 81-88, 1979
18) Müller, Christian: Zur statistischen Auswertung experimenteller Wöhlerlinien. Dissertation; TU Clausthal 2015
19) FKM e.V.: VHCF variable Amplitude II; Bauteilauslegung unter Berücksichtigung von Beanspruchung mit variablen Amplituden und sehr hohen Schwingspielzahlen. Final report of FKM 309; Journal 331; VDMA-Verlag 2018
20) DIN EN 10270 Teil 1-3: Stahldraht für Federn. 2001-12
21) Reich, R.; Kletzin, U.: Rechnerischer Festigkeits-nachweis für Federn und Federelemente. 5th Ilmenauer Federntag 2019

FE Simulation of Power Springs

Thomas RAUSCH, Georg HANNIG
SCHERDEL siment GmbH, Scherdelstraße 2, 95615 Marktredwitz, Germany
TEL: +49 9231 603-591 e-mail: thomas.rausch@scherdel.de

The development process of the machine element spring increasingly requires a digital transformation. This is due to the growing complexity of future systems and greatly shortened development times.

In practice, the analytical calculation of power springs often delivers only unsatisfactory results. The reason for this is the strong dependence on the manufacturing process that can be observed as well as pronounced nonlinearities, e.g. due to winding contact. This leads to a large number of prototype loops with correspondingly high development costs.

This paper will present a methodology for the numerical calculation of power springs to get finally a characteristic line and the load stresses for fatigue assessment. Due to the prestressed installation situation, it is necessary to calculate the winding process with subsequent assembly into housing. The plastic deformation with following springback leads to the superposition of residual and load stresses. This significantly influences the spring characteristics.

The virtual spring must successfully meet all requirements in order to be produced in real life. This agile and, from the author's point of view, forward-looking development process makes it possible to face the challenges mentioned at the beginning and allows detailed insight into variables that were previously difficult to observe.

Keywords: power spring, process simulation, load simulation

1. INTRODUCTION

The development process of the machine element spring increasingly requires a digital transformation. This is due to the growing complexity of future systems and greatly shortened development times. It is therefore necessary to develop new calculation methods to predict important spring characteristics.

Power springs - as spring elements with a high energy capacity - present a special challenge. This is due to their manufacturing process and function, which will be presented in more detail at first.

The material of power springs are mostly textured or stainless strips with high UTS, usually > 1800 MPa.

A preconditioned spring strip (step 1 in Fig. 1) is first coiled around a mandrel (step 2). Plastic deformation can be observed. This depends on the properties of the strip as well as on process parameters. In order to increase the energy capacity, it is also possible to wind a strip into a spiral and coil it against its spiral shape (cross curved springs).

The coiled strip is now released in a sleeve (step 3). Depending on the geometry of the coiling mandrel, the sleeve diameter and the above mentioned dependencies, some coils are pressed against the inside of the sleeve by

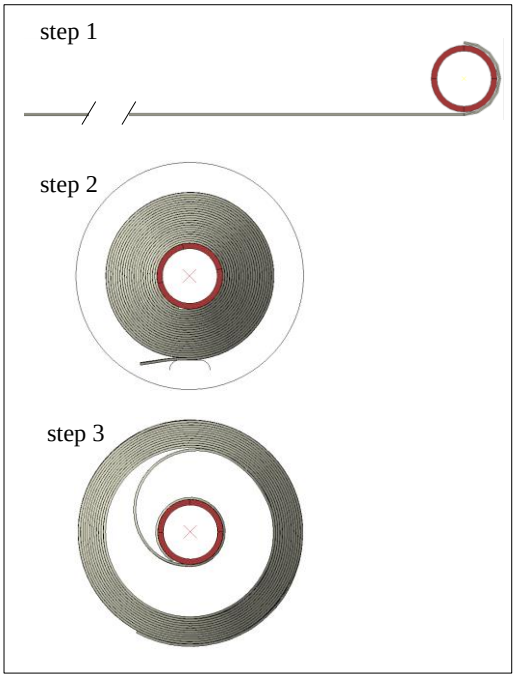

Fig. 1. Manufacturing steps in the simplest case. Step1: preconditioned strip, step 2: coiled on mandrel, step 3: spring back in housing

the pretension of the strip. The reason for this is the limited free elastic springback. The outer diameter of the free spring strip is therefore larger than the inner diameter of the sleeve. Coils close to the coiling mandrel

usually remain free due to the higher plastic deformation. This process step is often followed by a heat treatment for the specific improvement of spring properties such as fatigue life or setting behavior. The general effects can be read in Meissner et al.[1)].

The manufacturing of the power spring is now completed and the characteristic curve can be determined by relative rotation between inner mandrel and sleeve (Fig.). The curve can be divided into several sections. First there is a steep increase in torque. This can be observed by coiling the inner free coils until the first applied coil is lifted. This is followed by an increase with a lower and approximately constant spring rate. A hysteresis can be seen when the spring is released. This phenomenon can be explained by the friction between the coils.

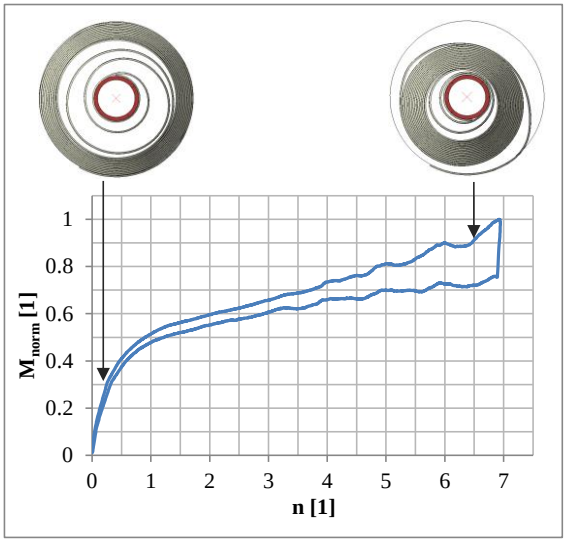

Fig. 2. Characteristic line of power spring, M_{norm} = normalized torque, n = number of rotation

As already shown by the characteristic curve and the described change in contact situations, the power spring has a distinct non-linear behavior. This makes an analytical design difficult. Meissner et al.[1)] or Bach[2)] suggest analytical formulas which are used in practice. As known from the corresponding literature and from practice, this is a good approach for a rough design.

One of the weak points is the prediction of the number of coils n_0 in free state. This state only becomes apparent when a spring is released outside the sleeve. n_0 strongly depends on the springback and thus on material and process. There is a lot of experience in spring design necessary. In most cases this is followed by trial and error in the prototype production.

In a more recent publication by Richter et al.[3)] the subject of springback and some influencing factors on austenitic spring strips (1.4310) are analyzed in more detail. The high strengths show a pronounced springback behavior, which is also dependent from the process. Thus the accuracy of the analytical approach is limited. For this reason the finite element method with correspondingly more complex material models should be the subject of research in future projects.

Yu et al.[4)] states that the spring behavior of power springs is influenced by a change in moment of inertia during the working cycle and shows an analytical methodology or extension to improve the predictions. By Tang et al.[5)] an investigation for the calculation of natural frequencies is presented. Thereby the natural frequencies of a modeled non prestressed spring are calculated by the linear methodology of an FE modal analysis.

The application of FE methods in the field of power springs is described in a publication by Shimoseki et al.[6)] from 2003 as "very hard to solve by FEM"[6)] caused by the strong non-linearity. Due to the significant development of commercial FE programs, the increase in computing power and the implementation of powerful material models, this article shows which possibilities currently exists. The focus of the study is solving the challenges mentioned above in sense of accelerate and digitize the spring design process.

2. METHOD OF CALCULATION

The finite element method offers the possibility to solve larger complex problems in the field of continuum mechanics. This is done by dividing the initially non-calculable problem area into smaller and therefore easier to calculate areas. This process is called discretization. In the case of the power spring the following challenges can be summarized:

- large deformation and rotation
- frictional contact and continuous modification of the associated contact surfaces
- interaction of several components
- metal plasticity
- consideration of the manufacturing process necessary
- transient (dynamic) influences

2.1 SIMULATION MODEL

The FE model shown in this paper is set up in the commercial software Abaqus. Therefore some model abstraction is required. In the simplest case, the surrounding components are designed as rigid bodies with assignment of mass and moment of inertia at the

center of gravity. The meshing of the components, see also Fig. 3, must be implemented with appropriate fineness to ensure sufficient contact of the coils.

Further tools such as coiling mandrel, guides, hold-down devices and, if necessary, also winding tools are essential for the manufacturing process. Rigid bodies are also useful for this purpose. Due to the diversity within the manufacturing processes up to the state shown in Fig. 3, reference should be made to Meissner et al.[1)]. In this literature the basic principles of virtual spring production are shown. The simplest procedure for power spring is described in the following chapter.

Coiling and application mandrel can have different dimensions. The connection to other components can be realized by a fixed connection, as in real life, for example by screwing or bonding. In the FE-model tie-constraints are helpful (Fig. 3-1). Interlocking connections like hooks can be abstracted by frictional contacts. (Fig. 3-2).

2.2 SIMULATION STEPS

The aim of the simulation should be representing the real process as far as possible in a way that the essential influences and target variables are correctly predicted.

Starting with the plane strip, it must be decided in front of the coiling process, if a virtual deformation is necessary. Otherwise it is possible to model in CAD the preconditioned strip. On the basis of previous experience, it is possible to eliminate the need for pre-forming in the case of variants which are coiled from a straight spring strip and only the connections to other components are bent (classical hook). For cross-curved variants, the pre-forming can influences the results significantly. This is due to geometry as well as material hardening and thus to residual stresses that are present over large areas of the strip.

The spring strip (straight or preformed) is now wound onto a coiling mandrel. Different process strategies can be modeled. In the simplest case, the strip is pressed onto the coiling mandrel via a hold-down device. This ensures gap-free coiling. The necessary forces and speeds are initially based on empirical values. In terms of process optimization, however, simulation is an effective tool for comparing different processes and process parameters.

The coiled strip is now spring-backed in the housing. Special attention must be given to perform this process close to reality. For example, the coiling mandrel is often turned back to a torque $M_{norm} = 0$ under torque control. This prevents a free spring-back. It must be ensured that no plastic deformation of the spring occurs during this process.

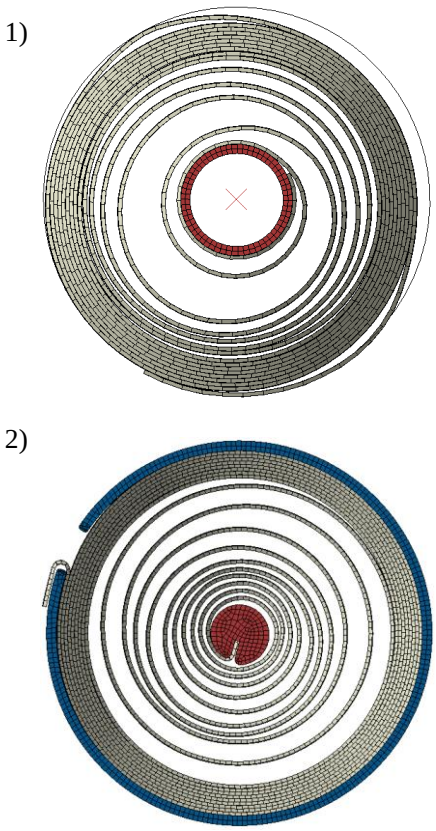

Fig. 3. FE-Models of mounted springs, 1) tie constraints, 2) contact constraints to surrounding parts

The now virtually manufactured spring is subjected to a torque test (characteristic curve recording). Often the coiling mandrel must be replaced by a test mandrel. The characteristic curve test should be simulated in real time scales in order to correctly detect inertia effects and contact phenomena such as stick-slip. However, compromises have to be made at this point due to greatly increasing calculation times. Insight is given in chapter 4. In order to make predictions about friction effects, it is recommended to observe the forward and backward curve.

2.3 MATERIAL MODEL

The continuous linking of variables from production and load simulation is elementary important. To select a suitable material model, the effects observed in macroscopic sample and component tests must be taken into account. The essential effects (no complete summary):

- especially with austenitic material grades: non-linearities in the load and unload module
- plastic deformation
- cyclic plasticity (Bauschinger effect[7)])
- anisotropic behavior due to rolling directions

- creep and ageing during heat treatment

For example, the observed effects show a strong influence on springback. It is not trivial to achieve an acceptable springback in FE-models with spring-hard material grades. Especially batch differences of the same material or special materials are challenging and require a lot of preliminary tests and validation.

For the specific power springs in this article, a multilinear kinematic hardening approach according to Chaboche[8,9] is recommended. This becomes understandable for cross-curved springs. Here, under certain circumstances, multiple plasticity occurs due to differently oriented load directions during pre-forming with subsequent coiling on a mandrel. An isotropic hardening approach would lead to a steadily increasing yield surface. This is not observed in different sample tests (cyclic tensile tests, bending tests).

In the case of heat treatment, it is possible to describe stress reduction by defining temperature-dependent yield limits and creep models. These changes influence the spring geometry and the load in the system. In Betten[10] useful models are presented.

3. RESULT

One of the important requirements of power springs is the energy store behavior and thus the spring characteristics. Fig. 4 shows a comparison between calculated and measured torque-angle characteristics. The spring is manufactured from a straight strip of 1.4310. The measured characteristic curve is recorded on a spring-torque testing machine.

First of all, one can see a very good match in both the forward and backward curve. The initial steep increase hits very well. This shows that the geometry and the preload after the springback in the sleeve are real. The hysteresis indicates that both the contact situation and the coefficient of friction correlate to reality. In simulation and weaker in the measurement, a wavy characteristic curve with a particular characteristic from half up to the usable coils is shown. In this state a lot of coils are lifted from the housing. After closer analysis, it becomes apparent that the spring deformation is not completely concentric around the mandrel, see also Fig. 2, top right. This leads to two phenomena. On the one hand, a cyclically changing diameter can be seen where the outer coil is connected to the housing. Thus, in this working range, the point of application of force and hence the moment on the mandrel also varies continuously. On the other hand, the moment of inertia of the entire system in relation to the axis of rotation changes continuously, resulting in dynamic effects especially at high rotational speeds.

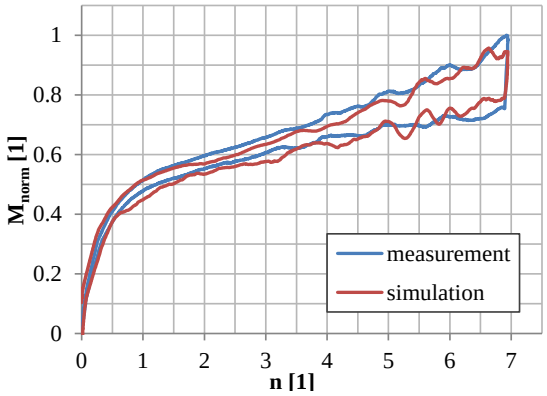

Fig. 4. Comparison of measured and simulated characteristic line

The hysteresis from Fig. 4 shows that the friction situation could be represented well. The simulation allows to examine tribological parameters isolated. For this reason, Fig. 5 shows a variation of the friction coefficient as an example. As expected, the hysteresis increases significantly. The basic characteristic remains identical although the waviness increases, especially in the reverse direction.

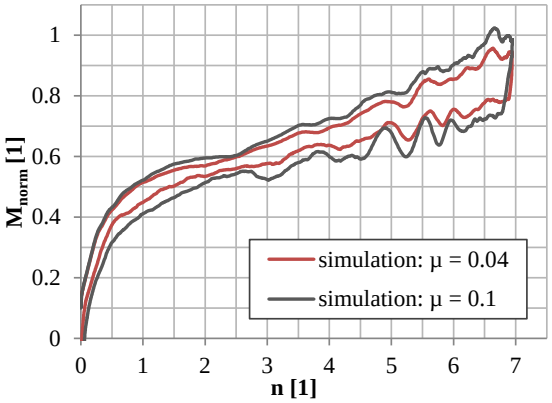

Fig. 5. Influence of friction coefficient

In the next step Fig. 6 a change of the coiling procedure is performed. There are different strategies for the production of power springs. In this case, the manufacturing process, especially the coiling mandrel and hold-down device, is changed in the simulation. With the existing models this is possible with a limited effort. The goal of reducing hysteresis has been reached. However, the spring torque and the number of rotations with constant spring rate decreases. Further optimization loops would be imaginable.

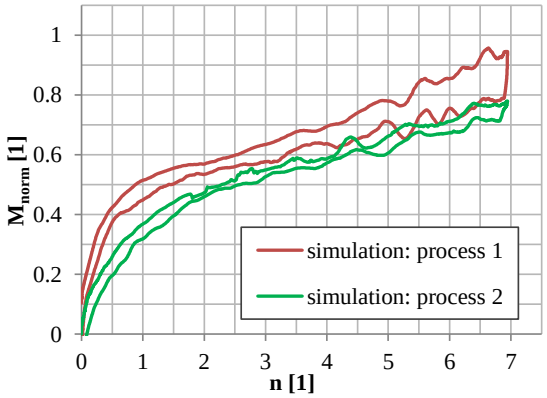

Fig. 6. Influence of different manufacturing process, aim: reduction of hysteresis

In order to make an estimation of the durability, the evaluation of stresses is necessary. It should be emphasized that there is a tensorial superposition of residual stresses from the manufacturing process (σ_{res}) and load stresses (σ_{load}).

$$\boldsymbol{\sigma_{total} = \sigma_{res} + \sigma_{load}} \qquad (1)$$

So it is not possible to compare the stresses with analytical calculation results. Fig. 7 shows the superimposed max. pressure- / tensile stresses of the tensor (σ_{total}) on the highly stressed outer path in different states.

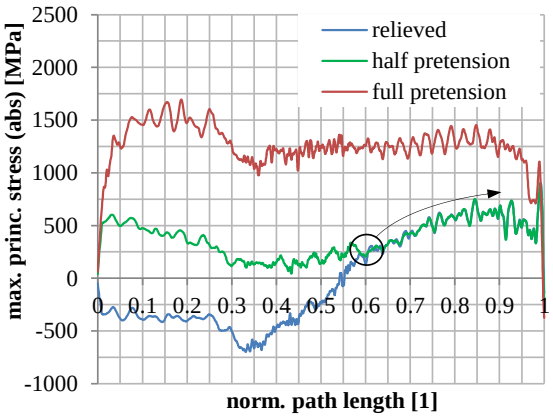

Fig. 7. Max. pressure- / tensile stresses of σ_total on outer path of spring in different positions, norm. path length 0 = inner end of spring (mandrel)

The released spring in the assembled state (blue) shows compressive stresses in the area of the mandrel up to approximately the middle strip length. This coils are free in the system. So there are pure residual compressive stresses from the forming process. With increasing path length, the coils contact other coils or the housing. The residual compressive stresses are superimposed by load stresses. In the state of half pretension (green) it is clearly visible that the inner coils in particular have gained a lot of tensile load stress. The black circle marks the point from which the coils are still in contact with the other coils and housing. With increasing preload, this point moves to the normalized path length = 1 (see arrow). In the fully tensioned state (red) there are even higher tensile stresses present in the area of the inner coils than at the outer.

Due to the described superposition of load and residual stresses, it is clear that the described characteristics in the stress curve need not be equally for each spring. An example is shown in Fig. 8.

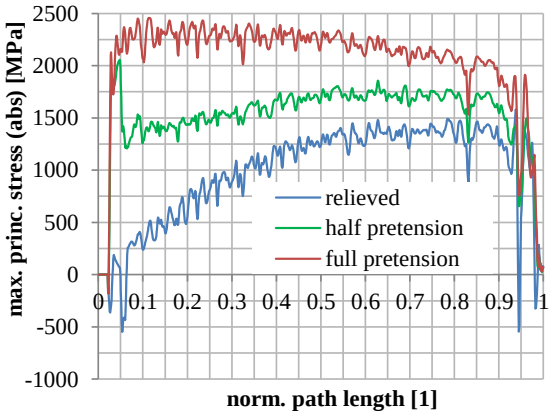

Fig. 8. Change in spring design, material and manufacturing process compared to Fig.7.

It is also noticeable that there is a strong oscillation in the stresses over the path length. The cause is finally analyzed in the manufacturing process. In the case of Fig. 8, a stepped coiling mandrel in the form of an archimedean spiral is not used. This results in an oscillating residual stress curve which is recurring over the length of the coils.

Even if a direct comparison with the analytic is not possible, the strong non-linearity and thus the problem with conventional calculation methods are evident. In this case, significantly larger stress amplitudes would occur in the area of the inner coil, which would lead to a reduction of the fatigue life.

4. SUMMARY

The following central points can be summarised on the basis of the analyses presented:

- The numerical simulation of power springs is possible with current simulation programs and computing power. Depending on the spring, the computing time is in the range of 24 - 86 h on 4 currently powerful CPU cores. A reduction of the computing time still seems possible.

- It is necessary to include the manufacturing process in different detail stages in simulation. So it is possible

to predict the pretensions load in the sleeve and the residual stresses to finally get a real characteristic.

- Material modelling in varying degrees of detail are necessary. A particular challenge is still the prediction of springback. Due to the huge strip length of power springs, this has a significant impact on the entire geometry and performance. Further research in field of material modelling of high strength steels would be desirable.

- The evaluation of stresses as superposition of residual stresses and load stresses can be applied for fatigue strength estimation and show differences to analytical stress calculation. Concepts for calculating local fatigue strength are conceivable with this input.

- In comparison to analytic approaches the system characteristics can be predicted more precisely in simulation. Trial and error is significantly reduced on real component and false estimations can be avoided.

REFERENCES

1) M. Meissner, H.-J. Schorcht and U.Kletzin, Metallfedern, Springer-Verlag, Berlin Heidelberg (2015), pp.120-125, 543-553.
2) W. Bach, Federfibel, SCHERDEL GmbH, Marktredwitz (2010), pp.89-108
3) K. Richter, F. Reuther, R. Müller and D. Landgrebe, Investigating the Influence of Bending Parameters on the Springback Behavior of Ultra-High Strength Spring Strips, Trans Tech Publications, Switzerland, Materials Science Forum, Vol. 918 (2018), pp.125-133
4) Yang Yu, Zengqiang Mi and Xudong Guo, Modeling and calculation of variable moment of inertia for spiral power spring, Advances in Mechanical Engineering, Vol.7 (2015), pp.1-15
5) Jingqiu Tang, Zhangqi Wang, Zengqiang Mi and Yang Yu, Finite Element Analysis of Flat Spiral Spring on Mechanical Elastic Energy Storage Technology, Research Journal of Applied Sciences, Engineering and Technology 7(5) (2014): pp.993-1000
6) M. Shimoseki, T. Hamano and T. Imaizumi, FEM for Springs, Springer-Verlag, Berlin Heidelberg New York (2003), pp.63-67
7) J. Bauschinger, Über die Veränderung der Elastizitätsgrenze und die Festigkeit des Eisens und Stahls durch Strecken und Quetschen, durch Erwärmen und Abkühlen und durch oftmals wiederholte Beanspruchungen, Mitteilungen aus dem mechanisch-technischen Laboratoriums der K. technischen Hochschule in München, Vol.13, München (1886)
8) J.-L. Chaboche: Sur l'utilisation des variables d'état interne pour la description de la viscoplasticité cyclique avec endommagement, Problèmes Non Linéaires de Mécanique, Symposium Franco-Polonais de Rhéologie et Mécanique (1977), pp.137-159
9) P.J. Armstrong, C.O. Frederick, A mathematical representation of the multiaxial Bauschinger effect, CEGB internal research report in Materials at High Temperatures Vol. 24, No. 1, Derbyshire (1966), pp.1-26
10) J. Betten, Creep Mechanics, 3rd edition, Springer-Verlag, Berlin Heidelberg (2008), pp.49-62

Stress Intensity Factors at Surface Cracks in Compression and Tension Springs

Yuji NAKASONE
Tokyo University of Science, 6-3-1, Niijuku, Katsushika-ku, Tokyo 125-8585, Japan 180
E-mail: nakasone731@yahoo.co.jp

This study has made 3D FE analyses in order to investigate the effects of crack inclination angle θ and aspect ratio a/c on the correction factors F_i (i=I, II, and III) for the stress intensity factors of semi-elliptic surface cracks in compression and tension coil springs where a is crack depth and c half crack surface length. The maximum first principal stress σ_{1max} with its direction of about 138° to the equator of the wire was produced on the outside wire surfaces of compression coil springs whereas on the inside wire surfaces of tension coil springs. The effects of q are significant for F_I and F_{II} values. The F_I values reach their maxima at almost all the values of eccentric angle ϕ of the cracks for θ =52°, nearly perpendicular to the σ_{1max} direction. The largest value of F_I is 0.841 in compression coil springs whereas 0.951 in tension ones. The largest value of F_{II} is 1.16 for θ=90° at ϕ=180° and the smallest one is -1.11 for θ =0° at ϕ=0° on the outside wire surfaces of compression springs whereas 0.688 for θ=0° and -0.814 for θ=90°, respectively, at ϕ=180° on the inside wire surfaces of tension springs. The effects of a/c are prominent for F_I values. The largest value of F_I is 0.673 for a/c=0.25 at ϕ=90°on the inside wire surfaces of compression springs. On the inside wire surface of tension springs, the largest value is 1.28 for a/c=0.25 at ϕ=90°.

Keywords: Tension, Compression, Coil Springs, Surface Cracks, Stress Intensity Factors, Mixed Mode, Finite Element Method

1. INTRODUCTION

Since coil springs are often made of high-strength materials, even very small incipient cracks can cause catastrophic fracture of springs. Actually, very small cracks are often found in coils springs fractured in service[1), 2)]. In order to ensure the reliability of springs, it is important to know the severity of cracks, i.e., the stress intensity factors of surface cracks initiated in coil springs. It is usual practice, however, to estimate the value of stress intensity factor of the opening mode from a simplified calculation of the stress intensity factor for a semi-elliptic surface crack in a circular cylindrical bar subjected to torsion.

The present author and his colleagues have made three-dimensional finite element (FE) analyses of coil springs not only of isotropic[3), 4)] but also generally anisotropic [5), 6), 7)] materials.

The present paper describes the stress intensity factors of semi-elliptic cracks on the surface of coil spring wires subjected to compression and tension loads. This paper also discusses the effects of spring parameters such as the inclination angle θ of a crack surface with the equator of wire and the aspect ratio a/c, or the ration of crack depth a to half crack surface length c.

2.FE CALCULATION OF STRESS INTENSITY FACTORS - MODEL AND CALCULATION

2.1 FE model of coil springs

Semi-elliptic surface cracks in coil springs were created and the stress intensity factors at the cracks were calculated by a commercial FEM software, ANSYS 17.0.[8)]

Fig. 1 (a) and (b) show an enlarged view of semi-elliptic surface crack model embedded in the present coil spring model and a whole view of the coil spring model, respectively. One hundred and eighty key points were created at equal distances on a spiral line having a radius of R=12 mm, a pitch of p=18 mm (equivalent to a pitch angle of 13.4°) and a winding number of n=5. A solid circle having a radius of r was created round each key point and was extrude from one key point to another along the spiral line to produce a circular cylinder having a length of $\pi R/18$. The $36n$ cylinders were then glued to one another to form a coil spring having a coil radius of R=12 mm, a pith of p=18 mm and a winding number of n=5. The hooks at the both ends of the spring were created as shown in Figs. 2 (a) and (b): i.e., at the end of the spring coil denoted by “A” in Figs. 2 (a) and (b), shorter circular cylinders were joined together towards the center of the coil to form a circular arc having a radius of $R/3$=4 mm and, at the place denoted

by "B" in the figures, cylinders were joined together to form a partial circle having a radius of about 0.8*R*=9.6 mm and connected to the group of cylinders forming the straight-line wire arranged along the center axis of the coil spring.

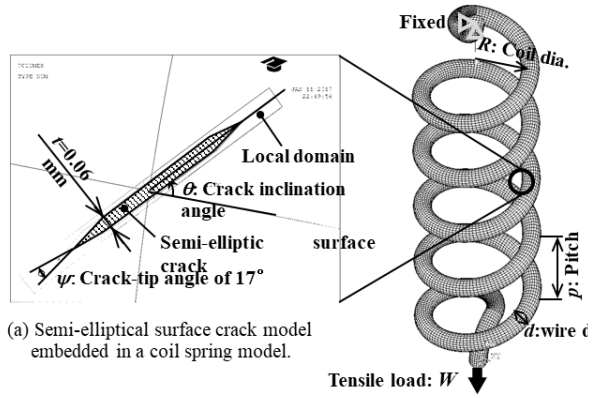

(a) Semi-elliptical surface crack model embedded in a coil spring model.

(b) A whole view of the present tension coil spring model.

Fig. 1. A whole view of the present coil spring model and a semi-elliptical surface crack model embedded in the spring model.

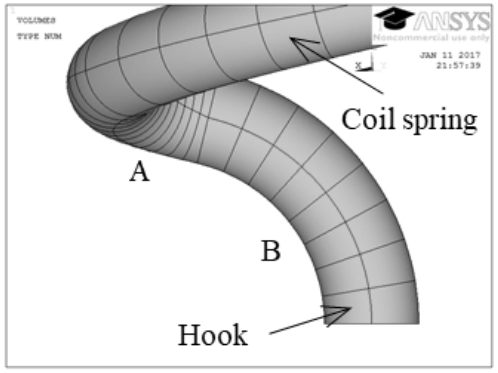

(a) Detailed view of a rising portion of the lower hook.

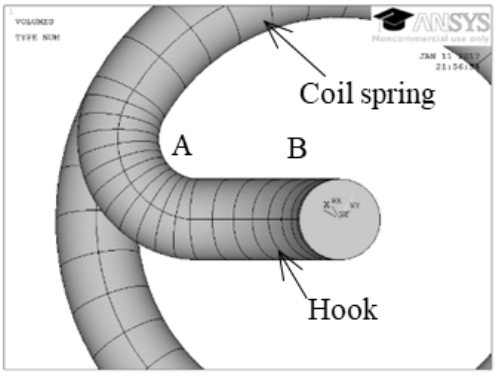

(b) Bottom view of the lower hook.

Fig. 2. 3D FEM model of the lower hook portion.

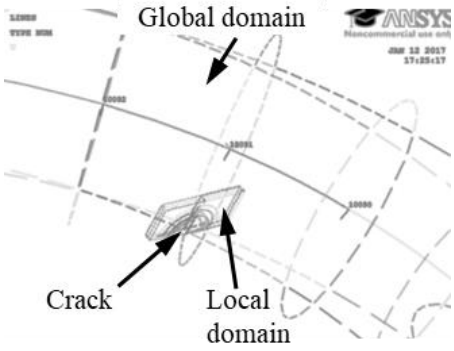

Fig. 3. A local domain containing a semi-elliptical surface crack embedded in a global domain of a coil spring

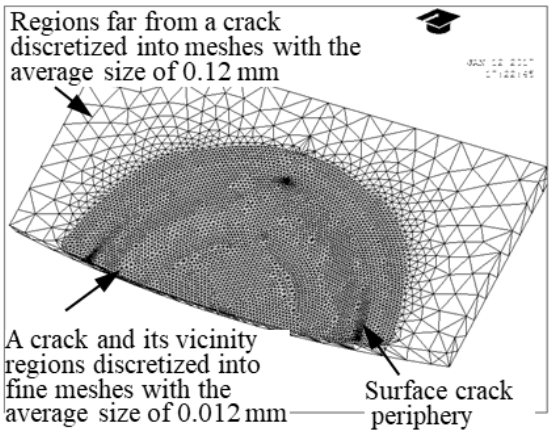

Fig. 4. Finite element discretization of an semi-elliptical surface crack including the local domain.

The body of the coil spring model except at the vicinity of the crack region, or so-called the subdomain, was discretized with the quadratic hexahedral elements of an average size of 0.5 mm. The boundary conditions are summarized as shown in Fig. 1 (b): i.e., the upper end surface of the hook was fixed in all directions and the lower end surface was uniformly loaded by compressive or tensile load of W=±100 N.

2.2 FE model of semi-elliptic surface cracks

Stress field around surface cracks cannot be properly computed by FEM due to contact between the mating surfaces of non-opening cracks.[9] The present study adopted a thin slit of 0.06 mm in width with sharp tips of an opening angle of ψ=17° instead of a crack. The stress intensity factor (SIF) values calculated by using the pseud-cracks agree well with most reliable solutions within -7.4 % relative error at the mode III SIF, K_{III}, of an annular crack in a circular cylinder subjected to tortion[10] and within 1.7 % relative error at the mode I SIF, K_I, of a central through-thickness crack in a flat plate subjected to uniform tensile stress.[9), 11]

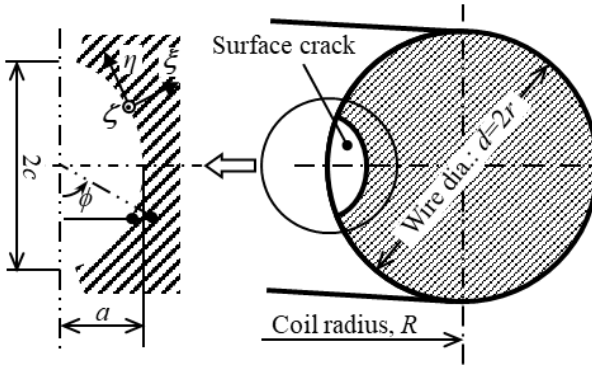

Fig. 5. Eccentric angle ϕ and local Cartesian coordinates (ξ, η, ζ) set on the periphery of a semi-elliptical surface crack on the inside surface of a tension coil spring.

This study adopted the subdomain in which a semi-elliptic surface crack model was embedded as shown in Fig. 3. The subdomain enables the efficient FE discretization at surface cracks of different shapes. It is only the subdomain that should be discretized at a new surface crack. The discretization of the main body of the coil spring model except at the subdomain need not be updated. Fig. 4 shows an example of FE discretization of the subdomain in which a surface crack is embedded. The crack and its vicinity regions were discretized with fine quadratic tetrahedral elements of an average size of 0.012 mm whereas regions away from the crack with quadratic hexahedral elements of an average size of 0.12 mm.

2.3 Calculation of correction factors at stress intensity

Fig. 5 illustrates an elliptic surface crack on the inner surface of the spring wire. A local Cartesian coordinate system (ξ, η, ζ) was set along the periphery of the crack as shown in Fig. 5. Since mixed mode stress state develops in the vicinity of the crack periphery, SIF's of the three modes need to be determined. The values of SIF's were calculated by the stress extrapolation method[8] by using the following relations:

$$\begin{cases} K_{\mathrm{I}} = \lim_{\xi\to 0} \sigma_{\zeta\zeta}\sqrt{2\pi\xi} \\ K_{\mathrm{II}} = \lim_{\xi\to 0} \tau_{\xi\eta}\sqrt{2\pi\xi} \\ K_{\mathrm{III}} = \lim_{\xi\to 0} \tau_{\eta\zeta}\sqrt{2\pi\xi} \end{cases} \quad (1)$$

where ξ is the distance from the crack tip, $\sigma_{\eta\eta}$ the normal stress in the η direction, $\tau_{\xi\eta}$ the in-plane shear stress and $\tau_{\eta\zeta}$ the out-of-plane stress on the wire cross section.

The values of SIF's, K_{I}, K_{II} and K_{III}, were evaluated at the eccentric angles of the semi-elliptic crack, ϕ=0°, 30°, 45°, 60°, 120°, 135°, 150° and 180°, and the values of the correction factors for the SIF's, or the normalized SIF's, F_i (i=I, II and III) were calculated by Eq. (2):

$$F_i = \begin{cases} \dfrac{K_i}{\sigma\sqrt{\pi a}} & (i = \mathrm{I}) \\ \dfrac{K_i}{\tau\sqrt{\pi a}} & (i = \mathrm{II},\ \mathrm{III}) \end{cases} \quad (2)$$

where a is the depth of the semi-elliptic crack, τ the Wahl shear stress given by the following formula:

$$\tau = \kappa\frac{2WR}{\pi r^3} = \left(\frac{4s-1}{4s-4} + \frac{0.615}{s}\right)\frac{2WR}{\pi r^3} \quad (3)$$

where κ is the Wahl stress correction factor,[12] W the applied load, and s the spring index, i.e., s=R/r. The normal stress σ in Eq. (2) is the maximum first principal stress produced. The shear stress τ in Eq. (3) was set equal to the maximum first principal stress σ by deducting from Mohr's stress circle[13] and at the sake of ease of practical calculation.

2.4 Analytical conditions

In the present FE analyses, Young's modulus of the spring wire was set E=210 GPa, Poisson's ratio ν=0.3, the coil radius R=12 mm, the wire radius r=2 mm and the applied load W=±100 N where the plus load indicates tensile load and the minus compressive one. These conditions were common at all the FE analyses performed in the present study. The other two parameters, i.e., the inclination angle of a crack to the equator of the spring wire, θ, and the crack aspect ratio, or the ratio of crack depth to half the crack surface length, a/c, were systematically changed in order to investigate the effects of these parameters on the correction factors for the stress intensity factors of the three modes of the semi-elliptic surface cracks as follows:

Case 1; Investigation of the effects of crack inclination angle θ, and

Case 2; Investigation of the effects of aspect ratio a/c.

3. ANALYTICAL RESULTS

3.1 Principal and maximum shear stresses in uncracked coil springs

Fig. 6 and 7 show the first principal stress, s1, vs. distance from wire center, x, relationships in compression and tension coil springs, respectively. The pith, p/R, dependence is also depicted in the figures. The σ_1 takes its minimum on the inside wire surfaces in compression coil springs and increases linearly with the distance from the wire center, x, to reach its maximum

on the outside surfaces. In tension coil springs, however, the σ_1 vs. x relationships are reversed; i.e., the σ_1 takes its maximum on the inside and decreases linearly with the value of x to take its minimum on the outside surfaces. The values of σ_1 in compression coil springs is higher than those in tension ones. The σ_1 vs. x relationships rotate around the point at x=0, at which the equator of the wire is located, in the two types of springs. The effect of p/R is larger in compression than in tension coil springs.

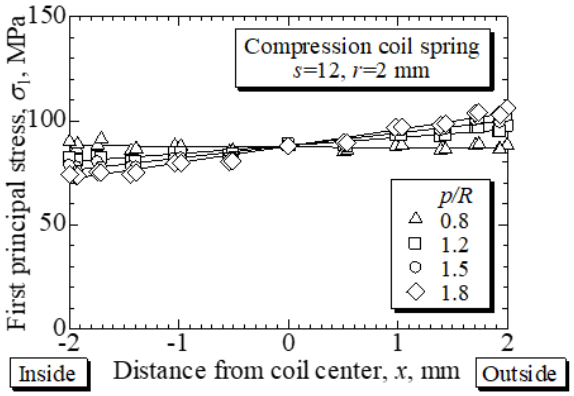

Fig. 6.Distributions of the 1st principal stress s1 on the wire surfaces of compression coil springs for different p/R values; p is the pitch and R coil radius of the springs.

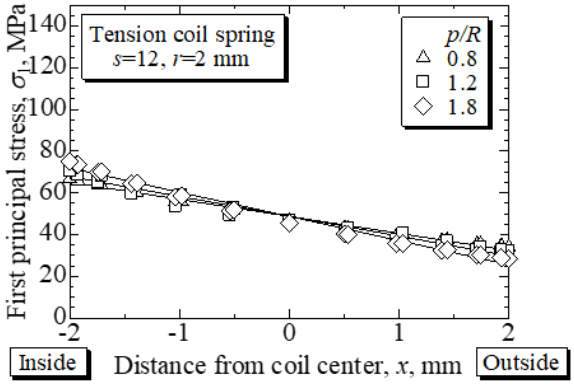

Fig. 7. Distributions of the 1st principal stress s_1 on the wire surfaces of tension coil springs for different p/R values; p is the pitch and R coil radius of the springs.

The direction of the maximum first principal stress is approximately 138° to the equator of the wire, the same for cracks on the outside wire surfaces of compression coil springs and those on the inside wire surfaces of tension coil springs.

3.2 Case 1: the effects of crack inclination angle θ on the correction factors for the stress intensity factors

The correction factors for the stress intensity factors were evaluated at semi-elliptic surface cracks on the inside surfaces of compression coil springs and on the outside wire surfaces of tension coil springs, where the first principal stress σ_1 was highest, at the middle of the length of the springs (n=2.5) for crack half surface length c=0.5 mm and aspect ratio a/c=1.0. The crack inclination angle, θ, was changed from 0° to 90° to investigate the effects on the correction factors.

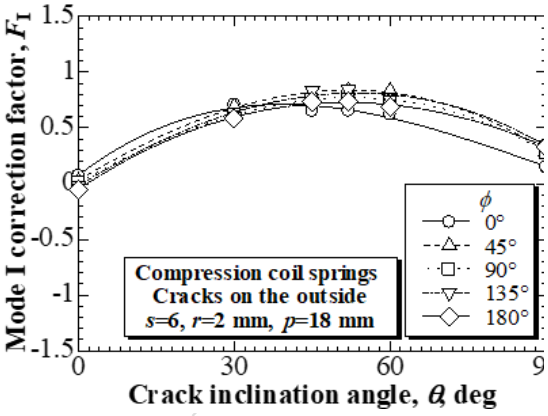

(a) Mode I correction factor

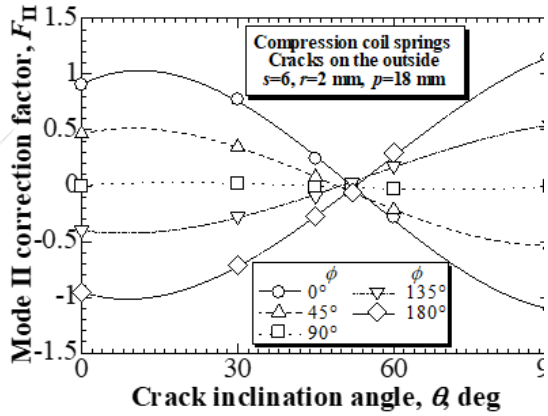

(b) Mode II correction factor

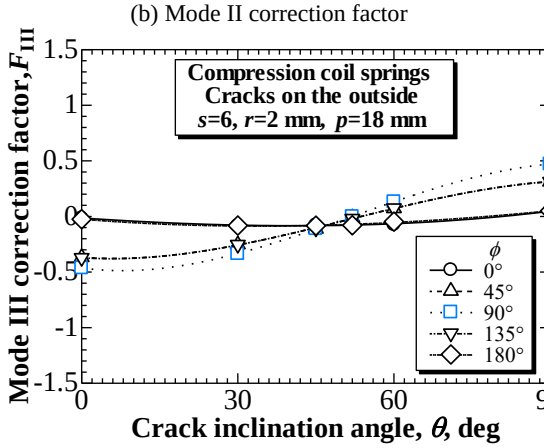

(b) Mode II correction factor

Fig. 8.Relationships between the correction factors and crack inclination angle θ for surface cracks on the outside wire surfaces of compression coil springs.

Fig. 8(a) to (c) show the relationships between each of the correction factors of the three modes and crack inclination angle θ for surface cracks on the outside wire surfaces of compression coil springs. The solid

lines in the figures represent the cubic curves of best fit for the F_I, F_{II} and F_{III} vs. θ relationships.[3), 4)]

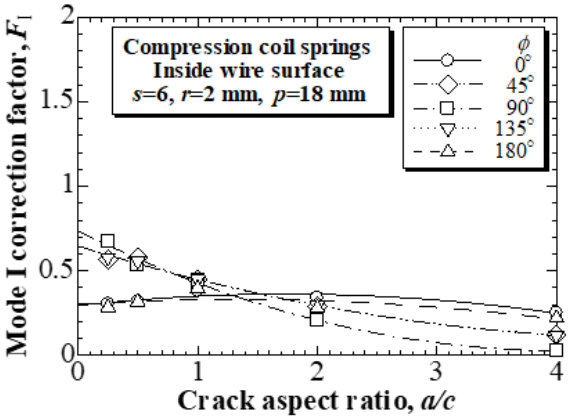

(a) Mode I correction factor

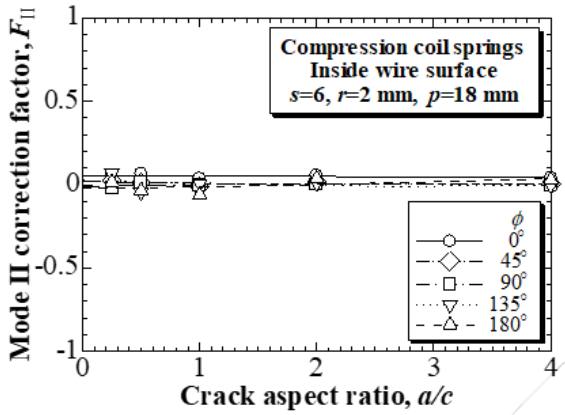

(b) Mode II correction factor

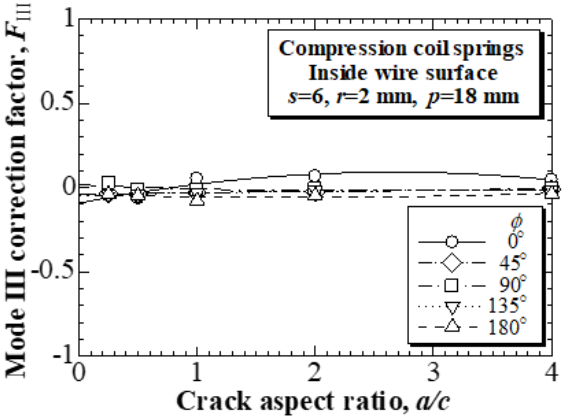

(b) Mode II correction factor

Fig. 10. Relationships between the correction factors and crack aspect ratio a/c for surface cracks on the inside wire surfaces of compression coil springs.

The mode I correction factor, F_I, vs. crack inclination angle, θ, relationships, as depicted in Fig. 8 (a), show almost the same tendency, namely, upward convex, at different values of eccentric angle ϕ, or at the different positions of the crack periphery. For θ=52°, that is nearly equal to the angle perpendicular to the direction of the maximum first principal stress, the F_I values reach their maxima of 0.781 to 0.841 at all the values of ϕ except at ϕ=0°. The F_I values are nearly zero for θ=0° and 0.151 to 0.346 for θ=90°.

Fig. 8 (b) shows the F_{II} vs. θ relationships along the crack periphery. At ϕ=0° near surface, the F_{II} value takes its maximum of 0.906 for θ=0° and decreases almost monotonically with θ to its minimum of −1.11 for θ=90°. At ϕ=180°, the opposite crack tip to that at ϕ=0° near surface, the F_{II} vs, θ curve is completely reversed; i.e., the curve takes its minimum of −0.954 for θ=0° and increases almost monotonically with θ to its maximum of 1.16 for θ=90°. The other curves are placed between the two. The F_{II} values are almost zero for all the values of θ at ϕ=90°.

Fig. 8 (c) shows the F_{III} vs. θ relationships along the crack periphery. Unlike the F_{II} vs. θ relationships in Fig. 8 (b), the F_{III} values at ϕ=0° and 180° are almost zero for all the values of θ. The curves at ϕ=45° to 135° take their minima of about −0.5 and increase monotonically with θ and reach their maxima of 0.313 to 0.472 for θ=90°.

Fig. 9 (a) to (c) show the relationships between each of the correction factors of the three modes and crack inclination angle θ for surface cracks on the inside wire surfaces of tension coil springs. The solid lines in the figures represent the cubic curves of best fit for the F_I, F_{II} and F_{III} vs. θ relationships.[3), 4)] Fig. 9 (a) and (b) show that the F_I and F_{II} vs. θ relationships of semi-elliptic surface cracks on the inside wire surfaces of tension coil springs are highly similar not only in shape but also in value to those on the outside wire surfaces of compression coil springs as shown in Figs. 8 (a) and (b).

The maxima of F_I values are 0.651 to 0.951, slightly different from those for the compression coil springs as depicted in Fig. 8 (a). The F_I values are nearly zero for θ=0° and 0.199 to 0.463 for θ=90°. The F_{II} value takes its minimum of -0.691 for θ=0° and increases almost monotonically with θ to reach its maximum of 0.554 for θ=90° at ϕ=0°, about half the maximum value of F_{II} in compression coil springs.

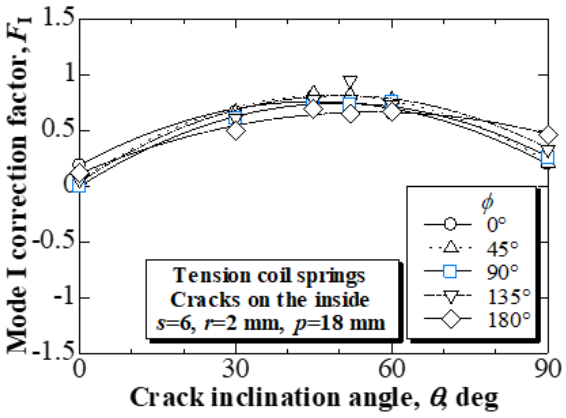

(a) Mode I correction factor

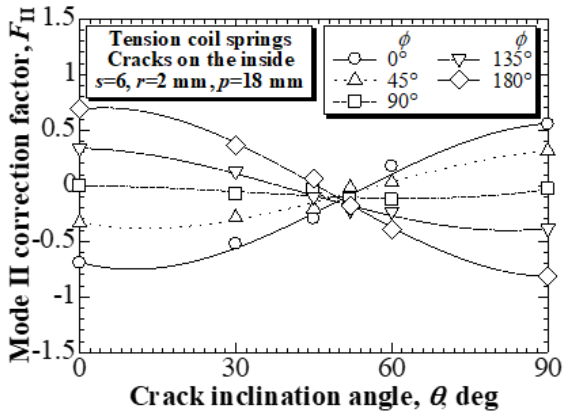

(b) Mode II correction factor

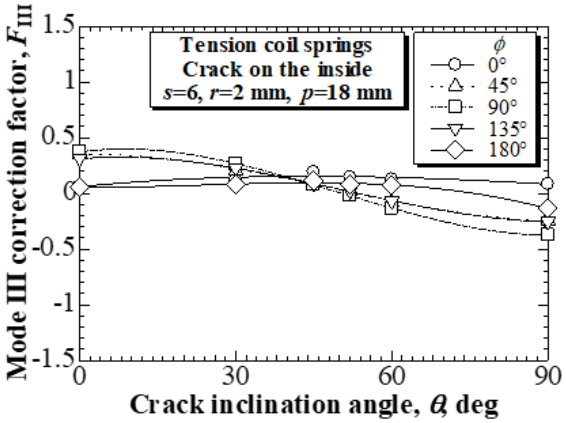

(b) Mode II correction factor

Fig. 9. Relationships between the correction factors and crack inclination angle q for surface cracks on the inside wire surfaces of tension coil springs.

The F_{III} vs. θ curves for the tension coil springs at ϕ=45° to 135° in Fig. 9 (c) are reversed compared to those for compression coil springs as depicted in Fig. 8 (c); i.e., the curves take their maxima of 0.311 to 0.372 and decrease monotonically with θ and reach their minima of –0.375 to –0.245. The F_{III} values near the wire surface (ϕ=0° and 180°) are nearly zero for all the values of θ.

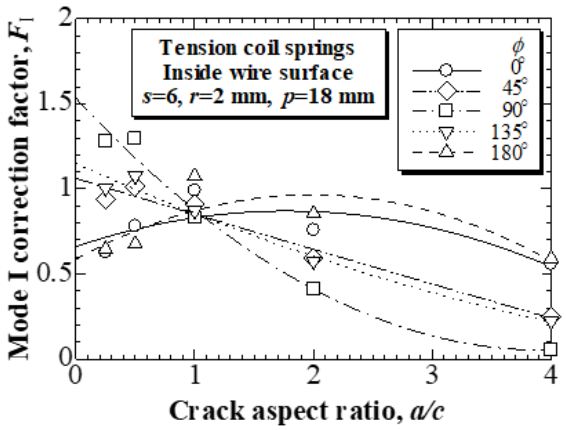

(a) Mode I correction factor

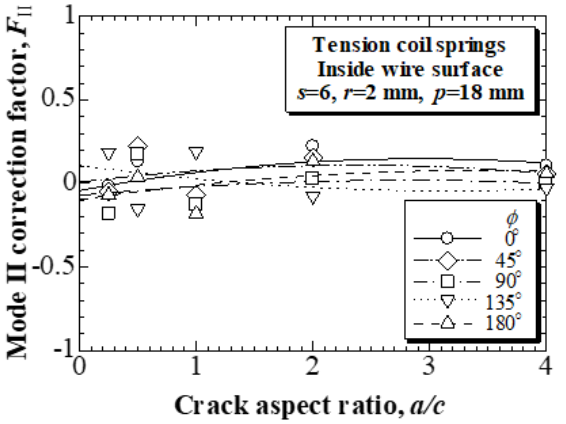

(b) Mode II correction factor

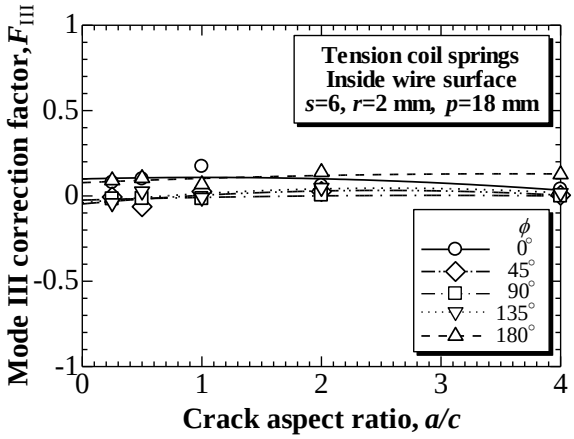

(b) Mode III correction factor

Fig. 11. Relationships between the correction factors and crack aspect ratio a/c for surface cracks on the inside wire surfaces of tension coil springs.

3.3 Case 2: the effects of crack aspect ratio a/c on the correction factors for the stress intensity factors

The correction factors at the stress intensity factors were evaluated at semi-elliptic surface cracks on the

inside wire surfaces of compression and tension coil springs at the middle of the length of the springs (n=2.5) for crack half surface length c=0.5 mm and the aspect ratio, a/c was changed from 0.25 to 4.0 to investigate the effects on the correction factors.

Fig.10 (a) to (c) show the relationships between each of the correction factors of the three modes and crack aspect ratio a/c for surface cracks on the inside wire surfaces of compression coil springs. The solid lines in the figures represent the quadratic curves of best fit for the F_{I}, F_{II} and F_{III} vs. a/c relationships.[3), 4)]

Fig. 10 (a) shows that the F_{I} value takes its maximum of 0.5 to 0.673 for a/c=0.25 to 135°, i.e., inside of cracks and monotonically decreases with the value of a/c to reach its minimum of 0.03 to 0.2 for a/c=4 at ϕ=45°. The F_{I} value becomes lower and takes almost constant values of 0.253 and 0.397 near wire surface at ϕ=0° and 180°, i.e., near wire surface.

Fig.10 (b) and (c) show that the F_{II} and F_{III} values are almost zero along the entire periphery of cracks for all the a/c values investigated in this study.

Fig. 11 (a) to (c) show the relationships between each of the correction factors of the three modes and crack aspect ratio a/c for surface cracks on the inside wire surfaces of tension coil springs. The solid lines in the figures represent the quadratic curves of best fit for the F_{I}, F_{II} and F_{III} vs. a/c relationships.[3), 4)]

Fig. 11 (a) shows that the F_{I} value takes its maximum of 1.28 for a/c=0.25 and monotonically decreases with the value of a/c to reach its minimum of 0.03 for a/c=4 at ϕ=90°. The F_{I} value takes its maximum of 0.567 and 0.579, and reaches its minimum of 0.123 and 0.118 for a/c=4 at ϕ=45° and 135°, respectively. At ϕ=0° and 180°, the F_{I} value takes its maximum of 0.759 and 0.855, respectively, for a/c=2.

The maximum F_{I} value is about twice larger than that for semi-elliptic surface cracks on the inside wire surfaces of compression coil springs as shown in Fig. 10 (a). This result implies that the correction factors affected by the crack position. Actually, the investigations regarding the effects of positions on the correction factors revealed that the values of F_{I}, F_{II} and F_{III} are about twice higher on the outside than on the inside wire surfaces in compression coil springs.[3), 14)] Multiplying the F_{I} values in Fig. 10 (a) by a factor of about two brings about F_{I} vs. a/c relations to be obtained on the outside wire surfaces of compression coil springs.

Fig.11 (b) and (c) show that the F_{II} and F_{III} values are almost zero along the entire periphery of cracks for all the a/c values investigated in this study. This result is also the same as that obtained from Figs. 10 (b) and (c).

4. CONCLUSION

This study has made 3D finite element analyses in order to investigate the effects of spring parameters on the correction factors F_i (i=I, II, and III) for the stress intensity factors of the three modes for semi-elliptic surface cracks in compression and tension coil springs. The parameters investigated are inclination angle of the crack to the equator of the wire θ and crack aspect ratio a/c where a is crack depth and c half crack surface length. The main results obtained in this study are as follows.

(1) The maximum first principal stress s1max was produced on the outside wire surfaces of compression coil springs whereas on the inside wire surfaces of tension coil springs. The direction of s1max is approximately 138° to the equator of the wire, the same for cracks on the outside wire surfaces of compression coil springs and those on the inside wire surfaces of tension coil springs.

(2) The effects of q are especially significant for FI and FII values. The FI values reach their maxima at almost all the values of eccentric angle f of the cracks for q=52°, practically perpendicular to the direction of s1max. The largest maximum value of FI is 0.841 in compression coil springs whereas 0.951 in tension ones.

(3) The largest maximum value of FII is 1.16 for q=90° at f=180° and the smallest minimum one is -1.11 for q=0° at f=0° on the outside wire surfaces of compression coil springs whereas 0.688 for q=0° and -0.814 for q=90°, respectively, at f=180° on the inside wire surfaces of tension coil springs.

(4) The effects of a/c are especially prominent for FI values. The largest maximum value of FI is 0.673 for a/c=0.25 at f=90°on the inside wire surfaces of compression coil springs. Taking the effects of crack position into account, the largest maximum value of FI is estimated to be doubled on the outside wire surfaces of compression coil springs. On the inside wire surface of tension coil springs, the maximum value of FI is 1.28 for a/c=0.25 at f=90°.

REFERENCES

1) N. Takenoshita, K. Shirabe and Y. Aoki, Trans. Jpn Soc. Spring Engs. **32**, 35 (1987) (in Japanese).
2) The Soc. of Mats. Sci., Jpn., *Fractography*, (Maruzen Pub. Co., Ltd., ISBN 4-621-04792-2, 2000), pp. 298-303 (in Japanese).
3) Y. Nakasone and K. Muranushi, Trans. Jpn Soc. Spring Engs. **62**, 37 (2017) (in Japanese).
4) Y. Nakasone, K. Muranushi and K. Kawakami, Trans. Jpn Soc. Spring Engs. **64**, 79 (2019) (in Japanese).
5) Y. Nakasone and K. Muranushi, Proc. 2017 Autumn Meeting Jpn Soc. Spring Engs., (2017) (in Japanese).
6) Y. Nakasone and K. Muranushi, Proc. 2018 Spring Meeting Jpn Soc. Spring Engs., (2018) (in Japanese).
7) Y. Nakasone and K. Muranushi, Proc. JSME CMD2018, OS0413(2018) (in Japanese).
8) T. Stolarski, Y. Nakasone and S. Yoshimoto, *Engineering Analysis with ANSYS Software*, *2nd Ed.*, (Butterworth-Heinemann ISBN 0-081-02164-X, 2018), 551 pp.
9) E.g., M. Isida, *Elastic Analysis of Cracks and Stress Intensity Factors*, (Baifukan Co., Ltd., ISBN 4-563-03230-1, 1976), (in Japanese).
10) J. P. Benthem and W. T. Koiter, in: G. C. Sih (Ed.) *Methods of Analysis and Solutions of Crack Problems*, (Springer ISBN 9-048-18246-8, 1973), pp. 131-178.
11) M. Isida, in: G. C. Sih (Ed.) *Methods of Analysis and Solutions of Crack Problems*, (Springer ISBN 9-048-18246-8, 1973), pp. 56-130.
12) A. M. Wahl, *Mechanical Springs*, *2nd Ed.*, (McGraw-Hill ISBN 0-070-67705-0, 1963), pp. 56-59.
13) E.g., E. P. Popov and T. A. Balan, *Engineering Mechanics of Solids*, *2nd Ed*., (Prentice Hall Inter. Inc. ISBN 0-13-081534-9, 1991), pp. 470-498.
14) Y. Nakasone and K. Kawakami, Unpublished data

A new test bench for rotating bending fatigue test of tempered steel wires

Federico BALLO, Michele CARBONI, Gianpiero MASTINU and Giorgio PREVIATI
Politecnico di Milano – Department of Mechanical Engineering, via La Masa 1, 20156, Milano
Email: federicomaria.ballo@polimi.it

Fatigue strength of mechanical components depends on a large number of factors such as surface finishing, manufacturing process, residual stresses etc. To account for such a large amount of variables, experimental tests on finished or semi-finished components are required for an accurate assessment of durability performances.

In this paper, a new bench for the rotating bending fatigue tests of tempered steel wires is presented. The bench is based on a four-point bending loading scheme and is employed for testing the spring wires just before the final winding.

Differently from conventional test benches, here the focus is on semi-finished components (more than 1 meter long), instead of standard specimens commonly used for material testing. Moreover, the bench presents a non-linear configuration of the tested component due to its length.

The bench design has provided some unreferenced features that make it quite accurate and effective in producing quick fatigue assessments. Some fatigue bending tests of tempered steel wires are described and discussed.

Keywords: Wire rotating bending, High cycle fatigue, Four-point bending

1. INTRODUCTION

Lightweight design is nowadays assuming a great importance in automotive industry and vehicle design. In fact, the reduction of the vehicle mass implies significant improvements in terms of reduction of fuel consumption and Greenhouse gas (GHG) emissions. Minimisation of the vehicle mass takes place from the minimisation of each single component.

Beside lightweight, safety is a main driver in vehicle design and construction. To guarantee the required safety standards, accurate numerical models and experimental tests are required for design and safety assessment of vehicle components.

Helical springs are employed in many applications and particularly in automotive systems. Such components are often subject to a very high number of fatigue cycles, even in the order of giga-cycles, as in the case of helical springs for internal combustion engines valves[1-2)].

Said that, it is clear that the persistent demand of lightweight and compact embodiments represents an important challenge for OEM manufacturers, who are forced to the development of spring steels with higher mechanical and fatigue properties. To meet such elevated design requirements, a high standard of the manufacturing process has to be maintained.

The assessment of fatigue life of material is one of the most discussed topic and a large number of papers can be found in the literature discussing the related methodologies. An example of such approaches related to spring steel characterization can be found in[3)]. This kind of approach, although very effective in the definition of the properties of the raw material, does not allow for the evaluation of the effective properties of the semi-finished component.

Referring to helical springs, the manufacturing process of such components is long and complex, since is characterised by several passages with important modifications of the material. Only the direct test of wire sections as provided by the manufacturing process can assess the quality of the component before the spring is actually realised.

In this paper, a new test bench for fatigue life assessment of semi-finished steel wires for spring manufacturing is presented.

2. DESIGN OF THE TEST BENCH

In Fig. 1 the 3D drawing of the bench is shown. In the bench, there are two movable central supports and two fixed extreme supports; by imposing a transversal displacement to the two central supports the wire is progressively deformed up to reach the prescribed stress

level. The motor is connected to the wire by a special elastic joint and it is free to move to accommodate the deformation of the wire without applying any force.

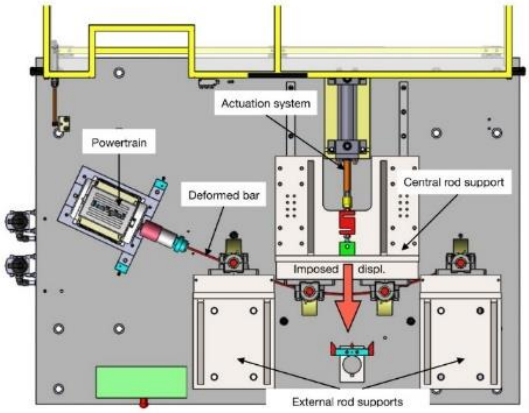

Fig 1. Drawing of the four point rotating bending test bench.

The supports of the wire are free to rotate with respect to a vertical axis as to accommodate the deformation of the wire. The two central supports are moved by a hydraulic actuator and are guided by high precision linear rails.

The curvature of the wire in its deformed configuration is measured by the specifically designed arcmeter shown in Fig. 2. The stress imposed in the central section of the wire is then calculated from the curvature measure.

The accuracy of the test bench is strongly dependent on the precision of the couplings of its parts and on the machining tolerances. In the design and manufacturing process of the test bench, a proper compromise between machining tolerances and manufacturing cost has to be found. To accomplish that, a sensitivity analysis based on a numerical model of the four point bending test was performed. From the analysis, it turned out that great care has to be paid in ensuring a precise alignment of the two central supports to maximise the accuracy of the bench.

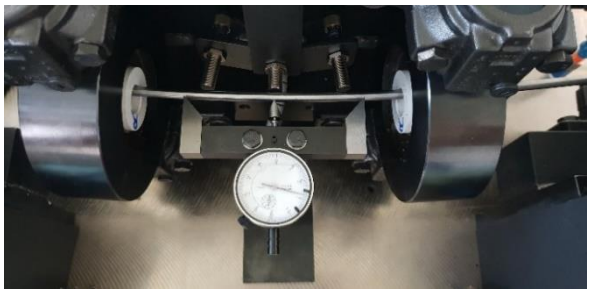

Fig. 2. Detail of the measurement of the wire curvature.

3. FINITE ELEMENT MODEL OF THE PLASTIC BUSHINGS

Since the wire, unlike the standard specimens used for conventional material fatigue tests, has a uniform diameter along its entire length, one of the major problems is that of defining the interface area between wire and supports. The contact between the wire and the machine supports is made by means of polymeric bushings based on Polyethylene Terephthalate (PET) with an additive of Polytetrafluoroethylene (PTFE). The bushings are installed on each of the four supports, two of them are visible in Fig. 2.

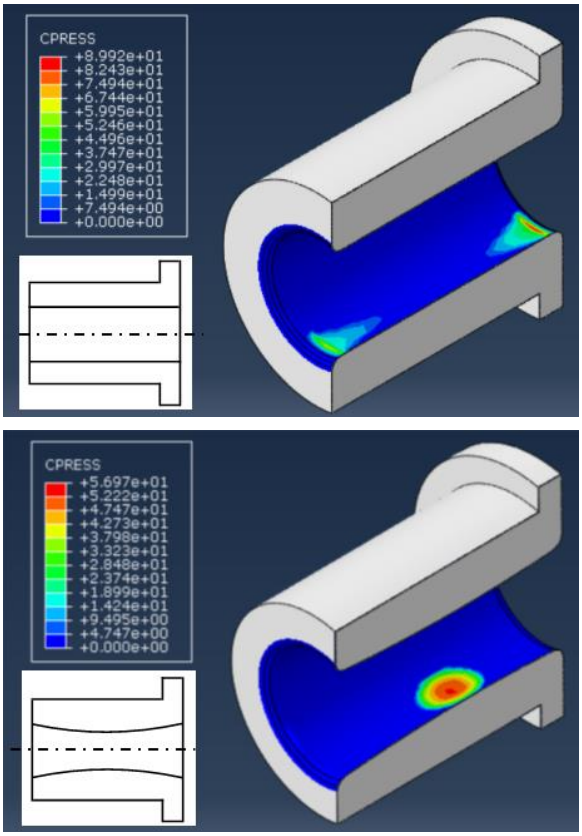

Fig. 3 Contact pressure on the PET bushing, wire diameter 20 mm. Top: cylindrical bushing. Bottom: bushing with internal curved profile.

For the definition of the internal profile of the bushings, accurate numerical analyses were performed with the finite element method, which allowed to define an ideal profile of the surface inside the bushing. The profile of this surface, in direct contact with the wire, has been defined in order to minimize the contact pressure with the wire surface and at the same time to maintain a uniform stress in the central section of the wire (the area between the two central supports) as shown in Fig. 3. The advantage of the curved profile is also evident from Fig. 4, that shows the stress behaviour near the central

support on two different wires obtained from simulations with curved profile and cylindrical bushings. The curved profile bushing allows to obtain a smoother transition and a more constant and uniform stress state in the central portion of the wire.

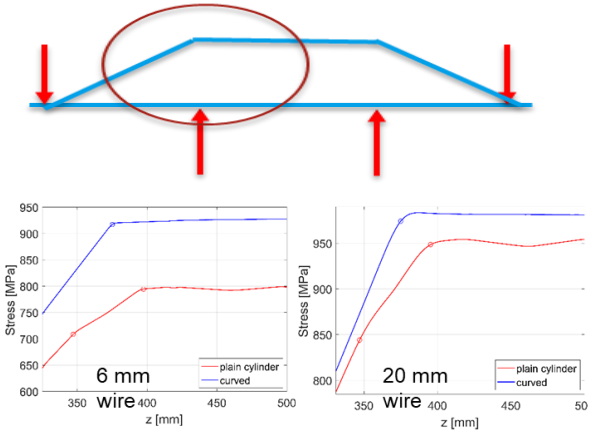

Fig. 4 Stress profile near one of the central supports. Blue line is the curved profile bushing, while red line is the cylindrical bushing.

4. EXPERIMENTAL TESTS

Twenty-nine semi-finished bars for the realization of helical springs have been tested, in[4] the authors made also tests on rectified tempered bars made from 39NiCrMo3 steel alloy.

The bars have been chosen of two different diameters (8 and 11.5 mm) and are made of a 54SiCr6 high resistance steel alloy thermally treated to reach an ultimate tensile strength greater than 1600 MPa. The applied stress ranged from 550 to 1000 MPa. Almost all of the 29 bars showed a rupture located inside the central section as shown in Fig. 5, only one has shown a rupture located outside.



Fig. 5 Detail of a fracture inside the central section of one of the tested wires.

Fatigue tests have been conducted both in the finite and infinite life region. For the finite life fatigue region, either three or four different stress levels have been tested; for each stress level at least three replicas have been tested.

To extract the fatigue limit, an accelerated staircase method has been adopted to limit the number of specimens. The obtained experimental curves are shown in Fig. 6.

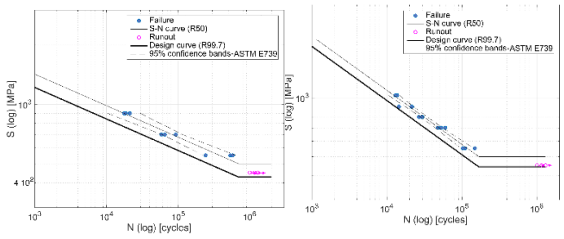

Fig. 6 Wöhler's curves obtained on 8mm (left) and 11.5 mm (right) wires

In Fig. 7, the fractographic image of the fracture surface of specimen number 2 is shown. This specimen has a diameter of 8 mm and an applied load of 1000 MPa. From the picture, it can be observed the relatively large overload zone (indicated with "o" in the picture), clear indication of a high applied stress. The presence of different ratchet marks and multiple crack initiations indicates that the stress on the surface of the specimen was pretty uniform.

The location of the fracture zones and the fractographic image prove that the test bench presented in this paper is actually able to provide a four point rotating bending load situation, without relevant stress concentration at the supports.

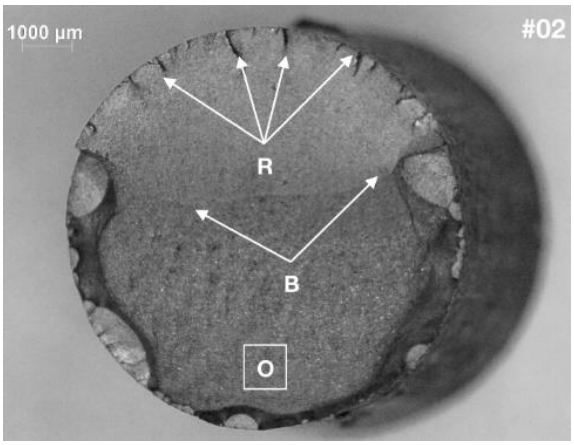

Fig. 7. Specimen #02 (diameter 8 mm, applied load 1000 MPa), fractographic image. O = overload zone; B = beach marks; R = ratchet marks

5. CONCLUSION

In the paper, a new test bench for the four point bending fatigue test of semi-finished bars has been

presented and described.

The test bench was developed to assess fatigue performances of semi-finished steel wires used for the production of helical springs employed in the automotive field.

The test bench has been designed in order to guarantee a constant bending moment in the central part of the wire.

A sensitivity analysis has been performed to maximise the accuracy of the test bench and to highlight the critical geometrical features to be monitored during the construction of the machine.

Special plastic bushings with a curved inner surface have been designed to support the wire while rotating. Finite elements analyses have been performed in order to optimise the bushings inner profile.

Experimental fatigue tests have been conducted on 54SiCr6 tempered steel wires used for manufacturing helical springs for automotive applications. The specimens have been characterised both in the finite and infinite life fatigue regions. Out of 29 tested wires, in 28 cases the wires have broken in the central part.

ACKNOWLEDGEMENTS

The authors would like to thank “ANCCEM” (http://www.anccem.org/) for their support in participating to the conference.

REFERENCES

1) C. Berger and B. Kaiser, “Results of very high cycle fatigue tests on helical compression springs”, International Journal of Fatigue, vol. 28(11), pp. 1658-1663, 2006.
2) Y. Akiniwa, S. Stanzl-Tschegg, H. Mayer, M. Wakita, K. Tanaka, “Fatigue strength of spring steel under axial and torsional loading in the very high cycle regime”, International Journal of Fatigue, vol. 30(12), pp. 2057-2063, 2008.
3) D. Angelova, R. Yordanova, T. Lazarova, S. Yankova, “On Fatigue Behavior of Two Spring Steels. Part I: Wöhler Curves and Fractured Surfaces”, Procedia Materials Science, vol. 3, pp. 1453 – 1458, 2014.
4) F. Ballo, M. Carboni, G. Mastinu, and G. Previati, Tempered Wire Fatigue Testing, SAE Technical Paper 2019-01-0532, 2019, https://doi.org/10.4271/2019-01-0532.

Miniaturised Fatigue Testing Devices to characterise Fatigue Damage Evolution

Anna WILDEIS, Matthias THIMM, Robert BRANDT, Hans-Jürgen CHRIST and Claus-Peter FRITZEN

University of Siegen, Paul-Bonatz-Straße 9-11, 57076 Siegen, Germany

TEL:+ 49-271-740-4744 e-mail:anna.wildeis@uni-siegen.de

Two miniaturised testing devices are introduced that allows for in-situ fatigue testing under uniaxial and torsional loading, respectively, in a confocal laser microscope. The design and the functional principle of the miniaturised testing device for uniaxial loading, which was developed and built at the University of Siegen, will be presented. Furthermore, an exemplary insight in the successful use of the miniaturised testing device for characterising the fatigue damage evolution in a martensitic spring steel will be shown. The miniaturised testing device for torsional loading is still in the assembly phase. This study shows the design concept, the combination of the components and an additional lightweight load frame made of CFRP.

Keywords: In-situ analysis, Miniaturised fatigue testing devices, Martensitic spring steel, Cyclic torsion

1. INTRODUCTION

The technology for manufacturing of coil springs has been significantly improved within recent years driven by the needs of lightweight design. However, the common standards for the design of coil springs are quite conservative (e.g.[1)]), leading to unnecessarily heavy components. In order to ensure sufficient reliability, springs suppliers as well as their customers are facing time-consuming and expensive component testing programmes. An unerring life time prediction methodology, however, would allow to reduce these efforts. This requires an accurate understanding of the relevant damage mechanisms caused by axial and torsional loading.

The evolution of fatigue damage is commonly subdivided into four phases, i. e., crack initiation, microstructurally short fatigue crack propagation, long crack growth and eventually fracture. The phases of crack initiation and initial microstructure-controlled crack propagation, which may account for up to 90% of the fatigue life in the high cycle fatigue regime[2)], are the focus of the lifetime assessment concept aimed at in this study. Furthermore, the impact of compressive residual stresses, which are nowadays implemented by sophisticated shot peening technologies, is addressed. According to Forsyth[3)] the fatigue crack propagation itself can be divided into two stages. Stage I corresponds to short crack propagation, while stage II is equivalent to long crack propagation. The stage I crack propagation occurs on single crystallographic slip bands and is driven by the maximum shear stress (loading mode II). For uniaxial loading, this leads to a short crack propagation on slip bands with the highest Schmid-factor inclined at an angle of 45° with respect to the loading axis and for torsional loading, the relevant straining mode of coil springs, to an angle of 0° or 90° with respect to the rotation axis (see Fig. 1 b)). Stage I crack propagation is significantly influenced by the microstructure[4)]. Hence, it needs to be examined as a function of cycles considering the characteristics of the nearby microstructure before and during the test. For this purpose, ex-situ fatigue tests can be carried out by periodically interrupting, dismounting and transferring of the specimen from the fatigue testing machine to a microscope for inspection. This method is laborious and can lead to an additional deformation of the gauge length of the specimen. In order to eliminate these disadvantages, the use of an in-situ testing technique by means of a miniaturised fatigue testing device is to be favoured. Over the years several miniaturised testing machines for uniaxial loading have been developed by different research groups (e. g. [6,7)]). However, only one study has been found dealing with the development of a miniaturised torsion fatigue testing device[8)] that is feasible to test micro-scale specimens under small tensional and torsional loadings within a SEM. A linear motor and a DC motor are driving the device.

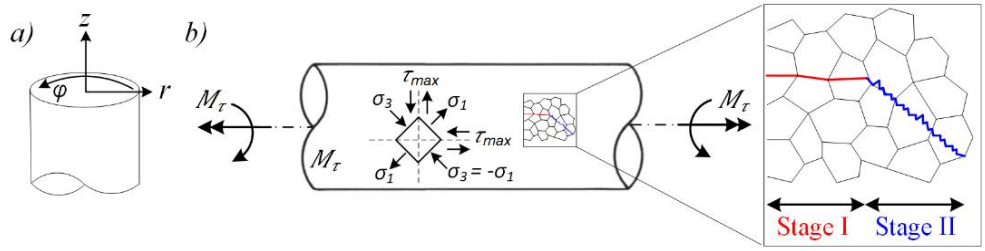

Fig. 1: a) Definition of the cylindrical coordinate system b) Stress state and crack propagation under torsional loading [5)]

Steel 316L wires with a nominal diameter of 200 µm have been cyclically tested by means of this device. It meets the challenge to characterise the mechanical behaviour of micro-scale components under complex loading conditions.

The present study introduces the benefits of a miniaturised in-situ fatigue testing device under uniaxial loading and presents the development of a miniaturised in-situ torsion fatigue testing device. The results achieved by means of both miniaturised in-situ fatigue testing devices will provide valuable information about short crack propagation to improve the lifetime prediction of high-strength, martensitic spring steels.

2. STRESS CONDITIONS

For the cylindrical specimen (s. Fig. 1 a)) a cylindrical coordinate system (r,φ,z) is chosen, where the z-direction coincides with the cylinder axis. The r and φ coordinates span the plane orthogonal to the z-axis. Under uniaxial loading at a load F_z, pure tensional stress σ_{zz} homogeneously acts within the cross section of a specimen perpendicular to the load axis, i.e., the stress tensor $\hat{\sigma}$ reads

$$\hat{\sigma} = \begin{pmatrix} 0 & 0 & 0 \\ 0 & 0 & 0 \\ 0 & 0 & \sigma_{zz} \end{pmatrix}. \qquad (1)$$

Under torsional loading at a torque M_T the stress tensor at the surface of a cylindrical fatigue specimen reads

$$\hat{\sigma}_t = \begin{pmatrix} 0 & 0 & 0 \\ 0 & 0 & \tau_{\varphi z} \\ 0 & \tau_{z\varphi} & 0 \end{pmatrix} \qquad (2)$$

With $\tau_{\varphi z}=M_T/W$ and W being the polar moment of inertia. While torsional loading exerts a pure shear stress on the specimen (s. Eq. (2)), uniaxial loading includes a hydrostatic component as well

$$\hat{\sigma} = \frac{1}{3}\begin{pmatrix} \sigma_{zz} & 0 & 0 \\ 0 & \sigma_{zz} & 0 \\ 0 & 0 & \sigma_{zz} \end{pmatrix} + \frac{1}{3}\begin{pmatrix} -\sigma_{zz} & 0 & 0 \\ 0 & -\sigma_{zz} & 0 \\ 0 & 0 & 2\sigma_{zz} \end{pmatrix} \qquad (3)$$

This shows that torsional testing is required to examine crack initiation and growth under shear stress without the impact of hydrostatic stress.

3. MINIATURISED TESTING DEVICE FOR UNIAXIAL LOADING

3.1 DESIGN AND FUNCTIONAL PRINCIPLE

The design and the functional principle of the miniaturised testing device for uniaxial loading is shown in Fig. 2 a). The samples are clamped between the load frame and the sample slide. It is driven by a piezo actuator (PSt 1000/35/125 VS 45 Thermostable, Fa. Piezomechanik GmbH), which is installed in a traverse that is installed in the load frame. The stiffness of the piezo actuator is $C_{Pz} = 360\,kN/mm$ and it´s maximum extension at maximum electrical voltage $U = 1000V$ is $125\,\mu m$. In the blocked condition, the maximum force is $45\,kN$ (see Fig. 3 a)). In combination with the integrated disk springs with a stiffness of $C_{CP} = 20{,}5\,kN/mm$, the sample can be loaded with a maximum force amplitude of $F = 1280\,N$. The wedge plates enable a bearing without clearance. The stress ratio can be set via the disk springs and the actuator stroke before the sample is clamped. The applied force can be measured by means of a quartz crystal force sensor (type 9134B29, Fa. Kistler) with an accuracy of <0,01 N, which is installed between the two parts of the sample slide, and is used as an input signal for the peak optical power control designed by LabVIEW.

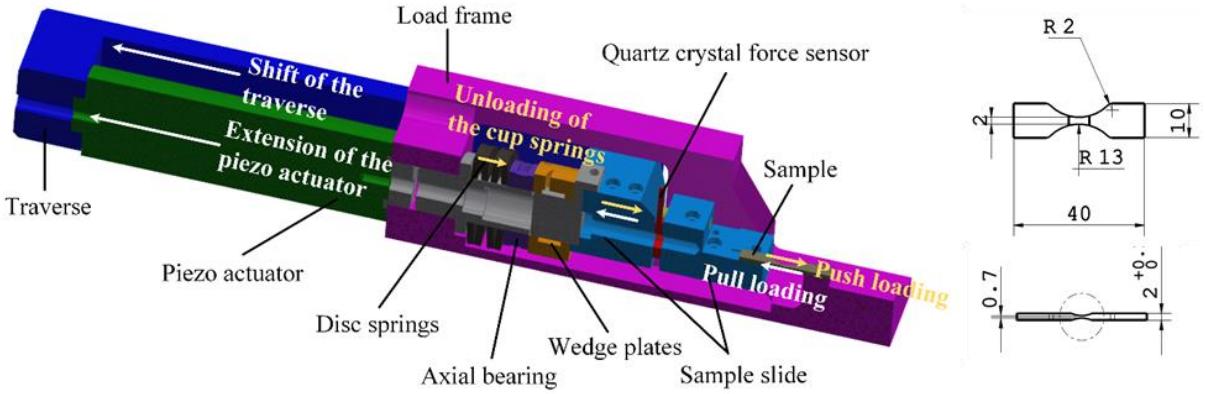

Fig. 2: a) Design and functional principle and b) sample geometry of the miniaturised testing device for uniaxial loading

As a result of a continuous target-performance-comparison, a function generator transmits a sinusoidal voltage signal to the power electronics, which is connected to the piezo actuator. This sinusoidal voltage signal corresponds to the desired force amplitude. The power electronics delivers a voltage of 0 V<U<1000 V and enables a test frequency of 30 Hz. The miniaturised testing device can be installed in a scanning electron microscope as well as in a confocal laser scanning microscope (see Fig. 3 b). Further information regarding the design and the functional principle of the miniaturised testing device are reported by [9].

3.2 Sample geometry

The sample geometry can be seen in Fig. 2 b). Its cross section A_s=1,4 mm² is relatively small to achieve a failure of the samples in spite of the low maximum force amplitude of the miniaturised testing device. Furthermore, to facilitate a damage localization, the cross section is further reduced by two shallow notches at opposite sides with a notch factor of $k_{(v,UD)}$=1,3 each.

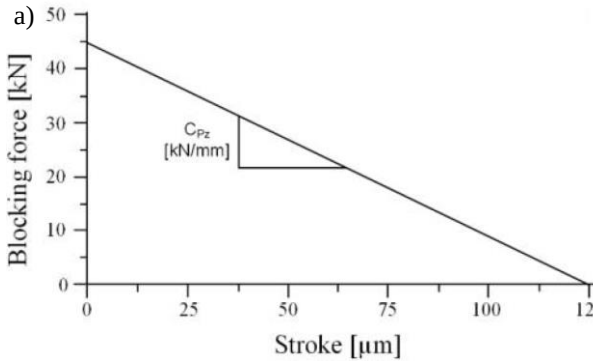



Fig. 3: a) Blocking force-stroke-diagram of the used piezo actuator b) Installation of the miniaturised testing device into a confocal lasermicroscope

Table 1: Chemical composition in weight-% and mechanical properties of 54SiCr6

C	Si	Mn	Cr	R_m [MPa]	$R_{p0,2}$ [MPa]
0,53	1,43	0,66	0,63	1750	1550

3.3 IN-SITU FATIGUE TESTS CONDUCTED ON A HIGH STRENGTH STEEL

The suitability of the miniaturised testing device for characterising fatigue damage evolution is shown up at the example of martensitic spring steel 54SiCr6 samples (chemical composition and mechanical properties can be found in Table 1). The material was austenitized at 1080°C for 100 min. in vacuum and quenched down to RT with compressed nitrogen. Subsequently, tempering happened at 400°C for 1 h in inert gas. The resulting martensitic microstructure comprises an average prior austenite grain size of $125\ \mu m$.

The surfaces of the samples were successively ground with SiC paper up to a grain size of 4000 and finally

polished with a colloidal silicon suspension with a particle size of $0{,}25\ \mu m$. The stress-controlled in-situ fatigue testing with a stress ratio of $R = -1$ happened with a frequency of 10 Hz at stress amplitudes of 680 MPa and 600 MPa, respectively. To characterise the fatigue damage evolution, images of the sample surface were captured in predefined intervals by means of a confocal laser scanning microscope.

The results of the in-situ fatigue tests are presented in Fig. 4. The fatigue damage evolution is described via the crack density ρ_n as a function of the number of cycles N. The crack density describes the ratio of the total accumulated crack length L_n of all detected cracks to the monitored area A_n. As can be seen in Fig. 4, the crack density rises with increasing number of cycles. Furthermore, an even more pronounced fatigue damage

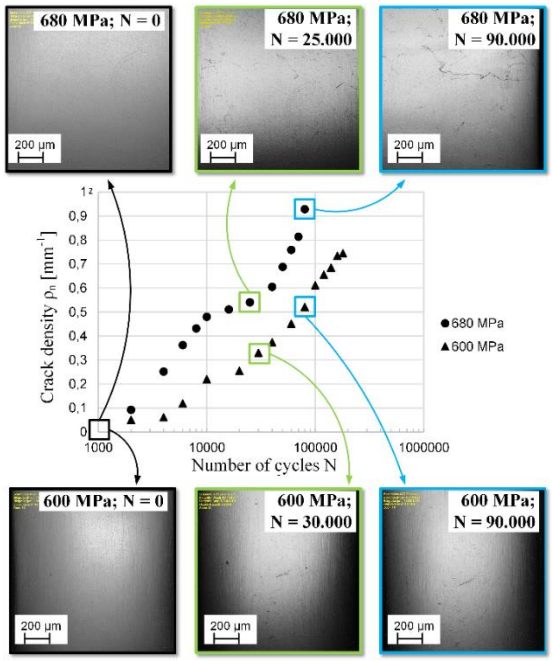

Fig. 4: Crack density verses the number of cycles for two different stress amplitudes

occurs on the surface of the sample loaded with the higher stress amplitude of 680 MPa.

The results in Fig. 4 clearly demonstrate the suitability of the miniaturised testing device for characterising fatigue damage evolution in a high-strength, martensitic spring steel.

4. DEVELOPMENT OF THE TORSION FATIGUE TESTING DEVICE

4.1 Specimen geometry and requirements for the testing device

The torsion fatigue specimen geometry is shown in Fig. 5. A shallow notch of radius $R = 20\ mm$ guarantees that crack initiation is localized to this small area and enables EBSD analyses, which require a flat specimen surface. FEA (s. Fig. 6) shows the shear stress concentration in the notch root at a notch factor of $k_{v,T} = 1{,}5$. Furthermore, FEA discloses the resulting warping torsion stress in the notch centre (see Fig. 7). No warping stresses occur along the symmetry axes of the specimen, and thus, the notch centre is free of additional hydrostatic stresses by warping torsion, similar to a rectangular beam[10].

Here, the torsional fatigue testing is addressing the high cycle fatigue regime at a test frequency of $f \approx 5\ Hz$ for sinusoidal loading. Considering a martensitic spring steel with an ultimate tensile strength of $\sigma_{UTS} = 1750\ MPa$, the testing device must provide a torsional stress of at least $\tau = 1400\ MPa$. Accordingly, the power unit has to provide a torque of $M_t = 5\ Nm$ with a safety factor of at least 2.

The very same confocal laser-scanning microscope a mentioned before will be used with a restriction in installation height $H = 95\ mm$ and a loading maximum $m \leq 15\ kg$. Thus, the load frame must have a low weight and a sufficient stiffness. The additional von Mises stress due to the limited stiffness of the miniaturised torsion fatigue device is not allowed to exceed the nominal value by more than $14\ MPa$ (1 % of the maximum applied shear stress).

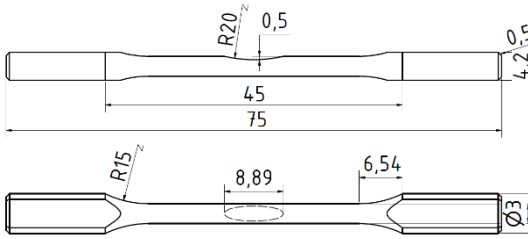

Fig. 5: Specimen geometry for the miniaturised torsion fatigue testing device

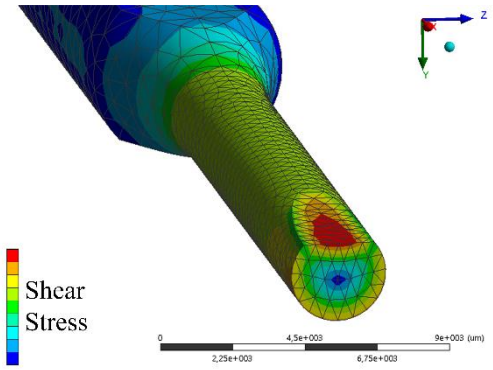

Fig. 6: Shear stress distribution in the cross

section of the developed specimen

The design of the miniaturised torsion fatigue testing device is shown in Fig. 8. The sample fits into a groove of the sample holder, which complies with the shape and dimension of the fixing section of the sample. This leads to an easy fixing and a form closure of the samples. Drill holes with a diameter of 3 mm in each sample holder enables a force closure as well by means of set screws. An integrated linear guidance enables a shift of one of the sample holders leading to the possibility of testing of samples with different lengths. A servomotor (Fa. Siemens) delivers a maximum torque of M_t=12 Nm at a test frequency of up to $f \approx 100$ Hz for sinusoidal loading. The angle of twist is adjusted via motor control.

A torque sensor (Fa. HBM) with an accuracy class of $\pm 0{,}5$ % is applied for torque measurement. To avoid a damaging misalignment of the torque sensor, two torsion-resistant stiff metal bellows couplings are integrated.

4.2 LOAD FRAME

In order to meet the requirement of low mass at high stiffness for the load frame, three different materials have been considered, namely structural steel, aluminium and titanium.

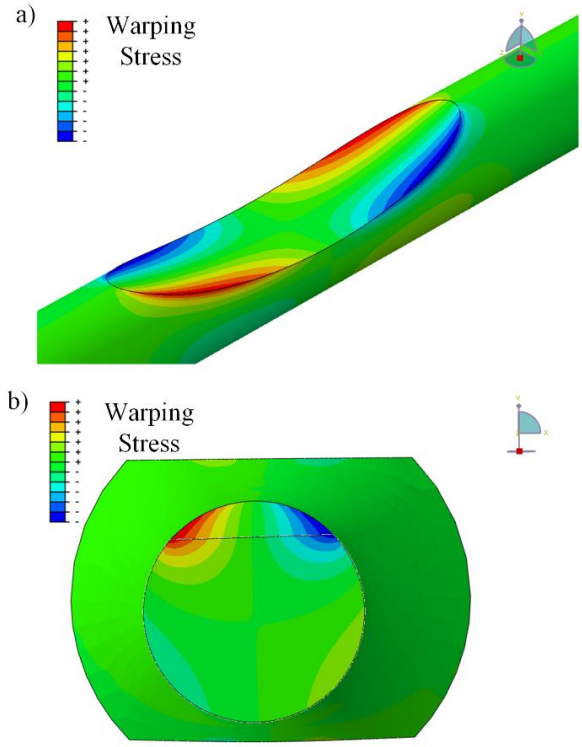

Fig. 7: Expected uniaxial warping stress a) in the shallow notch and b) in the cross section

The resulting weights and the maximum displacement in the middle of the sample holder of the corresponding load frame at a torque of 5 Nm are listed in Table 2 and an example of the related FEA simulation of the aluminium load frame is shown in Fig. 9

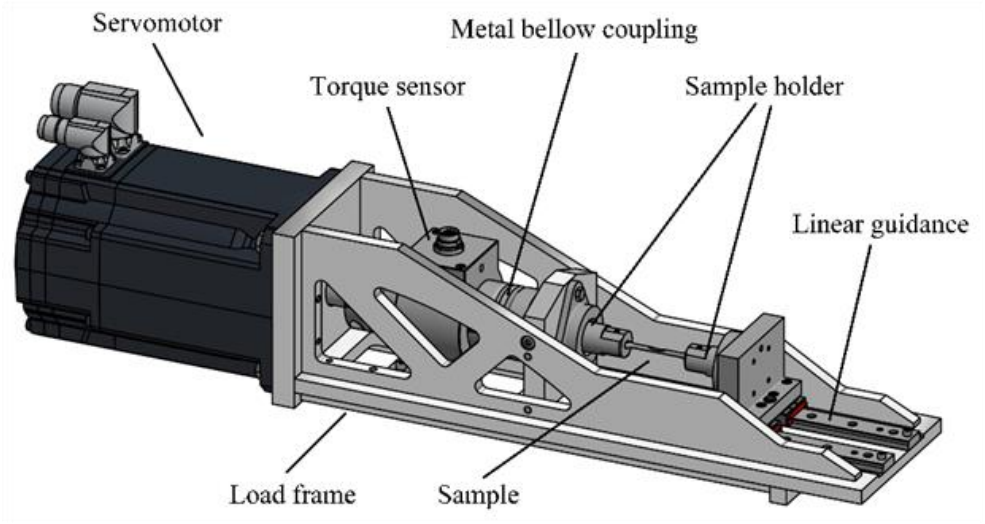

Fig 8: Design of the miniaturised torsion testing device

Table 2. Weight and maximum displacement depending on the material.

Material	Weight (kg)	Displacement (µm)
Structural steel	7.6	4
Aluminum	3.6	11
Titanium	4.3	9

A load frame made of structural steel provides minimum displacement, while a load frame made of aluminum has the lowest weight. Since an easy handling of the miniaturised torsion fatigue testing device plays a major role in the design of the load frame, aluminum offers the better alternative. To evaluate the effect of displacement of the aluminum load frame on the specimen, additional FEA simulation were made. Compared with a rigid load frame of unlimited stiffness, it disclosed an additional von Mises stress of 0.64 MPa, which is far below the critical value of 14 MPa. Therefore, the next step of this study will be the fabrication of the load frame made of aluminum according to the design seen in Fig. 8. In order to prevent an additional bending torque for the specimen, the motor shaft of the servomotor, the specimen and the specimen holder are coaxially aligned of the miniaturised fatigue testing device and the conformance will be checked by means of strain gauges attached to a sample. For a design verification a three-dimensional model was printed and mounted into the confocal laser-scanning microscope. As can be seen in Fig. 10, the load frame fits into the assembly space and provides the in-situ testing capability in the confocal laser-scanning microscope.

Since for torsional testing the investigation of crack initiation and crack growth occurs without a tensional hydrostatic stress, a stress supported crack opening during the in-situ fatigue test may not occur.

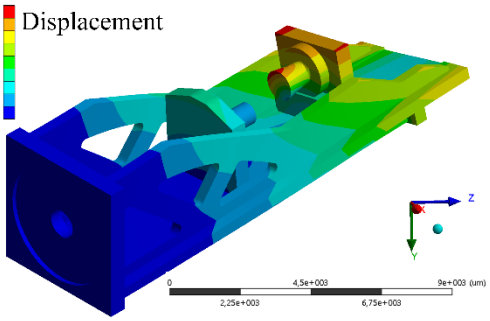

Fig 9: Displacement of the aluminium load frame at a torque of 5 Nm



Fig. 10: Printed three-dimensional model of the load frame

Consequently, this may prevent for a convenient examination of the crack initiation and propagation. In this particular case, an additional bending unit has to be integrated into the load frame, in order to enforce a crack opening during the surface recording times.

4.3 ADDITIONAL LIGHTWEIGHT LOAD FRAME MADE OF CFRP

As the sample stage of the confocal laser scanning microscope can only be loaded with a maximum load of 1,3 kg, the miniaturised torsion testing device needs to be mounted on an additional test bench analogue to the test bench for the miniaturised testing device for uniaxial loading, which can be seen in Fig. 3 b). However, this leads to the consequence, that the automatic surface scanning function of the confocal laser scanning microscope cannot be used, resulting in a higher inspection effort. Therefore, an additional lightweight load frame made of CFRP shall be manufactured. The design of the CFRP load frame allows for dismounting of the load frame including the clamped sample, thus enabling a quasi in-situ testing. The prototype of the CFRP load frame has a total weight of 1,2 kg including bearing blocks and sample holders made of aluminum (s. Fig. 11).

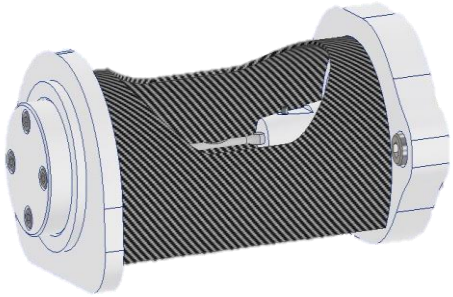

Fig. 11: Prototype of the CFRP load frame

The results of a FEA simulation analogous to the one made in chapter 4.2 show, that the maximum displacement of the CFRP load frame at a torque of 5 Nm is to 67 µm, leading to an additional von Mises stress of 6,2 MPa in the sample, which is still below the critical value of 14 MPa. In comparison to the aluminum load frame shown in Fig. 9, a weight reduction of 66 % is achieved and enables the usage of the sample stage of the confocal laser scanning microscope.

5. OUTLOOK

During the project, the damage mechanisms of fatigue in a high-strength, martensitic spring steel will be analysed in detail under cyclic loading by means of a miniaturised fatigue testing device for uniaxial loading and a new miniaturised torsion fatigue testing device, respectively. The investigation is focussing on the effect of the martensitic microstructure on the short crack propagation behaviour, e.g. to what extent prior austenite grain boundaries[11] or the block boundaries[12] will act as obstacles. Furthermore, the impact of compressive residual stresses on short crack propagation, e.g. in terms of the occurrence of crack-closure effects, will be investigated by additional testing of shot peened specimens. In order to analyse the changes of the residual stress state in front of the crack tip during the testing, the miniaturised fatigue testing device is also designed to be used at a synchrotron facility such as the DESY in Hamburg.

On the numerical side, in order to accurately represent the material, further methods of discretisation will be implemented and their ability to reproduce effects like residual stresses will be examined

6. CONCLUSION

The reasoning for the development of a miniaturised torsion fatigue testing device for the characterisation of the damage mechanisms caused by torsional fatigue and the derived realization concept for such a device is presented in this study.

It was shown that the warping stress does not affect the notch ground and will not interfere with crack initiation and crack growth. Therefore, the material can be examined without uniaxial stresses influencing the results.

The suitability of the miniaturised testing device for characterising fatigue damage evolution in a high-strength, martensitic spring steel was shown on the basis of two in-situ fatigue tests.

The developed miniaturised torsion fatigue testing device was found to be best driven by means of a servomotor with a maximum torsional moment of $M_t = 12\,Nm$ and a maximum test frequency $f \approx 100\,Hz$. The specimen clamping is realised by traction and form closure. In order to reduce the weight of the miniaturised torsion fatigue testing device, aluminum was identified as the material of choice for the load frame. Furthermore, the load frame was optimized in terms of stiffness, to reduce additional von Mises stresses in the specimen. A further weight reduction of 66 % is achieved by use of a CFRP load frame that enables the usage of the sample stage of the confocal laser scanning microscope, leading to a lower inspection effort.

ACKNOWLEDGEMENTS

The authors thank Deutsche Forschungsgemeinschaft (DFG) for financial support.

REFERENCES

1) R. Rennert, E. Kullig, M. Vormwald, A. Esderts, D. Siegele, Rechnerischer Festigkeitsnachweis für Maschinenbauteile aus Stahl, Eisenguss- und Aluminiumwerkstoffen, VDMA-Verlag (2012)
2) H.-J. Christ, Ermüdungsverhalten metallischer Werkstoffe, 2nd Edition, (Wiley-VCH ISBN 978-3-527-31340-2. 2009) pp120-121.
3) P. J. E. Forsyth, Act. Met. 11 (1963), pp703-715.
4) U. Krupp, Fatigue Crack Propagation in Metals and Alloys, (Wiley-VCH ISBN 978-3-527-31537-6. 2007) pp161-162.
5) R.H. Li, P. Zhang, Z.F. Zhang, Mater. Sci. Eng. 574 (2013), pp113 –122.
6) W.-F. Li, X.-P. Zhang, Mater. Sci. Eng. A318 (2001), pp129-136.
7) I. Roth, U. Krupp, H. J. Christ, M. Kübbeler, C.-P. Fritzen, Proc. of ESOMAT, Prague (2009), EDP Sciences.
8) S. Fu, L. Wang, G. Chen, D. Yu, X. Chen, Rev. Sci. Instrum. 87, 015111 (2016).
9) I. Roth, Untersuchungen zum Ausbreitungs-verhalten mikrostrukturell kurzer Ermüdungsrisse in metastabilem austenitischen Edelstahl, Dissertation Universität Siegen, Siegener werkstoffkundliche Berichte, H.-J. Christ (Hg.), Band 5, 2012.
10) I. Szabo, Höhere Technische Mechanik, Springer-Verlag Berlin (1977).
11) A. Brückner-Foit, X. Huang, Int. J. Fatigue 28 (2006), pp963-971.

12) A. Giertler, Doctoral Thesis RWTH Aachen (2020)

Design and Analysis of Composite Structures for Automotive Applications. Chassis and Drivetrain

Vladimir KOBELEV, Jörg NEUBRAND
Muhr und Bender KG, Mubea-Platz 1, 57439 Attendorn, Germany
TEL:+ 49- 2722 62 9503 e-mail: vladimir.kobelev@mubea.com

Abstract. The optimal structural design with lightweight materials is one of the principal tendencies in contemporary development of passenger cars because the increasingly stringent emissions reduction requires through weight reduction. The use of composite material promises some of the most attractive improvements; however, requires the redesign parts and components, which are traditionally made of steel. Especially carbon-fiber reinforced plastics and glass-reinforced plastics have pronounced potential in mass-reduction of vehicles. Cost of the product remains a key issue. As with any lightweight material, all further expenses, which incurred in addition to the cost of the base material, must be accounted. The major task to make the product attractive to customers and the market is to reduce the construction and production costs as much as possible with the significant weight reduction and extra benefits.

Keywords: Design, Composite Structures, Automotive Applications

1. CONCEPTS OF HIGH STRENGTH COMPOSITE ELEMENTS

The lecture presents the concepts of high strength elastic elements of automotive chassis and drivetrain made of composite materials from the point of classical mechanics. We study the principal ideas, which are necessary for understanding of analysis and optimization of composite elements. The building blocks of physical background serves the anisotropic elasticity on structural and micro-mechanical levels, anisotropic creep and elements of fracture mechanics.

In times of climate change and rising emissions in environment, lightweight construction has found its way into almost all industries. The authorities, particularly in the automotive industry, formulate the endlessly decreasing targets in the emission reduction. Because the increasingly stringent emissions can be minimized through weight reduction, the optimal structural design with lightweight materials is one of the principal tendencies in contemporary development of passenger cars. Some of the most attractive improvements have been seen in the use of composite, is to replace parts and components traditionally manufactured from steel. Especially carbon-fiber reinforced plastics and glass-reinforced plastics have great potential to reduce the weight of passenger cars. Cost of the product remains a key issue. As with any lightweight material, all further expenses, which incurred in addition to the cost of the base material, must be accounted. The major task to make the product attractive to customers and the market is to reduce the lightweight construction and production costs as much as possible with the significant weight reduction and other extra benefits. Despite manufacturing processes were continuously improved, there is still a substantial progress to be achieved for the cost-effective mass production. Safety is another dominant criterion for passenger cars. Hence, the new designs must be structurally robust enough to adhere to current and future crash and safety targets.

Over recent years, car body and drivetrain have come under deep examination in the attempt to save mass of structure and a range of innovative concepts be developed. Lightweight construction has become an optimization goal that is valid to several components of automobiles.

Weight reduction of the chassis has gained in importance as well. The chassis has a substantial potential of weight reduction [1)]. Among other lightweight materials for chassis design, the glass-fiber reinforced plastic provides a good alternative to steel. Moreover, the unsprung mass can be lessened. This factor brings distinct advantages for the driving dynamics and comfort.

2. OPTIMIZATION PRINCIPLES FOR CHASSIS ELEMENTS OF MADE OF COMPOSITE MATERIALS

The manuscript “Durability of Springs” [2)]exhibits the

mechanics of the elastic elements made of steel alloys with focus on the metal springs for automotive industry.

The book [3] presents the concepts of high strength elastic elements of automotive chassis and drivetrain made of composite materials. The book studies the principal ideas, which are necessary for understanding of analysis and optimization of composite elements. Its content extends and relates logically to the work [2].

The book [3] investigates the distinctive structures of composites, such their anisotropy, inhomogeneity, stress coupling and direction on loading dependence. The derivation of all equations and formulas follow from the declared propositions. The anisotropic elasticity on structural and micro-mechanical levels, anisotropic creep and elements of fracture mechanics serve as the building blocks of physical background for the book. This book is recommended for engineers dealing with design and development of chassis and drivetrain, graduated from automotive or mechanical engineering courses in technical high school, or in other higher engineering schools. The researchers, working on elastic elements and energy harvesting equipment, will also find a general review for technology and simulation of composite structural elements.

In Chapter 1 the basics of the anisotropic materials and the fiber composites, as they are needed in the context of this work, are to be presented. Based on the structure of fiber composites and the characteristic properties of the fibers and matrix, the special features of the mechanical properties of a unidirectional single layer are described. Further, the calculation equations for determining the engineering constants are displayed. The Chapter explains the deformation behavior of laminates and the transformation laws with tensor and vector notations of Voigt and Kelvin.

Strength of the unidirectional material as well as layered composite made of variously focused unidirectional layers can be investigated by means of two main approaches: phenomenologically and micromechanically in Chapter 2. In natural sciences, phenomenological theories (in contrast to microscopic or structural, for example) are those theories, which describe only phenomena and their consequences, without explaining their causes. Chapter 2 presents the traditional phenomenological approach applies the local stress or average stress failure criteria, based on different approximations of the experimental strength data. Finally, the transformations of failure criteria between inclined coordinate systems. The phenomenological approach applies the local stress or average stress failure criteria to form strength models. These models are based on fitting of the experimentally acquired failure data.

The alternative approach studies the destruction from the viewpoint of the micromechanics. The strength characteristics of the unidirectional composite are explained in Chapter 3 from the positions of failure mechanisms for fibers and matrix. For this purpose, the micromechanical models of both components are developed. This approach provides the qualitative understanding of failure and explains the hypothetical mechanisms on structural level of the composite material. The explanations propose the ways for the optimization and for the proper material selection. However, since the micromechanical criteria are based on several hypotheses, they cannot be such precise, as the phenomenological criteria, which are grounded on the direct strength measurements. Chapter 3 deals with the modeling of the fracture process of a fiber composite material with the parallel fiber orientation. The problem of fiber pullout from the matrix is investigated. The elastic behavior of the fibers and elastic-plastic behavior of the matrix are presumed. The zones around and far from the crack tip are considered independently. The problem for the crack, whose surfaces are bridged by undamaged fibers, is solved. The effect of the fiber draw from the surface of the crack is associated with the jump of the effective displacements over the crack surface. The equations of a plane and a rotationally symmetric problem of crack propagation are grounded on the fiber pullout solution. The results of the numerical solutions and the fracture toughness evaluations are described. Further, the debonding on the surface of fibers under the action of tensile load in fiber direction is rigorously studied. The debonding region is modeled as the cylindrical crack on the surface of the fiber. The closed form solutions are achieved. The main result is the following. For the relatively long debonding zone the stress intensity factor at the tip of the debonding crack does not depend on the crack length. Thus, for the cyclic load application, the elongation of the debonding crack remains constant and crack length is proportional to the number of load cycles. This effect lead to continuous degradation of material with the increasing of cycle number, for example, explains the near linear reduction of longitudinal module with the duration of cyclic load.

Chapter 4 discusses the general principles for the optimal design of structures, based on the anisotropic properties of materials. Problems of maximizing the ultimate rupture load, total stiffness and stored energy capacity are formulated. The optimal orientation of the

anisotropy axes in the structure elements is studied, based on tensor notation in space and vector and tensor notations in the six-dimensional stress space. Necessary optimality conditions are presented using different notations.

Chapter 5 explores the torsion and bending of the driveshafts made of composite. The driveshaft is modeled as an anisotropic rod with the solid or the thin-walled tubular cross-section. The dominant load on the driveshaft is torque that causes high shear stress in the material. The alternating torque causes al-so twist vibration modes. The secondary loads are the bending and tension. The resulting stresses from the secondary loads are usually moderate, but these loads can provoke the Greenhill's torque instability and bending vibration modes. From the lightweight viewpoint, the advantageous design of the driveshafts is the thin-walled tubular structure. The corresponding model of the thin-walled anisotropic driveshaft is based on the kinematic hypotheses and equations of thin anisotropic shells. The kinematic hypotheses assume that the profile of the normal cross section of the thin-walled shaft is not distorted but is instead only rotated and displaced in space. Using the kinematic hypotheses, the strains and curvatures of the middle surface of the shaft are displayed. The strain equations are obtained by varying the potential energy functional of the classical theory of anisotropic shells. Finally, the problem of determining the critical load for a thin-walled driveshaft in axial compression is investigated. The proposed model is appropriate for the analysis of driveshafts made of multilayered composite materials. As mentioned above, the elongated driveshafts are subjected to Greenhill's twist buckling. If twist instability occurs, the straight axis of twisted rod transforms to the helical spiral curve. This motivates the pursuit for the optimal cross-sectional shape of the driveshaft. Remarkably, the optimal shape of cross-section of the shaft for the maximal critical torque is the hollow triangle. On the contrary, circular hollow cross-section leads to the minimum shear stress under given torque. Accordingly, the short driveshafts must have preferably the circular hollow cross-section, while the lengthy driveshafts should have the triangular hollow form of profile.

Chapter 6 reviews the common types of wheel suspensions of the vehicles. The structural elements of wheel suspensions, except of the spring elements, remain in this context solid. The elementary introduction of vehicle dynamics provides the basis for subsequent investigation of flexible structural elements of wheel suspensions and study of the coupling effects.

Chapter 7 studies the dynamics of vehicle, taking into consideration the elasticity of its chassis components. Specifically, this section treaties in details the passenger car with the twist-beam axle. At first, the basic designs of cars with twist-beam axle are described, the differentiations to other wheel suspensions are studied and the advantages and disadvantages of this type of suspension are recorded. Later, the influences of the flexible axle on driving dynamics are pronounced. The accounting of the coupling effects during fast cornering with the strong lateral acceleration is exemplified. The suspension elements made of composite materials possess some interesting and distinctive mechanical features, which proper use can positively influence the dynamic of a vehicle. At first, the anisotropy provides an additional coupling between the degrees of freedom and supplementary interaction between the wheels and body. At second, the lower modulus of elasticity of material relative to its strength, leading to excessive elastic response of suspension elements. At third, the unusual ratios of flexibilities in different directions have an effect on the steering behavior of a vehicle. The models demonstrates these properties of composite materials on lateral dynamics.

Chapter 8 studies the design of anisotropic helical and conical springs for automotive applications. Helical composite springs possess the form of spiral of circular cross-section. The distance between the successive coils of a spring is a slowly varying function, so that the axis of the wire forms a helix with a constant or a variable pitch and the anisotropic wire of spring is predominantly in the state of pure torsion. The spring is additionally twisted along the axis of helix and the bending of wire along vertical axis happens. The design formulas for anisotropic helical springs are developed and the optimization problems are studied in closed form. Another frequent kind of springs is the conical spring. The ring thickness is constant and the applied load is evenly distributed over the upper inside edge and lower outside edge. The structural models for the anisotropic conical springs are developed and design formulas presented. Based on the analytical formulas, the optimization of the conical springs made of composite materials is performed.

In Chapter 9 a helical composite spring is substituted by the hypothetical elastic beam, located along the axis of the helix. This imaginary beam possesses the same averaged mechanical features, as the spring itself. Its elastic proper-ties, as bending, torsion and compression

stiffness, are equal to the matching averaged properties of the helical composite spring. This beam is known as an "equivalent beam" of the composite spring. The "equivalent beam" equations are substantially easier to solve, than the three-dimensional equations of the helical spring. The critical spring properties, as an axial and transversal stiff-ness, buckling loads, fundamental frequencies follow the "equivalent beam" equations. The local properties, like stresses in the wire or contact forces, could be evaluated only with the much more complex equations of the spatial elastic beam. The stability and transversal vibrations of the anisotropic spring are studied from the unified point of view of "equivalent beam" concept. The equations for transverse (lateral) vibrations of the compressed coil springs are also derived. This solution expresses the fundamental natural frequency of the transverse vibrations of the beam as the function of the axial force.

Chapter 10 examines the design and simulation of the leaf springs that withstand primarily the bending. The leaf spring is the most common type of the composite springs. The leaf spring, which mounted in length direction, has wheel-leading function, including absorption of brake forces and lateral forces. The transverse leaf spring has wheel-guiding function, regulates the spring rate of the wheel and the roll suspension of the vehicle. The transversal leaf spring is subjected to two different loads in the vehicle. On the one hand, it takes over the normal lifting suspension of the axle and on the other hand, depending on the design, it takes over some or all of the required roll stabilization of the axle. The lifting suspension can be described as an equilateral load, since both wheels move in the same direction. For the common types of leaf springs, the optimization analysis is performed and the principle mechanical features are explained.

Chapter 11 investigates the mechanical behavior of the corrugated, or meander springs. Meander-shaped spring is the folded form of an elongated leaf spring, connected to the chassis at its ends. Hence, the meander spring possesses the shorter length dimension and allows the packaging in the wheel suspensions of passenger cars. The meander spring is the candidate for the replacement of the helical springs, because the box dimensions of both spring types are comparable. On the other side, the manufacturing of the meander spring of composite material is not such pretentious as its helical pendant of fiber-reinforced composite. This Chapter explains the function of the meander springs, their stiffness calculation and buckling behavior.

In Chapter 12 the time-depending performance of spring elements made of composite materials, which exposed to steady heavy load is studied. The common anisotropic creep laws are implemented for the composite material. For basic spring elements, the anisotropic Norton-Bailey constitutive models with the anisotropic creep function are studied. The Altenbach approach applies the quadratic creep potential similarly to the common Mises-Hill plastic criterion. Analytical models are developed for the relaxation of stresses and creep under constant load. Closed-form solutions of the analytical models of creep and relaxation of composite rods in twist and bending states are presented

3. MATERIAL FACTORS

As mentioned above, reducing weight of vehicles is an indispensable requirement in the automotive manufacturing sector. There are several "material factors", which are used for characterization of the weight reduction. Apparently, the material density is the most trivial material factor in determining the best-suited material for a certain application. The density determines the relative weights of structures, but provides no information about their strength and flexibility. Another, also simple factor is the material price of the mass unit. The specific price factor is determining the material that is best suited for a price-critical application. The price factor, as a sum of raw material price and manufacturing expenses, is a commercially important factor in the material evaluation.

Another factor is the specific strength, or the strength-to-weight ratio of the material. The specific strength of an isotropic material is obviously given by the tensile or yield strength divided by the density of the material. A material with a high specific strength will be suitable for load-carrying elements. There are several secondary criteria of this kind, which depend upon the art of dominant load: uniaxial stress or bending stress. The specific strength factors distinguish whether axial stress or stress due to bending dominates. In the first case, the stress in constant over the cross-section of the part. The specific strength is equal to the tension load divided by the cross-sectional area and density of the material. In the second case, the stress a linear function of thickness coordinate. The specific strength is equal to the bending moment is divided by the resistance moment and density of the material. For the fixed weight of material, the thickness for the material with the lower density is greater. The resistance moment for the material with the lower density is greater as well. Accordingly, the material with lower density possesses higher specific

strength for bending even for the equal ultimate strength of both materials. This remark makes the application of lighter material attractive for bending-dominated applications.

4. PHYSICAL PROPERTIES OF COMPOSITE MATERIALS

A material is referred to as a composite material if at least two diverse components are combined on the microscopically level to a new concrete mixture. The separate substances, based on their various properties, accomplish different tasks. In nature, dissimilar materials are also frequently joined, so that the combination gains remarkable properties that both components cannot achieve separately. The comprehensive surveys of the physical properties and manufacturing of the composites was given by [4)5)6)].

Specifically, “composite” generally refers to solid combinations of high-strength, but brittle reinforcement fibers embedded in a weak, but ductile matrix (Fig. 1). The synergy effect is that the properly synthesized composite inherits the high stiffness and load capacity from fibers and the high ductility from matrix.

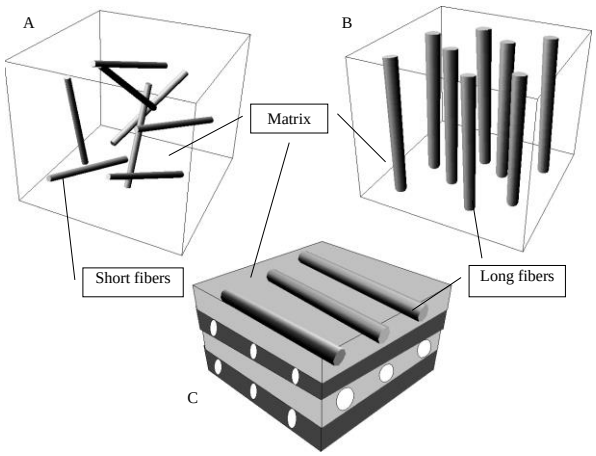

Fig. 1: Types of Composite materials: (A) Reinforcement by short fibers or whiskers; (B) Unidirectional composite, reinforced by continuous fibers; (C) Multilayered, laminated composite made of multiple layers

Chemical industry produces the artificial fibers, for example, carbon, glass or aramid fibers. These fibers possess outstanding mechanical and chemical properties. The matrix materials are steadily developed as well. The raw materials for fibers are usually very brittle and possess only a restricted strength. However, as the fiber diameter decreases, the strength raises tremendously high. The explanation of the increase of strength comprehends in size effect. The size effect unfolds within the remarkable features. On the one hand, the size of the flaw is limited in a thin fiber. The flaw must be many times smaller to generate an endless fiber. According to statistical considerations, the length of a flawless fiber section continues to grow for thin fibers. In other words, the thinner the fiber, the longer the flawless area [8)].

In fiber-reinforced plastics, the mechanical properties, such as stiffness and strength, are determined primarily by the reinforcement fibers. The fibers are made of a variety of materials, and processed to form diverse semi-finished products. For the production of fiber reinforced plastics, mostly inorganic fibers, such as glass fibers, as well as carbon fibers or aramid fibers are used. The carbon-fiber-reinforced polymer is an evolving construction material, which exhibits exceptional mechanical properties, such as strength and rigidity with at the same time light material density. The commercial production of carbon fibers was started in the 1970’s. The application was primarily in the aviation and aerospace industry. The carbon fibers invaded into motorsport at the beginning of the 1980's [9)]. Nowadays carbon fibers are gaining in significance again due to the trend in lightweight construction and are coming increasingly into focus in the automotive industry. Prominent automobile manufacturers are already using carbon fibers with success for visible auxiliary elements and currently research with their application in the principal structures.

With fiber composite materials, at least one type of fiber is "bonded" with a basic material, called a matrix, or resin. In addition to the fiber type, the matrix system plays a significant role in determination of the material properties. The new development and spreading of the composite material in modern industry is closely linked to the improvement of plastics, especially synthetic matrix. Synthetic resins are the perfect adhesive for fiber constructions, light, adhere to several types of fibers, corrosion resistant and assure the flawless impregnation of the fibers. Thermosetting plastic and thermoplastic plastics are used as matrix (or resin) materials, each of which has different advantages and disadvantages when viewed individually. For the moderately loaded structural and safety applications of composite components, thermosetting plastic must be applied, as they possess a higher resistance as thermoplastics. However, the positive features of thermoplastics are their simpler manufacturing and reusability. As already mentioned, the combination of the high-strength glass fibers with a corresponding thermoset plastic matrix enables the synergy effects to be optimally exploited.

The basic element of every component made of

composite material is the unidirectional layer. The laminate is the assembly of several differently oriented individual layers. The properties of laminates are mostly directional and strongly dependent on the sequence of the individual plies. The composite materials are commonly built from several single layers, even thou the fiber directions in all single layers can coincide. The strength and stiffness of a component can be determined by the number of layers, the fiber volume fraction, the fiber direction and the thickness of a single layer as well as the layer order.

In addition to the standard strength values such as tensile strength, yield strength, etc., other parameters such as the interlaminar strength value and the glass transition temperature serve as characteristic values for laminated composites. As its name already describes, the interlaminar shear strength limits the strength of the connection between the fibers and the matrix, which can be destroyed by the high shear stress. The shear stresses occur already at tensile/compressive loading, since the fibers and the matrix have different modulus of elasticity, which results in different strains and stresses in the two materials. The dangerous shear stress occurs along the separation surface between the matrix and the fibers. The standardized short bending test requires relatively small test specimens.

5. MECHANICAL PROPERTIES OF FIBERS

Mechanical properties of fibers

		E-Glass	Carbon HT	Aramid HM	Basalt
Density	kg/m³	2600	1780	1450	2750
Tensile strength	MPa	3400	3400	2800	4840
Modulus of elasticity, along the fibers	GPa	73	235	100	89
Modulus of elasti-city, transverse to the fibers	GPa	73	15	5.4	
Elongation at break	%	3.5..4	1.4-1.5	2.8	3.15
Poisson ratio		0.18			
Degradation temperature	°C	>400		550	1450
Ultimate axial stress sfb	GPa	2.55-2.9	3.3-3.5	2.8	2.52

The glass fiber was the first kind of fiber that was widely used as a reinforcement fiber. The so-called E-glass, with over 90% of all glass fibers used for reinforced plastics has the greatest share. The glass fiber has an isotropic behavior. The modulus of elasticity is approximately 70 GPa, as large as that of aluminum and about of a third of the modulus of elasticity of steel. The tensile strength is nearly 2.4 GPa and clearly below that of carbon fibers. This value is definitely higher than the strengths of aluminum and most of steel alloys. The density of glass fibers is roughly 2600 kg/m³.

Carbon fibers are currently the most widely spread reinforcement fibers for high quality parts. Density of carbon fibers is relative low 1600-2000 kg/m³. Carbon fibers are highly anisotropic, alike aramid fibers. The thermal expansion coefficient is also negative as of the aramid fibers. The carbon fibers possess a high fatigue endurance limit. The dynamic characteristics of laminates based on carbon fibers as reinforcement dominate the dynamic characteristics of such materials as steel or aluminum. The carbon fibers possess the exceptional chemical and thermal properties, as good resistance to corrosion. The strength, stiffness and thermal conductivity substantially differ depending on the type of fiber.

The high strength, low density, high impact and fatigue strength, good heat resistance and dimensional stability, good vibration damping and high-energy absorption capacity characterize the aramid fibers. The density of the aramid fibers, derived from aromatic polyamide, is lower (1450 kg/m³) than the density of carbon fibers. The tensile strength is approx. 2700 MPa. Consequently, the aramid fibers possess remarkably high specific, density-related, strength. The application scope is chiefly the ballistic and industrial protective devices. Aramid fiber plastic composites are exceptionally suited for tensile-stressed lightweight components. However, the fibers are highly anisotropic and the pressure sensitive in the direction of the fibers. This feature poses a problem for the design of components made of aramid reinforced plastic, which are predominantly subject to bending or compressive stresses. Aramid fibers feature an outstanding chemical resistance and low thermal conductivity. Starting at a temperature of approx. 400°C, while the fibers do not melt, they do begin to carbonize. Similar to the carbon fibers, they also have negative thermal expansion coefficient.

6. PHYSICAL PROPERTIES OF RESIN

The task of the resin (or matrix) is to fix the fibers in place and to protect them from environmental effects, such as chemicals or moisture. Regarding the mechanical properties of the fiber-reinforced plastic, the purpose of

the matrix is to transfer the forces to the fibers or between the fibers and to bear the fibers with respect to compressive stress.

Mechanical properties of the non-reinforced matrix resins				
		polyester	epoxy	vinyl ester
density	kg/m³	1120-1250	1100-1250	1070
fracture elongation	%	<3	6-8	3.5-7
Processing temperature	°C	20-180	20-230	20-175
Operating temperature	°C	50-160	45-230	100-150
tensile strength	MPa	50-70	70-90	75-85
E-modulus	GPa	3.5-4.7	2.8-3.6	3.4-3.5
flexural strength	MPa	60-120	140-160	125-135

7. Laminates

Unidirectional plies are pertinent for high-grade fiber composite components, which require high-strength and high-stiffness components. The unidirectional layers have a very low thread waviness, which has an advantageous effect on the strength and stiffness.

The frequently used types of fabric bonds are the plain weave and the twill weave. A plain weave primarily has the points of intersection per square unit, which gives it the known stability of shape. Because of the high shape retention, the drapability of this fabric on physical contours is limited; therefore, they do not slip and are firm.

Non-woven fabrics consist of 2 to 4 unidirectional plies of varied fiber orientation that are placed on top of each other. The fibers of the individual plies are secured by knitting threads or bonding adhesives.

Mechanical properties of fabric laminates				
		Glass	Carbon	Aramid
Fiber volume fraction	%	43	50	50
Tensile strength, bidirectional fabrics	MPa	330..400	560..650	460..540
Tensile strength. Unidirectional fabrics	MPa	590..680	950..1100	790..900
Tensile modulus, bidirectional fabrics	GPa	19..21	52..58	22.27
Tensile modulus, unidirectional fabrics	GPa	24..35	90..100	44..47
Compressive strength, bidirectional fabrics	MPa	310..440	450..520	130..165
Compressive strength, unidirectional fabrics	MPa	480..600	600..800	180..190

References

1) Kobelev V. (2018) Durability of Springs, Springer International Publishing, Wien, ISBN 978-3-319-58477-5 and 978-3-319-86415-0
2) Kobelev V. (2019) Design and Analysis of Composite Structures for Automotive Applications. Wiley Automotive Series, John Wiley & Sons, ISBN 978-1-119-51385-8
3) Peters St. Ed. (1998) Handbook of Composites 2nd Ed, Chapman and Hall, London
4) Kelly A., Zweben C. (2000) Eds. Comprehensive composite materials, Pergamon, Elsevier Ltd. All
5) Kleinholz R., Mathes V., Witten E., Eds. (2010) Handbuch Faserverbundkunststoffe, Vieweg+ Teubner GWV Fachverlage GmbH, Wiesbaden
6) Neitzel M., Mitschang P. (2004) Handbuch Verbundwerkstoffe, Carl Hanser Verlag, München, Wien
7) Argon A. S. (1974) Statistical aspects of fracture. In: Fracture and Fatigue: Composite Materials, Ed. L.J. Boutman, R.H. Krock. Vol. 5. p.153, Academic Press, NY
8) O'Rourke B. P. (2000) Formula 1 Applications of Composite Materials. In: Comprehensive Composite Materials, Elsevier Science Ltd.Vol.6, (ISBN: 0-080437249)

Examinations on composite strips for springs under torsional load

Martin PETRICH, Stefan TITZE, Tom-Luis WEIMANN and Ulf KLETZIN
Technische Universität Ilmenau, Wire and Springs Research Group, Machine Elements Group
Max-Planck-Ring 12, 98693 Ilmenau, Germany
TEL: +49-(0)-3677-69-1865 FAX: 49-(0)-3677-69-1259 e-mail: martin.petrich@tu-ilmenau.de

Fiber reinforced plastics are well established as high tech materials for special purposes such as monocoques in race sports and aviation or premium bike frames. Moreover, the composite materials are used progressively for functional parts and machine elements. However, the scope of necessary knowledge and required experience may lead to conservative usage. To reduce the gap and facilitate the development of new applications, this paper deals with basic mechanical behavior of strips made of fiber reinforced composites under torsional loading.

Therefore, a theoretical description is given and a FEA simulation with ANSYS Composite PrepPost has been developed. On the practical site, composite strips are being manufactured and tested until fracture. The results of measurements are being compared with theoretical analyses and the aforementioned FEA simulations. Furthermore, some specimens have been tested with cyclic torsional loads to develop a first impression of their fatigue behavior. This research may be seen as a contribution to extend the range of composite spring applications and shows some key aspects for future studies.

Keywords: FRP composite strips, torsional load, lightweight volute springs

MOTIVATION

Fiber reinforced plastics (FRP) are used in numerous industries when special requirements such as lightweight construction or chemical resistance are required. The composite materials have been established for several decades and are also used where particular attention has to be paid to fatigue strength. So there are increasing applications in the field of springs.

Leaf springs in particular have become established due to their simple geometry (production) and the main stress (bending stress) running along the spring, which is why the flexural strength of unidirectional laminate layers under cyclical stress has already been the subject of scientific research [1)2)]. Therefore, designs like meander springs [3)] (e.g. DANTO-Spring [4)], bellows springs or spiral-/C-/constant-force-springs [6)7)8)] have been developed to take these bending properties into account. In contrast to this, the round cross-section composites were usually examined for torsional loads and implemented, for example, as stabilizer tubes or helical compression springs .

Besides many other composite springs, one particular design that has so far been less investigated is the conical compression spring as shown in Fig. 1. This so called volute or evolute spring is made of strip material with a rectangular cross-section. Today, this spring made of metal strips is rarely used compared to helical compression springs made of round wires. Due to the mostly plane fiber products, the conical compression spring is particularly suitable for modern FRPs in view of its simple manufacture from fiber strips.



Fig. 1: Volute spring made from FRP strips with a core developed and manufactured by the authors

As with common compression/tension springs, the band of the volute spring is also subjected to a torsional moment. Therefore, this creates a need for understanding not only the static behavior to forced break but also fundamentals of fatigue properties and their comparison to results from bending loads. In the past few years, the usability and quality of FE simulations have also increased and offer added value in the design and evaluation of FRP. That is why simulations should support and confirm the tests.

2. THEORETICAL DESCRIPTION

2.1. COMPOSITE MATERIALS

The materials used in this examination are carbon and glass fibers with epoxy resin like shown in Fig. 2, due to it´s common application in industry *[9].

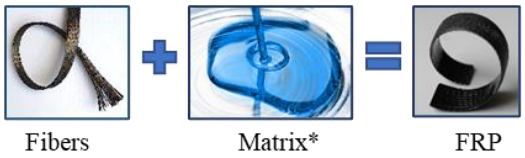

Fig. 2: Illustration of the combination of a composite material.

On the analytical basis, a laminate behavior can be calculated with the Classical Laminate Theory (CLT). For this, an equivalent mechanical model is being created, that assumes a combined but anisotropic material behavior. Many software tools are available to handle the stiffness or flexibility matrix. In futher usage of the CLT for multi-layer composites a ratio width/thickness > 10 is being assumed, to facilitate the usage of a disc-plate-theory. Plate-elements are being considered, when shear forces or moment *M* loads lead to bulging of the plate, additionally to the plate-parallel and forces *N* for disc-elements (equation (1)). The forces/moments have to be related to the width *b*.

$$\{\hat{n}\} = \frac{\{\hat{N}\}}{b} \text{ in [N/mm]; } \{\hat{m}\} = \frac{\{\hat{M}\}}{b} \text{ in [N];} \quad (9)$$

A stress-strain-relation of a disc-plate-element can therefore be described by equation (2). [14]

$$\begin{Bmatrix}\{\hat{n}\}\\ \{\hat{m}\}\end{Bmatrix} = \begin{bmatrix}[A] & [B]\\ [B] & [D]\end{bmatrix} \cdot \begin{Bmatrix}\{\varepsilon\}\\ \{\kappa\}\end{Bmatrix} \quad (10)$$

[A] is defined as the stiffness-matrix of the disc-element. [B] is to be seen as a coupling-matrix between disc and plate-element (strain-bending-coupling). Matrix [D] stands for the stiffness-matrix of the plate-element. According to VDI 2014-3, the influences of these parts of the stress-strain-relation are visualised in Fig. 3.

In particular, the stiffness-matrix of the plate [*D*] is relevant for the following descriptions of the strips. Fig. 4 shows the specific stress distribution when looking at the beam element under torsional load.

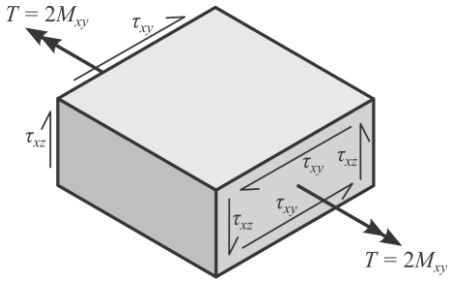

Fig. 4: Stress distribution of a beam element under torsional load[5].

Honickman et al. stated equation (3) that describes the relation of the torsional moment *T* to the angle of twist φ and length *x* for thick laminate plates for an estimate at small angles[5].

$$T = C\frac{d\varphi}{dx} = 2M_{xy} \quad (11)$$

For homogeneous isotropic materials, the St. Venant torsional stiffness coefficient *C* is defined as the product of the shear modulus *G* and the moment of inertia *J*. The calculation of *C* for FRP laminates depends on the type of torsion. A separation has to be made:

FREE TORSION

Free torsion occurs when a certain torsional moment is initiated and this is the only effective load. In other words, all other forces and moments are zero. The torsional stiffness can be calculated by equation (4), where S_{66} is a component of the flexibility matrix:

$$C_{lam,FT} = \frac{4b}{S_{66}} \quad (12)$$

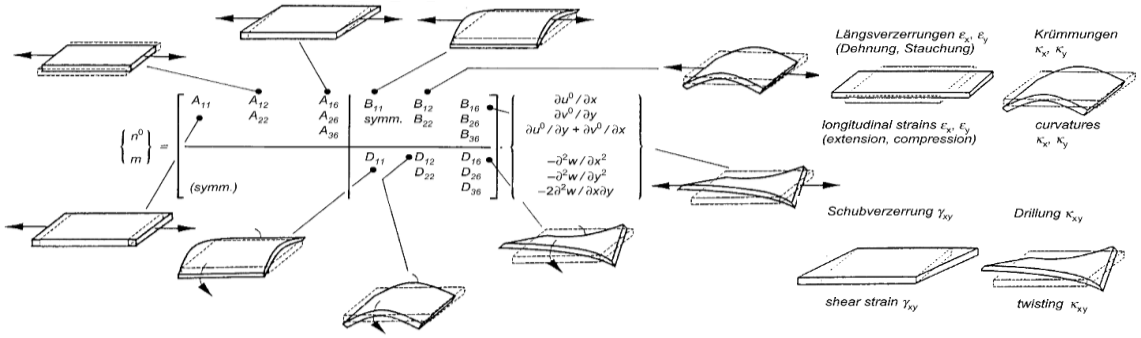

Fig. 3: Effects of the stiffness coefficients and visualisation of deformations from [10].

PURE TORSION

With pure torsion, on the other hand, all degrees of freedom are blocked except for the rotation around the longitudinal axis of the element. Therefore, the length shortening of the strip is prohibited, which occurs through twisting at free torsion. So the coefficient can be described by equation (5), where D_{66} is a component of the stiffness matrix.

$$C_{lam,PT} = 4b \cdot D_{66} \tag{13}$$

Through the knowledge of these relations, a linear calculation of the characteristic curves can be performed.

The Excel tool *Alfa*LAM (v1.3.1) by Thorsten Weber (TU Darmstadt) was used for the calculation of the laminate properties, which includes the CLT.

FAILURE BEHAVIOR AND ASSESSMENT

FRPs have generally a significantly more complex failure behavior than homogeneous materials because of the combination of very different components in one material. Due to the inhomogeneous anisotropic structure, the failure behavior differs depending on the load direction [12)13)].

The laminate behavior strongly depends on the manufacturing process and the resulting errors (voids). For this reason, the calculation is possible, but an ideal laminate is assumed here, which means that the calculated values can rarely be achieved in practice. Hence, performance tests must be carried out [14)].

The types of failure as well as types of stress in which the types of failure mentioned occur will be described below for unidirectional laminates. In general, a distinction can be made between three types of failure in a static loaded fiber composite [14)]:

- Fiber failure (FF)
- Inter-fiber failure (IFF)
- Delamination

As the name already describes, FF is tearing or breaking of the fibers. In almost all cases, this leads to component failure, which is why FF is usually an intolerable form of failure.

The IFF type of failure describes cracks in the matrix or in the fiber-matrix interface. The detachment of the matrix from the fiber is also called debonding. Delamination describes the type of failure when laminate layers separate from each other. Occasionally, this type is meant to belong to the IFF. However, since this failure does not take place intra-laminar but interlaminar and has a different damage pattern, this is usually listed as a separate type of failure. Pull-out could also be mentioned as an effect, whereby a fiber is pulled out of the matrix after it has been detached. A crack that runs along the boundaries of the fiber is also possible [2)].

In assessment of the degree of utilisation of composites, failure criteria F can be used. Different approaches exist, according to Max Strain, Max Stress, Puck, Tsai-Wu or Tsai-Hill for example. Taking the Puck criterion into account, fiber failures occur for $F \geq 1$ by the equations (6). A separation is made for tensile stress ($\sigma_1 > 0$) or pressure stress ($\sigma_1 < 0$) in fiber parallel direction, related to the according material strength R.

$$\frac{\sigma_1}{R_{||}^{+}} = 1 \; for \; \sigma_1 > 0$$
$$\frac{\sigma_1}{-R_{||}^{-}} = 1 \; for \; \sigma_1 < 0 \tag{14}$$

In contrast to metallic materials, FRP have a benign fatigue behavior. In the case of metals, fatigue usually occurs abruptly, whereas the failure of the FRP laminate is foreseeable [14)]. Furthermore, due to the gradual failure, they retain a lower residual strength. They can therefore be used for safety-relevant components and in certain cases are more suitable than metal. In general, the damage caused by the fatigue of FRP can be divided into five stages [15)]:

1. fiber failures and cracks in the matrix
2. connecting the matrix cracks to larger cracks, debonding and further fiber failures
3. delamination and further fiber failures
4. spread of delamination and local fiber failures
5. complete destruction of the laminate

When examining the laminate, however, it is difficult to determine in what phase the component is due to the various types of damage.

Knickrehm also deals with cyclic loads in his dissertation [1)]. Different strip samples were produced and examined under cyclic bending load. The samples revealed a recurring process of damage, which is described as follows:

The damage is initiated by individual FF, so the initiation of fatigue depends on the strength of the fibers. However, these first breaks do not occur at the maximum bending stress. The reason for this is the statistical spread of the strength of the fibers. Depending on the matrix material, matrix cracks may occur, but this does not result in any further damage. Due to the manufacturing process, tension increases occur in the fiber. The fiber

tension is additionally influenced during the load by fiber breaks in adjacent fibers, as well as by the stresses that occur due to deformation. If the fiber tension is greater than the strength, this results in a FF.

The further course is divided into two cases:

On the one hand, fiber-parallel matrix breaks can occur, both in the fiber matrix interface as well only in the matrix. If the cracks are parallel to the fibers, there is little coordinated breakage of the neighboring fibers.

On the other hand, the tear can continue perpendicular to the fiber. If the crack tip is perpendicular to the fiber direction, stress concentrations on the neighboring fibers occur, causing them to break. This failure type leads faster to a fiber break cluster formation, which results in earlier component failure. If the load is continued, the delamination occurs in further layers. This occurs gradually instead of suddenly [1)].

2.3 STRIP GEOMETRY AND MANUFACTURING METHOD

The geometry of the thin reference strips were determined according to DIN EN ISO 527-5 as shown in Fig. 5. All strips have a total length of l_{total} = 250 mm. The width is b = 25 mm and the thickness d = 1 mm. Hence, the b/h ratio is 25. Beginning and end of the specimen are captured with additionally glued cap strips on both sites to avoid breaks in the clamping. The free length is therefore reduced to l = 150 mm.

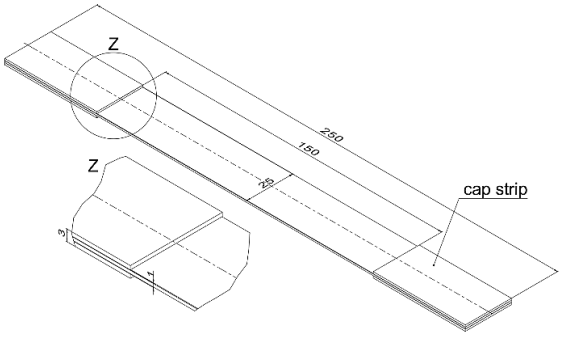

Fig. 5: Geometrical specification of the specimen.

To guarantee a reproducible specimen quality, a two-parted press mould was manufactured. The tool and an example strip are shown in Fig. 6. Before the strips could be produced, some preliminary tests were designed to gain the production knowledge.

The specimen shown in the picture was laminated in the mould with a vacuum assisted procedure. The strips have a buildup of four layers fiber fabric that have an orientation of ±45° to the longitudinal axis (schematic white diagonals below).

Nevertheless, some insignificant air voids existed in the probe, which can be seen as bright dots. The production can not be done by a vacuum infusion process, which would avoid these defects. In the test it was not possible to reach the total flow of the resin along the fibers because the cross-section is very thin and a flow promoter could not be used. Overall, several dozen specimen were produced and documented for the static and cyclic torsion tests.

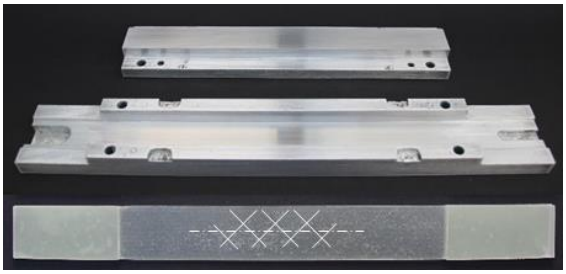

Fig. 6: Tool and sample strip made of four layers ±45° glass fiber reinforced epoxy resin (later added cap strips).

FE-SIMULATIONS WITH ANSYS ACP

Before the practical tests started, an additional analysis was carried out using the FEA in ANSYS Workbench. A special composite module is included in the software package, called ANSYS Composite PrepPost (ACP). First of all, a simple surface model was developed. In the ACP Pre-processor, the layup is applied to the surface and the characteristic values of the laminate are prepared by ACP using the CLT. The material properties were adjusted based on the datasheets of the used materials.

The mechanical setup is then determined in ANSYS Mechanical, analogous to common FEA models, with typical meshing and boundary constraints and the standard solver options.

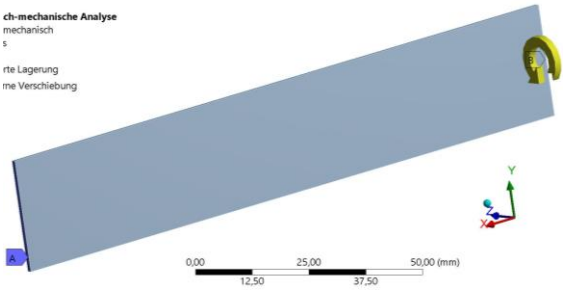

Fig. 7: Simple FE-model with fixation A and twist B.

After solving the model, a detailed deformation and stress/strain analysis can be carried out in the ACP Post module. Furthermore, failure criteria as previously described, can be displayed (see Fig. 8).

Different strip setups and parameters were simulated. Some of the results will later be compared to the

measured curves. Relevant parameters for the simulations were thickness *h*, length *l*, width *b* and composite material of the specimen.

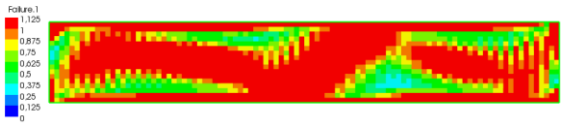

Fig. 8: Typical result of fracture for the second layer at 200° twist, expressed by the Max strain failure criterion. An overload is calculated for the red areas with values $F > 1$.

Therefore, some more simulations were carried out for a maximum twist angle of 300°, which are summarized in Fig. 9. The red line is referred to the previously described test specimen (reference strips). The green lines are calculated for higher parameter values. The blue lines obtain lower values.

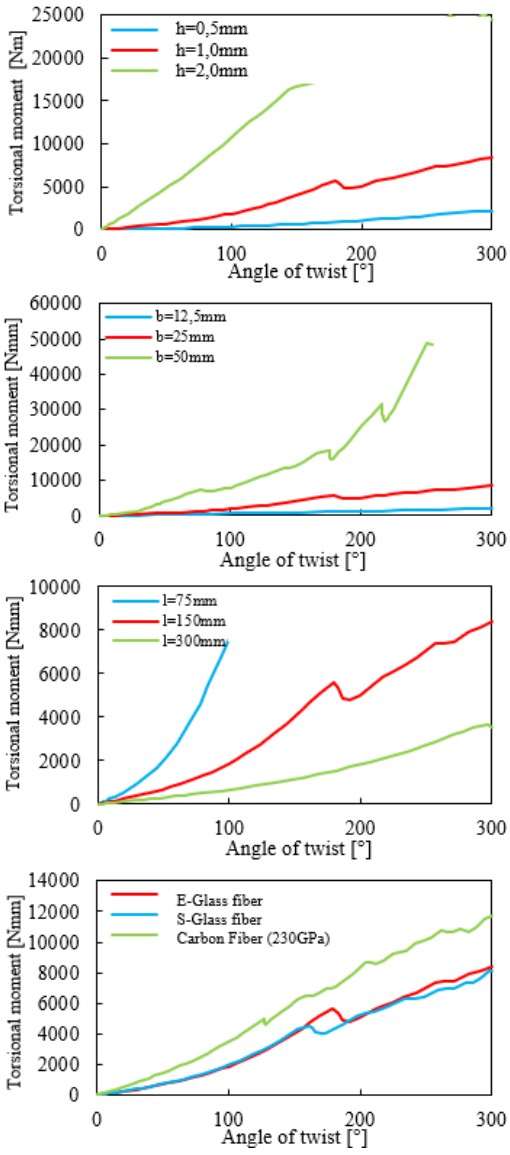

Fig. 9: Results of simulations for different strip properties.

Generally, the deformations and stress/strain or failure criteria have to be regarded, because the simulations do not consider the damaged elements and the curves are further increasing instead of collapsing. Furthermore, real tests have to be carried out, to understand the fatigue behavior of strips under torsional load in general.

4. EXPERIMENTAL SETUP AND RESULTS

4.1 TORSION TEST TO FORCED BREAK

Firstly, clamping units were developed for the usage of a standard tensile and torsion testing machine, which is usually being used for characterising spring steel wires.

The new clamps guarantee the fixation of the the strips at the cap strips and a centrally arranged twist axis, shown in Fig. 10. Additionally, a force for pre-tension $F_{tension}$ is being applied at the upper clamping to stabilize the test. The tests are being separated by the torsion type, like described in the theoretical part. The first test was carried out with a fixed upper traverse (pure torsion) and for the second type, the very small tensile force is being regulated constantly to $F_{tension}$= 10 N (free torsion).

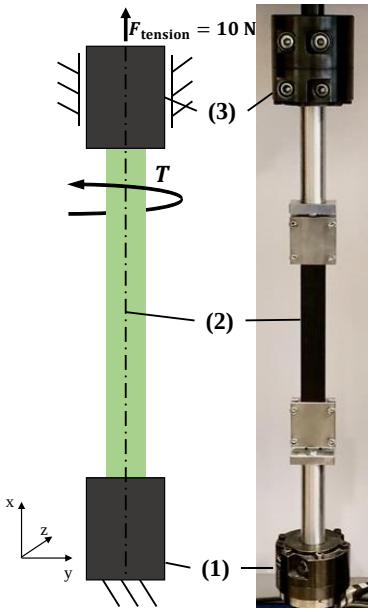

Fig. 10: Experimental setup for static torsion tests (setup for fatigue tests equivalent on cyclic testing machine).

(1) Torsional moment sensor / fixated site
(2) Strip specimen
(3) Torque motor site

A typical test sequence for free torsion is shown in Fig. 11. The pictures are rotated clockwise, so that the left site is the fixed site. Due to the twist, the strip length is reduced and the right clamp follows the deformation with the controlled force Ftension. The sensor (1)

records the torsional moment during the rotation.

How the bright fractures occur diagonally to the longitudinal axis of the strip, thus in the direction of the fibers, is clearly visible. In particular, the simulated failure pattern (compare Fig. 8) can be proven. The highly stressed line is being formed diagonally, starting from one edge of the strip at the left clamp. Then, the line is apparenty reflected on the other edge, where the forced break occurred. Overall, this behavior could be documented for all strip specimen.

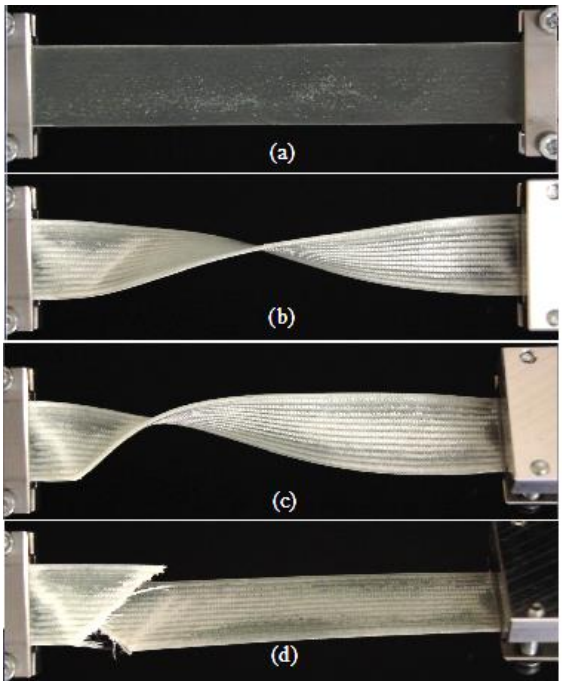

Fig. 11: Procedure of a forced break by free torsion.
a) Unloaded strip. Fixated left clamp
b) 180° twist, highly fractured surface (white areas)
c) Strong buckling and beginning of an out of plane crack
d) Forced break with typical diagonal fracture

Five specimen were tested to forced break with free torsion at $F_{tension}$ = 10 N and two specimen were tested for pure torsion with a fixed upper traverse. The diagram in Fig. 12 shows the results, which are being compared with characteristic curves from the simulations as well as previously described analytically calculated lines.

When looking in details at the characteristic curves for free torsion compared to the propagation of failure in Fig. 11, several points are noticeable. First of all, the torsional moment is slightly progressive and the scatter of the curves is low up to a twist of about 150°. Then, the maxima of the moment are reached at an angle of 170° with a range of 4000 - 5000 Nmm (approx. 4500 N ±10%). For higher twist angles, the curves have different stages, where probably larger areas are failing. Finally, the break occurs between 200°-300° twist angle.

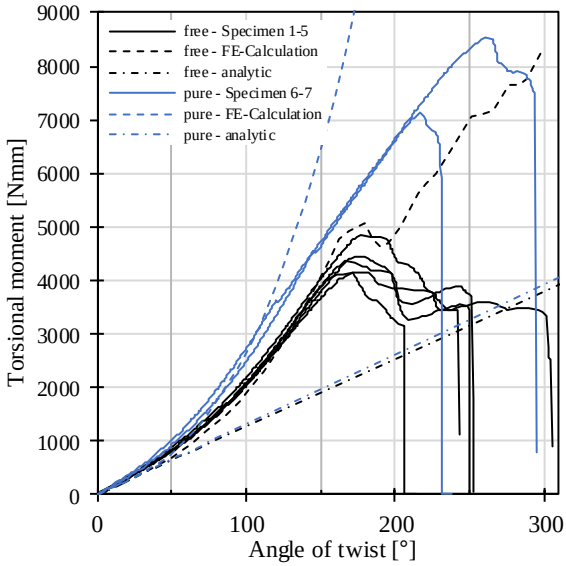

Fig. 12: Moment-twist-curves measured in practical tests compared to analytically and FE-calculated curves.

The next point to be considered is the very good match of the aforementioned simulation results. Even though the progression and the maximum are a little bit higher (ideal material without voids), the fracture is predicted in the same range of about 170° twist angle. After the first collaps by failures, the simulated curve continues to rise, since the model does not buckle and failed areas stay active. It has to be said that typical FEA simulations are limited due to those high deformations. Nevertheless, the predicted curve fits accurate in the interesting area up to 150° twist angle.

In comparison, the analytically calculated line is linear and only applicable for very small deformations. The slope of all variants is the same for 25° rotation. Overall, the diagram proves the calculation and simulation to be valid with limitations for high twist angles.

For pure torsion, both measured curves show the same slope. Due to the fixed traverse, the force $F_{tension}$ inceases significantly. This longitudinal force suppresses the buckling/winding effect, which leads to the break for free torsion. Hence, the specimen can stand up to almost double torsional moment for pure torsion. Furthermore, the break occurs almost suddenly with less stagewise failure behavior. Caused by the higher progression, the simulated curve deviates at about 120° to higher values of momentum. In particular, some small break downs occur in the tests above 120°. The conclusion is obvious: the reduced stiffness through these first fractures flattens the curves. The theoretically ideal simulation cannot take this into account.

As with free torsion, the analytical equation provides

comparable results only for very small angles. For higher twist angles a curve correction is necessary.

In conclusion, the FEA results are in good comparison to the measured characteristics for the reference strip and the failure criteria are proven with very good accordance.

4.2 FATIGUE TESTS

The main goal of the research was to get a first determination of the fatigue behavior of thin composite strips under torsional load. So a special testing machine for cyclic torsion of spring steel wires was used with the strip clamps, as shown in Fig. 13. With this machine, two strips can be tested simultaneously with a frequency of about f_{test} =11 Hz (depending on the angle and torque).

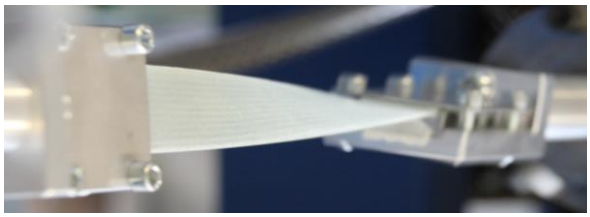

Fig. 13: Fatigue test on a testing machine for cyclic torsion where two specimen can be tested simultaneously.

Based on the intended use for volute springs, the fatigue tests should be carried out with a controlled angle of twist. This means a reduction in the torsional moment, due to increasing fractures in the composite. Moreover, the tests should not be accomplished with an alternating load, because the strips in the compression springs are only twisted in one direction. A mean angle of 50° was determined first, but the maximum amplitude of 50° and so a maximum angle of twist at 100° was not enough to destroy the specimen within the focused final number of cycles $N_{max} = 10^6$. Therefore, the mean angle was raised to 80° and an expected fatigue behavior could be noted in the Wöhler-diagram, that will be described later.

First of all, the progress characteristic of one specimen was examined. Fig. 14 shows the development of the torsional moment decreaings over the numbers of cycles.

Overall, the test can be divided into three phases: Phase I is characterized by a large decline in the torsional moment. It can be assumed, that first fractures occur early and lead to a reduction in the stiffness of the laminate. In Phase II, the stiffness is stabilized over a wide range of cycles. Lastly, the fracture of the strip is being determined by a further reduction of the torsional moment in Phase III. The reduction of the strip stiffness and influences for springs will be discussed later.

Continuing the fatigue tests for 80° mean angle of twist, a classical Wöhler-diagram (*S*-*N*-diagram) could be drawn for different angles of the amplitude.

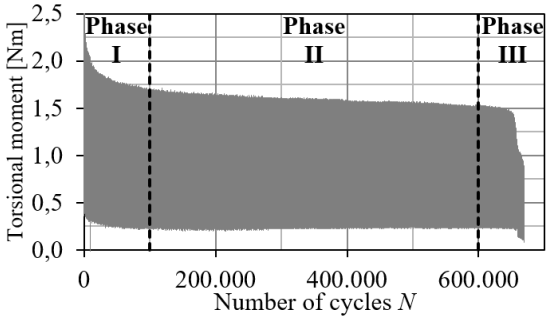

Fig. 14: Reduction of the torsional moment *T* depending on the number of cycles *N* for a specific probe.

Fig. 15 shows the general diagram where either breaks or run-outs are shown. It is important to say, that the maximum angle of twist is 80°+50°=130° and so clearly not in the area where the forced break is announced at about 150° to 200° (see Fig. 12) in the static test. Hence, this demonstrates real fatigue behavior. For the test, eigth specimen were cyclically twisted at the same twist amplitude. For both upper levels the limit $N_{max} = 10^6$ was not reached, due to earlier failure. Therefore, a Wöhler line can be calculated.

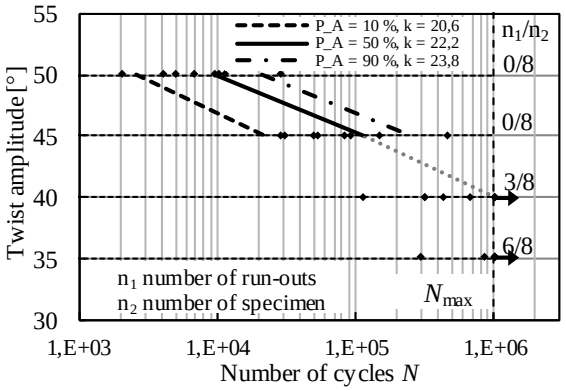

Fig. 15: Wöhler-diagram at mean twist angle of 80°

For the further examinations, the decrease in stiffness is discussed as follows. The softening of the strips can be related to required spring rates. Even if the sample has not yet failed at a specific number of cycles, the function of the spring can no longer be fulfilled for example. To take this into account, an Excel-macro was developed to find the specific *N* for a given reduction of the momentum. Different approaches can be taken for this, e.g. considering the progress of the upper torque limit or the trend of the relation of minimum to maximum torsional moment M_{min}/M_{max}. An exemplary evaluation is shown in Fig. 16 with respect to the last mentioned relation of the torque moments.

The different colored datasets are based on the same specimen, but with difference in evaluation of the allowed reduction of the torque moment (10%, 20% and

30% loss). As expected, the more stiffness loss is allowed, the later the failure is being detected. In particular, the scatter is related to the twist level, as known from the fatigue behavior of metal.

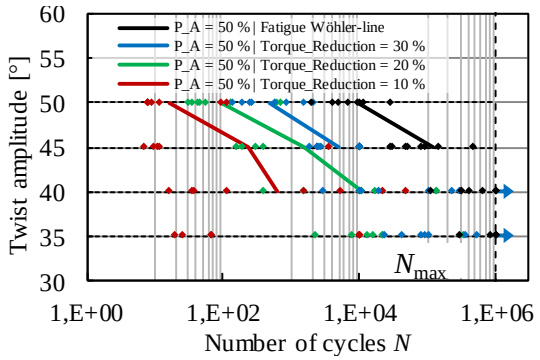

Fig. 16: Wöhler-diagram showing the effects of different evaluations for the reduction of the strip stiffness.

Overall, a very early component failure has to be stated, when the allowed reduction of the torque moment is small, e.g. 10% loss in torsional moment at about 100 cycles or 20% loss at about 100.000 cycles. This is caused by the slope of Phase I in Fig. 14.

CONCLUSION AND OUTLOOK

In this paper, a good comparison of calculated to measured strip characteristics under torsional loads could be shown. The analytical description is suitable only for small angles. The FE-simulations demonstrate very good accordance up to the fatigue area for free torsion and good accordance over a wide range for pure torsion.

An outlook is given for further investigations with other strip parameters. In the practical tests, the failure behavior could be described in detail. An essential characteristic is the stiffness reduction through material fatigue, evaluated in the cyclic tests. This is especially interesting for further studies.

Another topic for the next examinations is the enhancement of the strips by regarding a sandwich layup with a core. This is particullary relevant for springs, because of the lightweight potential and gain in stiffness.

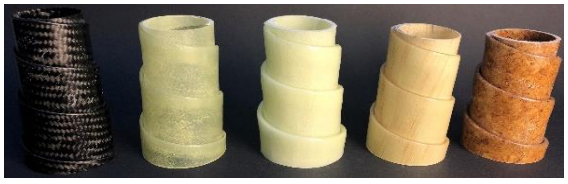

Fig. 17: Example springs with a sandwich core strip layup.

REFERENCES

1) Knickrehm, A.: Zum Versagen unidirektionaler Glasfaser-Kunststoff-Verbunde bei Biegeschwellbeanspruchung. PhD-thesis, TU Darmstadt, 1999.
2) Schoßig, M.: Schädigungsmechanismen in faserverstärkten Kunststoffen - Quasistatische und dynamische Untersuchungen. Springer-Verlag, 1st edition, 2010
3) Stimpfl, J.: Leichtbau in faserverstärktem Kunststoff für Fahrwerksfedern im Automobil. VDFI-symposium on Springs made from fiber composites. Siegen, 20.04.2016
4) DANTO-Invention: DANTO Spring. www.hannovermesse.de/produkt/feder-aus-faser-kunststoff-verbunden/2310289/L161872 Last visit: 26.07.2017
5) Hufenbach, W. et al.: Neuartige Leichtbaufedern in Faserverbundbauweise – Bauweisen / Auslegung / Fertigung. Ilmenauer Federntag; 2010
6) Zemann, R.: www.tuwien.ac.at/aktuelles/news_detail/article/8511/ Last visit: 26.07.201713) Ehrenstein, G.W.: Faserverbund-Kunststoffe: Werkstoffe - Verarbeitung - Eigenschaften. Carl Hanser Verlag, München Wien, 2nd edition, 2006.
7) Otto Bock Healthcare: C-Walk Prothesenfuß 1C40; http://www.ottobock.de/prothetik/produkte-a-bis-z/prothesenfuesse/c-walk/ Last visit: 26.07.2017
8) Scharr, G.: Faserverstärkte Kunststoffe – Federwerkstoffe für den Leichtbau. VDI-Nr. 1972; 2006
9) Epodex GmbH: Transparent Blue Epoxy Resin. https://www.epodex.com/produkt/transparent-blue-epoxidharz/ Last visit: 09.03.2020
10) VDI Guideline 2014-3: Development of FRP components. – Analysis. VDI-Handbook Composites & Construction; 2006
11) Honickman, H.; Johrendt, J.; Frise, P.: On the torsional stiffness of thick laminated plates. Journal of Composite Materials, 48(21):2639–2655, 2014.
12) Kobelev, V.: Failure Criteria for Fiber Composites and Optimization of their Fracture Behavior. Professoral Dissertation; Siegen 2001
14) Schürmann, H.: Konstruieren mit Faser-Kunst-stoff-Verbunden; Springer, 2nd edition, 2007
15) Jones, R.M.: Mechanics of Composite Materials. Taylor & Francis Inc., Philadelphia, 2nd edition, 1999

The Application of a Stainless Martensitic Precipitation Hardening Steel to an Elastic Spring

Robert BRANDT and Martin LINDNER
University of Siegen, Am Eichenhang 50, 57076 Siegen
TEL:+ 49-2722-5216 e-mail:martin.lindner@uni-siegen.de

Andreas ELVENKEMPER
Muhr und Bender KG, Mubea-Platz 1, 57439 Attendorn
TEL: + 49 2722-62-9311 e-mail:andreas.elvenkemper@mubea.com

A stainless martensitic precipitation hardening steel has been processed and validated for the application to an elastic spring. The component is here manufactured by means of a cold forming technology. Strengthening of the material happens during subsequent technology steps, i. e. by work hardening due to cold rolling prior to cold forming and, finally, by precipitation hardening of the component during isothermal tempering. The tensile strength of the here considered steel may exceed 2000 MPa. A conflict of targets between tensile strength and ductility is limiting the contribution of work hardening prior to cold forming. Hence, the major part of strengthening, i. e. 700 MPa, is contributed by ageing and only a minor part, i. e. 500 MPa, by work hardening. The lecture presents the mechanical and electro-chemical properties of the steel. The impact of Mn on the emergence of microstructural details as well as phase composition is thoroughly discussed with respect to the mechanical properties of the steel.

Keywords: precipitation hardening steel, retained austenite, manganese

Pre-release version

1. INTRODUCTION

Stainless steels are well known as spring steels, e. g. the austenitic steels, ferritic steels, martensitic steels, and precipitation hardening steels according to DIN EN 10151. Furthermore, stainless duplex steels according to DIN EN 10270-3 serve as well for spring steels. The here considered steels show typical mechanical properties that delivers the profile for their suitability as a spring material for elastic springs, e.g. by a benchmark of the specific yield strength *YS*/*UTS*, the tensile strength *UTS*, and the elongation *A* at fracture (s. Table 1). Therefore, a member of the precipitation hardening steels has been chosen for this investigation.

Table 1. Typical mechanical properties of common stainless steels after DIN EN 10151 and DIN EN 10270-3

		austenitic	ferritic	martensitic	duplex	Precipitation hardening	target
YS/*UTS*	[-]	0.3	0.4	0.6	0.65	0.9	≥ 0.9
UTS	[MPa]	900 - 1100	400 - 630	750 - 850	1800	1450	≥ 1675
A	[%]	35	20	13	25	20	≥ 5

A stainless precipitation hardening steel has a chromium (Cr) content that exceeds 10.5 %, a low carbon (C) content, and a high nickel (Ni) content. A Ni-martensitic α_2 matrix emerges after solution annealing and a subsequently quenching to room temperature from the prior austenitic phase (s. Fig. 5). The phase transition happens without diffusion so that the newly formed α_2 matrix has the same chemical composition as the prior γ phase. The Ni-martensitic matrix has a high ductility and can be cold formed. Intermetallic phases of nanometer size precipitate during tempering. The size and the degree of dispersion of these precipitates define the strength of the steel by means of tempering conditions, namely temperature *T* and time *t*. Furthermore, a deformation induced transition from retained austenite γ to martensite α_2 and strain hardening by cold deformation may contribute to the strengthening of the steel. [1)–8)]

Since Ni is a rather expensive material, the authors strive for a partial substitution of manganese (Mn) for Ni. As well as Ni, Mn stabilizes the γ-phase and contributes to the precipitation hardening. Therefore, Mn is used to replace Ni in martensitic precipitation hardening steels. The hardness of Fe-Ni-Mn steels are comparable with the hardness of Fe-Ni-steels, but high Mn contents lead to grain boundary embrittlement. [7),9)–13)].

Therefore, the impact of Mn has been investigated

and compared to a reference alloy with a higher Ni-contend and a very low Mn-content. Since Mn tends to segregate, which may lead to embrittlement phenomena, its content is restricted to a maximum of < 4 wt. %. [14)]

The mechanical and the electrochemical properties of the here considered steels have been thoroughly investigated and finally demonstrators of elastic springs have been manufactured.

2. METHODS AND MATERIALS

Two stainless precipitation hardening steels are in the focus of this study, which differ only in its Mn content, namely 3,4 % Mn for alloy A and 2,4 % Mn for alloy B. A Ni-rich alloy serves as a reference material (ref.). Table 2 shows the chemical compositions of these alloys.

Table 2. Chemical composition of the investigated alloys in wt. %

alloy	Cr	Ni	Mo	Mn	Cu	Al	C
ref.	13	8,8	4,0	0.4	2.0	0.34	0.01
A	12	6,8	4.0	3.4	2.0	0.49	0.01
B	12	6,7	4.0	2.4	2.0	0.48	0.01

The manufacturing technology consists of (i) melting, (ii) hot rolling (1250°C), (iii) cold rolling, (iv) solution annealing (1100°C for 1 h), and (v) quenching by water to room temperature. Then a fraction of the plates has been cold rolled. The considered degrees of deformation are φ = 30 % and 60 % and, finally, A50-samples are punched from all plates, including the not cold rolled plates. Precipitation tempering happens at T = 450°C for t = 3 h, so that as rolled and aged specimens of all three alloys with degrees of deformation φ_0 = 0 %, φ_{30} = 30 % and φ_{60} = 60 % are available.

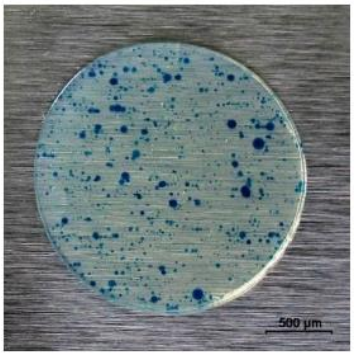

Fig. 1: Indication of pitting corrosion sensitivity by a "KorroPad" color change according to17)

The microstructure is revealed by light microscopy after grinding, polishing and etching with a V2A-etching solution. Hardness measurements are done by means of a FV-300 Vickers hardness measurement system of Future-Tech at a test load of 98 N, tensile tests by means of a universal testing machine, and phase analysis by means of an Panalytical Empyrean XRD. A quantitative phase analysis of cold rolled materials needs particular attention because of textures of preferred grain orientations. Therefore, pole figures of γ_{022} - and α_{112} -peaks are sampled and analysed according to[15)] using a focal spot of 3 x 3 mm² and Chromium-K_α-radiation. The mean intensity of both pole figures represents the volume fraction of each phase, respectively, and the share of each phase is calculated according to[16)]. For the sake of reliability, a complementary quantitative phase analysis has been done occasionally by means of EBSD using a FEI DualBeam Helios NanoLab 600.

Corrosion tests are carried out for alloy A and B. The specimens are manufactured from the above mentioned plates as well. The samples for pitting corrosion tests get polished and "KorroPads" according to[17)] are applied to its surface. As an example, the picture of Fig. 1 shows a surface of a low alloyed steel having a significant pitting corrosion sensitivity. Stress corrosion cracking sensitivity of alloys A and B is tested by means of a 4-point bending test as shown in Fig. 2,[18)] where specimens with the highest observed *YS* (φ_{60}, aged) are strained at 90 % of their *YS* in a saturated steam atmosphere. The time until failure is recorded.

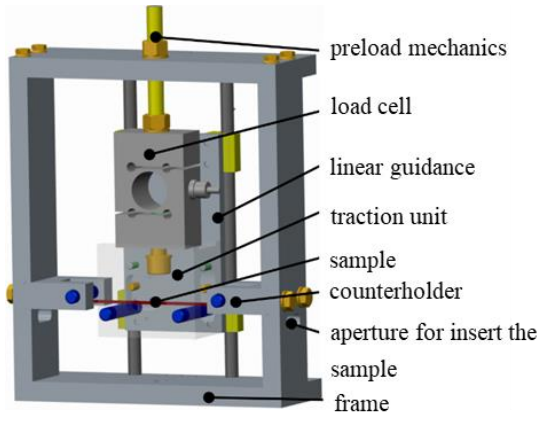

Fig. 2: The static bending test device according to[18)]

3. RESULTS

Table 3 gives the range of the measured yield strength in as rolled (AR) condition YS_{AR} and ΔYS due to aging which were used to create Fig. 3. The diagram of Fig. 3 (a) shows the yield strengths in as rolled condition YS_{AR} for all considered materials that increases with growing degree of deformation.

Pre-release version

Table 3: Range of the values of YS_{AR} and ΔYS in MPa which were used to create Fig. 3.

	ref.		alloy A		alloy B	
φ	YS_{AR}	ΔYS	YS_{AR}	ΔYS	YS_{AR}	ΔYS
0 %	324-480	326-497	486-531	300-375	554-565	640-666
30 %	711-788	317-419	750-785	303-353	964-984	641-666
60 %	918-1007	560-774	1053-1087	380-450	1082-1149	644-566

The reference material is somewhat softer than alloy A and B at all considered degrees of deformation φ. Furthermore, the increase of YS_{AR} with the degree of deformation is uneven. Alloy B shows an increase by 412 MPa from φ_0 to φ_{30} and by 549 MPa from φ_0 to φ_{60}. In contrast to that, alloy A shows an increase by 261 MPa from φ_0 to φ_{30} and by 560 MPa from φ_0 to φ_{60}. The total amount of increase by 558 MPa for the reference material is almost similar to alloys A and B.

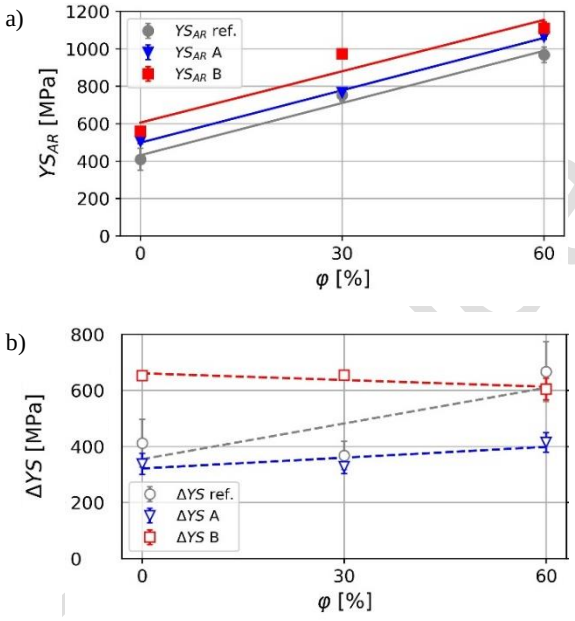

Fig. 3: (a) Yield stress of the as rolled materials YS_{AR} and (b) precipitation hardening ΔYS of the aged materials as a function of the degrees φ of deformation

Fig. 3 (b) shows the change in yield strength ΔYS due to ageing that is much bigger for alloy B than for alloy A. Furthermore, the amount ΔYS does not significantly depend on the degree φ of deformation due to prior cold rolling for both alloys. The reference material, however, shows a similar amount of precipitation hardening as alloy A at φ_0 and φ_{30}, but a significantly higher amount than alloy A, more like alloy B, at φ_{60}, respectively.

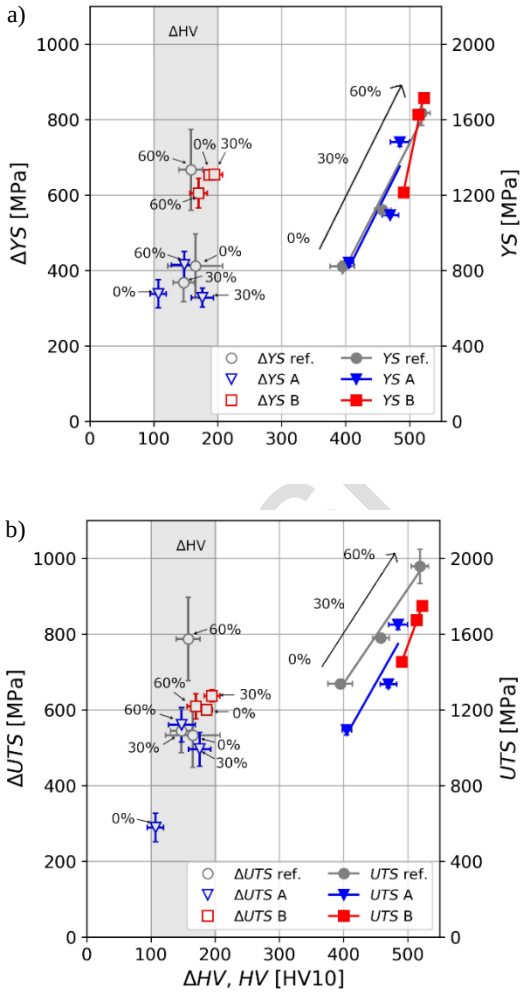

Fig. 4: (a) Strengthening ΔYS and (b) ΔUTS versus the hardening ΔHV (gray), respectively, due to ageing as well as the yield strength YS and the ultimate tensile strength UTS, respectively, versus the hardness HV after aging; the cold rolling degrees are shown by numbers.

The difference in Vickers hardness ΔHV (s. fig. 4, a) between the as rolled and the aged specimens, respectively, discloses values of 110 to 190 HV10 due to precipitation hardening. A correlation analysis of ΔYS vs. ΔHV results in two visible clusters of (ΔYS, ΔHV) pairs of values with centers of gravity at (372 MPa, 149 HV10) and (567 MPa, 178 HV10). The first cluster is made up by results gained from alloy A at all degrees φ of deformation as well as the reference material at φ_0 and φ_{30}. The second cluster is made up by results gained from alloy B at all degrees φ of deformation as well as the reference material at φ_{60}. An analogous correlation analysis of ΔUTS vs. ΔHV however, does not show comparable clusters, but the values are close to a center of gravity at (570 MPa, 170 HV10). Merely the reference material at φ_{60} and alloy A at φ_0, respectively, show a strong deviation

from this center of gravity.

The plot YS vs. HV reveals a uniform linear correlation with a coefficient of determination R^2 = 0,94 (Fig. 4, a). The plot UTS vs. HV reveals a specific linear correlation for each alloy (Fig. 4, b). Alloy B has the highest observed yield strength YS (1700 MPa) and the reference material the highest observed ultimate tensile strength UTS (1950 MPa).

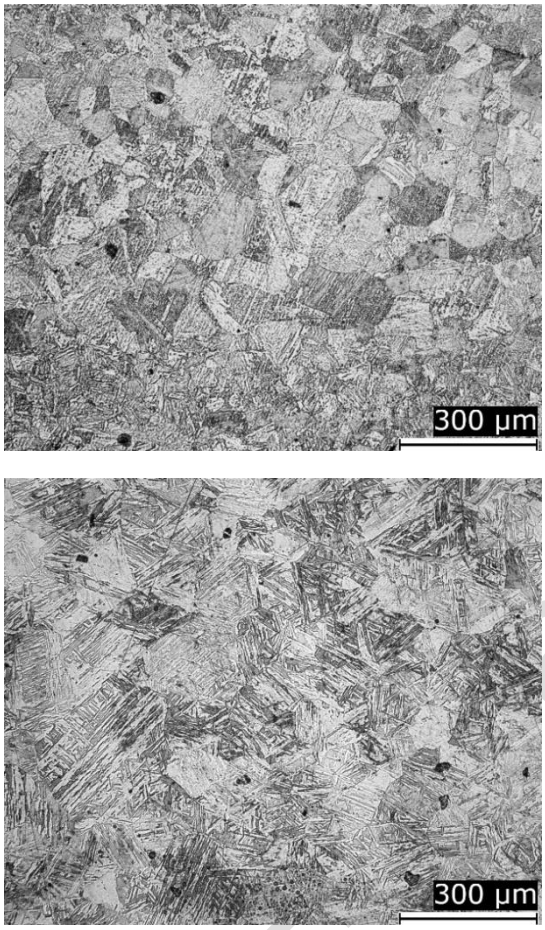

Fig. 5: The Ni-martensitic microstructure of the aged alloys A (top) and B (bottom) for φ_0

The metallographic analysis of the aged alloys A and B reveals a widely spread Ni-martensitic structure as can be seen in optical micrographs in Fig. 5, however, the microstructure of the reference material does not become visible. It Is difficult to perform a quantitative phase analysis of the minority γ phase by means of these micrographs, so that a X-ray diffraction as well as electron a microscopic analysis are required. The procedure of quantitative γ phase analysis is illustrated for the different materials in the aged state for φ_0. Fig. 6 shows the γ_{002} pole figure by XRD and the orientation as well as the phase mapping by EBSD. The γ_{002} pole figures show preferred orientations that are symmetric along the hot rolling direction. The reference material, however, differs slightly from alloy A and B. Accordingly, the EBSD mappings reveal this difference in the microstructure as well. Alloys A and B have much larger grain size than the reference material that, by comparison to the optical micrographs, turn out to be martensitic laths and, in case of alloy A, additionally some elongated austenitic islands. The phase maps further reveal a considerable amount of equiaxed γ grains for the reference material and small, finely dispersed γ phase islands for alloy B.

Table 4 shows the vol. fraction of the austenitic γ phase by means of XRD and occasionally by means of EBSD in parentheses. The majority phase of the as rolled reference material is retained austenite (RA) at φ_0 and φ_{30}. However, at φ_{60} RA becomes the minority component with only 10 %. During ageing the RA content becomes smaller, i. e. 25 % at φ_0, 33 % at φ_{30}, at φ_{60}. Alloy A has a much smaller but still significant RA content of almost 4.5 % to 6.6 % in the as rolled state independent on the degree φ of deformation. Ageing, surprisingly, leads to an increase of the austenitic phase. Alloy B has no significant RA in the here considered states.

Table 4. Austenite content in vol. % of the as rolled and the aged materials for different degrees of deformation

	ref.		alloy A		alloy B	
φ	rolled	aged	rolled	aged	rolled	aged
0 %	53.2	24.6 (30.6)	6.6	14.0 (14.2)	0.0	0.4 (1.2)
30 %	55.7	32.7	4.5	9.3	0.3	1.4
60 %	10.3	0.4	5.3	3.0	0.3	0.4

The corrosion test by means of the “KorroPad”-method discloses that the alloys A and B are pitting corrosion resistant. Selected scans of “KorroPad” testing are shown in Fig. 7. The indicator has not changed its color for any of the specimens. Furthermore, none of the samples failed in the stress corrosion test after 1000 h.

Pre-release version

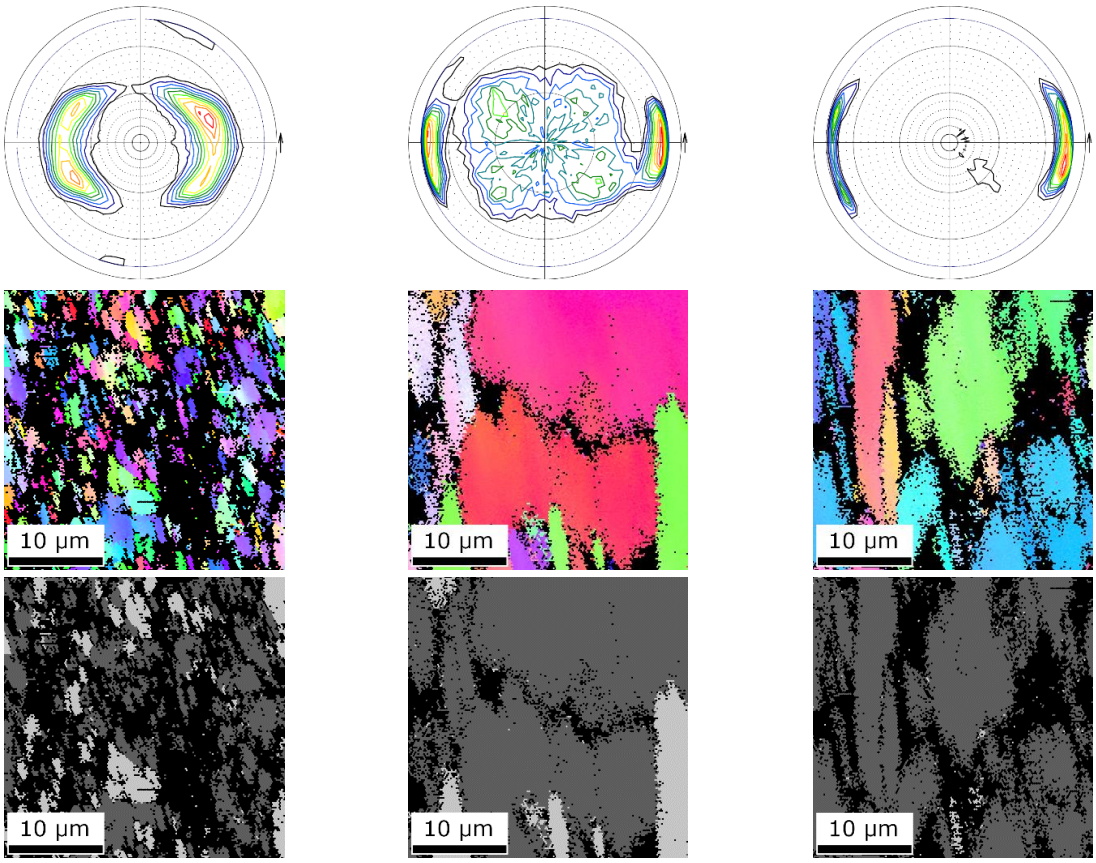

a) ref. material b) alloy A c) alloy B

Fig. 6: Pole figures of the γ_{002} peak by XRD (1st row) , inverse pole figure map (2nd row), and phase map (3rd row) by EBSD of the three alloys at φ_0 after ageing. The black areas of the EBSD maps represent pixels with a confidence index < 0.1. Bright gray represents the γ phase and dark gray the ferritic phase in the phase map.

4. CONCLUSIONS

Three precipitation hardening steels have been investigated in terms of mechanical testing, microstructure and corrosion properties. The yield strength YS of all three alloys can be increased by means of cold rolling and precipitation hardening. As the precipitation hardening happens in the α_2 phase, the γ phase does not contribute to the precipitation hardening. The share of γ in the phase mixture after ageing therefore is decisive for the precipitation hardening ΔYS. Hence, a higher share of γ phase reduces the contribution of the precipitation hardening and it is desired to avoid the presence of γ phase at all.

In the reference material, the transformation of the γ to the α_2 phase due to solution annealing and quenching happens only in a minor degree (Table). Only a sufficient degree of deformation $\varphi > 60$ % and subsequent ageing leads to a significant reduction of RA.

The reduced Ni content of alloy A leads to a much smaller RA content than the reference material. However, the Mn content of 3.4 wt. % stabilizes the γ phase so that still a significant share of γ phase of up to 7 vol. % is apparent. Furthermore, the content of γ phase increases during ageing at φ_0 and φ_{30}. It is assumed that ageing leads to a segregation of the γ stabilizer Mn into the γ phase which enriches its concentration leading to a thermodynamic stable state of the γ phase denoted as reversion austenite.[19] However, it seems that cold rolling may reduce the RA content, as observed in the reference material, and consequently the formation of reversion austenite.

The reduced Ni and Mn content of alloy B totally prevents for RA. The so that a full martensitic matrix is achieved by quenching to room temperature. Furthermore, no formation of reversion austenite is observed.

Mechanical testing reveals that small amounts of Mn supports precipitation hardening ΔYS, as experienced

Preview

for alloy B. However, bigger amounts of Mn increase the share of the γ phase and therefore the volume which contributes to the precipitation hardening decreases, as experienced for alloy A.

Alloys A and B neither show susceptibility to pitting corrosion nor to stress corrosion. All three mechanical requirements shown in Table 1 are met by alloy B at φ_{30} and φ_{60} while alloy A meet them only partially for all degrees φ of deformation.

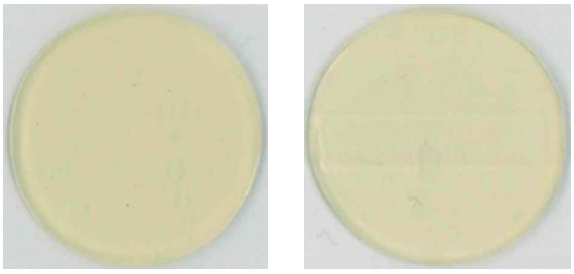

a) alloy A, φ_0 b) alloy A, φ60

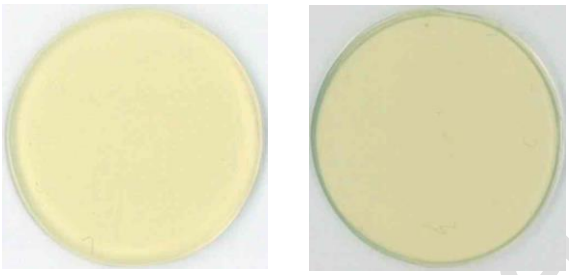

c) alloy B, φ0 d) alloy B, φ60

Fig. 7: "KorroPad" testing results of aged alloys A and B at φ_0 and φ_{60} showing no colour changes

5. OUTLOOK TO ADDITIVE MANUFACTURING OF PRECIPITATION HARDENING STEELS

The authors have considered here a rather conventional manufacturing technology. In the outlook the authors want to outline the following potential for an alternative manufacturing technology, namely additive manufacturing, e. g. by means of laser powder bed fusion (L-PBF), which is able to overcome material restrictions at high degrees of deformation (s. Fig 8). Short-term melting and heating to high temperatures and rapid self-quenching results in a fine grained, martensitic microstructure in components without any need of cold rolling. This non-equilibrium state is highly suitable for a pronounced precipitation hardening in steels. Furthermore, complex component geometries become feasible which cannot be realized by means of the conventional manufacturing technology, in particular very small radii of curvature as well as tailored thickness profiles for highly stressed areas. The combined effects of the reduced number of technologies, of scrap reduction, of excellent material utilization, and of dimensional stability during ageing may compensate for extra costs compared to the more conventional manufacturing technology.

Based on the results of the prior research work, the authors have already initiated a joint research project. Powder has been produced from alloy A at NANOVAL GmbH & Co. KG in Berlin. After the qualification of its flowability and the examination of its absorption behavior, finally, test specimens have recently been manufactured at the Ruhr University Bochum. The here reported RA content of up to 7% for alloy A may significantly be suppressed by choosing proper beam parameters for L-PBF. The University of Siegen takes responsibility for the ageing parameters, the phase analysis, and residual stress assessment of the additively manufactured materials. The materials characterization by means of tensile and compression testing happens at the Technical University of Dortmund to examine the impact of additive manufacturing technology to the precipitation hardening ΔYS. Additively manufactured specimens suffer from rough finishes and high porosity. Therefore, the Technical University of Dortmund applies tomographic methods for the materials analysis. The Results achieved up to now are very promising and will be published soon elsewhere.

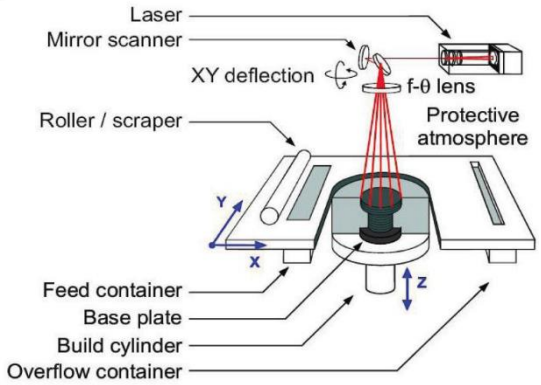

Fig. 8: Illustration of laser powder bed fusion (L-PBF)[19]

ACKNOWLEDGEMENTS

The authors would like to thank the "Europäischen Fonds für regionale Entwicklung" (EFRE) for the founding of this project. Part of this work was performed at the Micro- and Nanoanalytics Facility (MNaF) of the University of Siegen. Furthermore, the authors would like to thank Prof. Jan Sehrt and his working group Hybrid Additive Manufacturing at the Ruhr University Bochum, Prof. Frank Walther and his

Pre-release version

group Materials Test Engineering as well as Prof. Dirk Biermann and his Institute of Machining Technology at the Technical University of Dortmund, respectively, for their kind support and cooperation.

REFERENCES

1) *Nichtrostende Stähle*: Teil 1: Verzeichnis der nichtrostenden Stähle (DIN EN 1088-1), 2014).
2) A. C. Rodrigues, H. H. Bernardi and J. Otubo, *Microstructural Analysis of Co-Free Maraging Steel Aged*, J. Aerosp. Technol. Manag. 6(2014) 389–394.
3) M. Hansen, *Constitution of Binary Alloys, 2nd Edition*, (McGraw-Hill Book Company, New York Toronto London, 1958).
4) A.M. Hall, C.J. Slunder, *The metallurgy, behavior, and application of the 18-percent nickel maraging steels*, Washington, D.C., 1968).
5) W. Sha, *Thermodynamic calculations for precipitation in maraging steels*, Materials Science and Technology 16(2000) 1434–1436.
6) R. Schnitzer, R. Hochfellner, M. Nöhrer, M. Schober, H. Clemens, S. Zinner and H. Leitner, *Microstructural Characterization of PH 13-8 Mo Maraging Steels*, Prakt. Metallogr. 46(2009) 521–536.
7) J.-O. Nilsson, A. Hultin Stigenberg and P. Liu, *Isothermal formation of quasicrystalline precipitates and their effect on strength in a 12Cr-9Ni-4Mo maraging stainless steel*, MMTA 25(1994) 2225–2233.
8) D. Raabe, D. Ponge, O. Dmitrieva and B. Sander, *Designing Ultrahigh Strength Steels with Good Ductility by Combining Transformation Induced Plasticity and Martensite Aging*, Advanced Engineering Materials 11(2009) 547–555.
9) S. Hossein Nedjad, J. Teimouri, A. Tahmasebifar, H. Shizari and M. Nili Ahmadabadi, *A new concept in further alloying of Fe–Ni–Mn maraging steels*, Scripta Materialia 60(2009) 528–531.
10) S. Hossein Nedjad, M. Nili Ahmadabadi and T. Furuhara, *Correlation between the intergranular brittleness and precipitation reactions during isothermal aging of an Fe–Ni–Mn maraging steel*, Materials Science and Engineering: A 490(2008) 105–112.
11) E. A. Wilson, *Quantification of early stages of age hardening in Fe-12Ni-6Mn maraging type alloy*, Materials Science and Technology 14(1998) 277–282.
12) W. Sha, A. Cerezo and G. D.W. Smith, *Phase chemistry and precipitation reactions in maraging steels: Part IV. Discussion and conclusions*, Metallurgical and Materials Transactions A(1993) 1251–1256.
13) B. M. Bronfin, I. Y. Pyshmintsev and V. I. Kalmykov, *Phase transformations and the structure of high-strength low-carbon steels*, Metal Science and Heat Treatment(1993) 187–191.
14) S.-J. Kim and C. M. Wayman, *Strengthening behaviour and embrittlement phenomena in Fe-Ni-Mn-(Ti) maraging alloys*, Materials Science and Engineering: A 207(1996) 22–29.
15) H.-G. Brokmeier, *Texturanalyse mittels winkeldispersiver neutronographischer Kernstreuung*. Habilitationsschrift, Clausthal, 1995).
16) ASTM International, *Standard Practice for X-Ray Determinantion of Retained Austenite in Steel with Near Random Crystallographic Orientation*(E975-13), 2013).
17) Bundesanstalt für Materialforschung und -prüfung, *KorroPad - Verfahrensbeschreibung*.
18) T. Bieker, R. Brandt and C. Haase, *Untesuchung und Bewertung der Spannungsrisskorrosions-empfindlichkeit hochfester Federstähle bei statischer Beanspruchung*, in: H. Frenz, J.B. Langer (Eds.), Werkstoffprüfung 2017: Fortschritte in der Werkstoffprüfung für Forschung und Praxis. Prüftechnik - Kennwertermittlung - Schadens-vermeidung, Deutscher Verband für Materialforschung und -prüfung e.V., Berlin, 2017, pp. 191–196.
19) E. A. Jägle, P. Choi, J. van Humbeeck and D. Raabe, *Precipitation and austenite reversion behavior of a maraging steel produced by selective laser melting*, J. Mater. Res. 29(2014) 2072–2079.
20) K. Kempen, E. Yasa, L. Thijs, J.-P. Kruth and J. van Humbeeck, *Microstructure and mechanical properties of Selective Laser Melted 18Ni-300 steel*, Physics Procedia 12(2011) 255–263.

Prerelease Version

Maintaining the functionality of springs via a high-performance zinc flake system.

Klaus GRADTKE

Dörken MKS-Systeme GmbH & Co.KG , Wetterstraße 58, 58313 Herdecke

TEL:+ 49 2330 630 Telefax: +49 2330 63 354 e-mail: mks@doerken.de

No matter where springs are installed, be it in automobiles, truck & trailers or rail vehicles, they must withstand extreme loads. Surface protection, precisely matched to the respective spring type is therefore required to avoid corrosion damage and to ensure long-term functionality.

Depending on where the springs are used, the coating must meet different requirements. This for example applies to the ability of the coating system to follow elastic deformation without impairing the functional properties (ductility). Other important criteria are the uniform coating of different geometries and the lowest possible cross-linking temperatures. Furthermore, it is important to avoid hydrogen-induced stress corrosion cracking in the application process. In the case of springs made of high-strength steel, this repeatedly leads to the sudden material / functional failure.

The following text will explain how the problem can be solved by selecting a suitable coating process. Against this background, zinc flake coating as a micro-layer corrosion protection solution for springs is presented.

Keywords: Corrosion protection, zinc flace system, coating, application process, cathodic protection, basecoat, topcoat

1. INTRODUCTION

Whether it is in cars, trucks and trailers or in rail infrastructure: springs are used in a wide range of vehicles and applications and often need to withstand very high levels of stress. To avoid corrosion damage and ensure long-term functionality surface protection precisely tailored to the respective spring type is required. Zinc flake systems are a practice-proven micro-layer corrosion protection solution for this.

2. DIVERSE STRESSES IN DAILY USE

Springs of various dimensions, construction type and function are used in nearly all industries, whether it is vehicles, construction or the rail sector. For example, cars and trucks feature diverse springs with very various functions, from corrosion protection to sliding

properties and on to noise suppression. The same also applies for the leaf springs utilised in trucks and trailers. These are responsible for the vertical vibration behaviour and help to compensate potholes or unevenness on the road surface. In this, they are constantly subjected to strong mechanical stresses as well as harsh weathering. In rail transport high speeds

and the associated high dynamic forces in particular represent a stern test for rail fastenings. For the rail clamps employed, this means: as elastic components, they need to withstand the toughest use continuously, functioning reliably and challenging each day.

3. REQUIREMENTS-CONFORMING SURFACE COATINGS FOR SPRINGS VIA ZINC FLAKE SYSTEMS

To ensure that the springs withstand the various challenges of daily use and long-term, faultless use is guaranteed, the springs need to be equipped with a capable corrosion protection. In practice, for many years now zinc flake systems have proved their worth as extremely capable surface protection for parts and components in various areas. A zinc flake system typically comprises a basecoat and a topcoat. The key task of the base coat is to actively protect the coated steel surface against corrosion - it offers so-called cathodic corrosion protection. The scale-like zinc coats which is shown in Fig. 1 create a barrier effect that slows the impact of corrosive media.

As the less noble metal, the zinc “sacrifices” itself and protects the steel below from deteriorating when faced with a corrosive attack. In the case of exclusively passive barrier coatings there is a risk of loss of adhesion or rust penetration, for example in areas where the coating has been damaged. This phenomenon is prevented with the zinc flake thanks to the sacrificial effect.

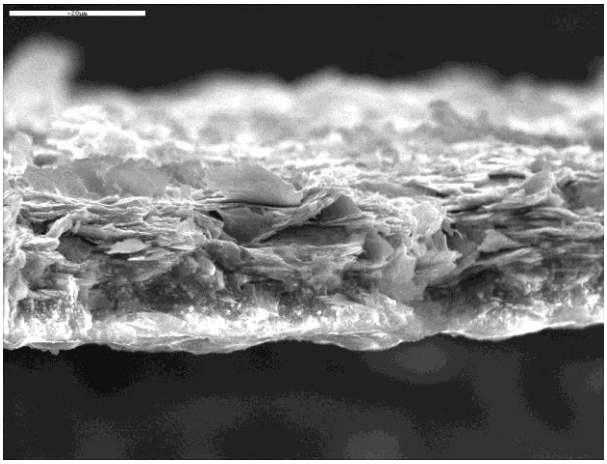

Fig. 7: Scanning electron microscope image of a zinc flake coating

With the zinc flake base coat, up to 1,000 hours against base metal corrosion (red rust) in accordance with salt spray testing according to DIN EN ISO 9227 can be achieved with thin coats of 8 to 12µm (see Fig. 2). In addition, they are free of heavy metals hazardous to health, such as chromium, lead or cadmium, and satisfy the EU directives for the End-of-life Vehicles Directive 2000/53/EC and Restriction of Hazardous Substances Directive 2002/95/EC.

The subsequent application of a topcoat can further enhance corrosion protection. The topcoat offers multi-functional properties such as increased chemical or mechanical resistance, colouring or sliding properties. Depending on type and application, the coating thickness of the topcoat typically stands at 5 to 15µm. Classic technologies require a higher coating thickness to offer a similar level of corrosion protection or their application does not allow them to be used on the micro layer scale.

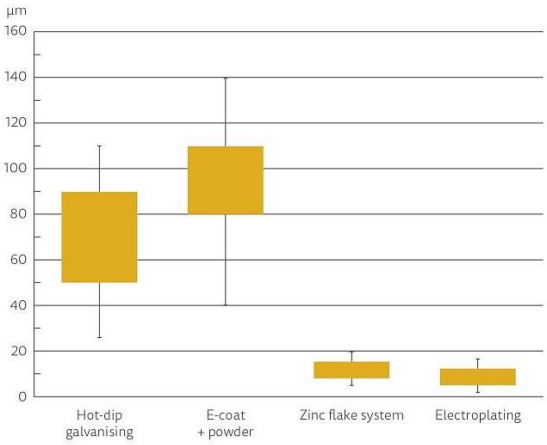

Fig. 8: Typical coat thicknesses of various coating systems

4. IDEAL COATING SYSTEM FOR SPRINGS

Depending on the area of application, the coating is required to satisfy various, often high, specifications of the manufacturers. The numerous advantages and positive characteristics mean that zinc flake systems are able to fulfill the criteria for the surface coating of springs. This concerns, for example, the criterion of ductility, especially important for springs, the capacity of the coating system for elastic deformation without resulting in the limitation of the functional characteristics. In addition to outstanding cathodic corrosion protection and media resistance, the zinc flake system is comparatively ductile.

Similarly, the even coating of different geometries that is often required and material-saving cross-linking and hardening temperatures are key criteria for springs, which are met with the zinc flake coating. Cross-linking already occurs at relatively low annealing temperatures of around 180 °C.

Beyond this, the zinc flake system also avoids the risk of hydrogen-induced stress corrosion cracking, as no hydrogen embrittlement is generated during the application process. Finally, springs, which are used in a large number of fields, also require consistently reliable adhesion. To ensure this and thus achieve optimal corrosion protection it is necessary to have pre-treatment in proor to the coating process, tailored specifically to the respective springs.

5. APPLICATION OF THE ZINC FLAKE SYSTEM

Prior to the actual coating it is necessary to pre-treat the surface of the components. This is the only way to achieve optimal application – and therefore the achievement of functional characteristics such as adhesion. In the next stage the coating is applied, using the rack procedure or the dip-spin process, depending on size and geometry.

In the dip-spin process the springs are immersed into the coating material as bulk goods in a basket with a diameter of 400 to 900 mm, or as racked goods. Depending on the dip-spin parameters and coating setting, an average coat thickness of 3 to 6µm can be applied for each coating procedure. In this, a tilting process can improve the extraction of excess coating

material after cross-linking. During the dip-spin process the coating covers the entire surface area of the spring. In conclusion, centrifuging removes excess material. This application ensures that the spring is fully coated both inside and out. Finally, the components are dried in the furnace.

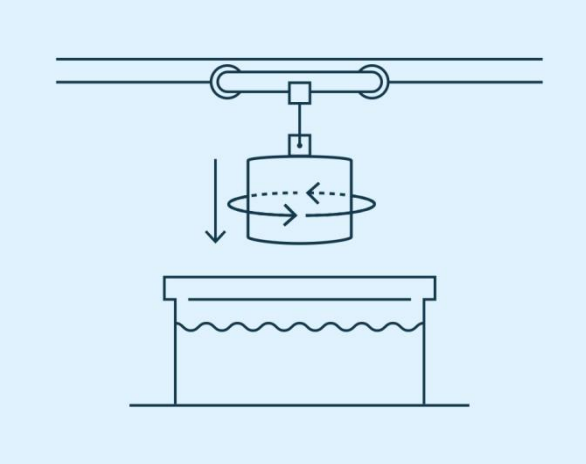

Fig. 3: Dip-spin coating

6. CONCLUSION

In the surface coating of springs, depending on the area of use it is not only long-lasting cathodic corrosion protection that needs to be provided, but also further factors such as media resistance, excellent ductility and low annealing temperatures. For many years now, zinc flake systems have offered a reliable, high-performance coating solution.

ISBN 978-3-00-069928-3



© All rights reserved
VERBAND DER DEUTSCHEN FEDERNINDUSTRIE e.V.
Goldene Pforte 1 • 58093 Hagen